Imperial College
London

Electronic Structure, Transport Properties and Doping of Wide-Band Gap Semiconducting Oxides $Ni_xMg_{1-x}O$ and $BaSnO_3$

Christian Alexander Niedermeier

Department of Materials

The Imperial College of Science, Technology and Medicine

A thesis submitted in fulfilment of the requirements for

the degree of Doctor of Philosophy of Imperial College London

October 2016

Declaration of Originality

This thesis is my own work and any resources used from other authors have been referenced in the text and figure captions.



Christian Niedermeier

London, October 2016

Copyright Declaration

The copyright of this thesis rests with the author and is made available under a creative commons attribution non-commercial no derivatives licence. Researchers are free to copy, distribute or transmit the thesis on the condition that they attribute it, that they do not use it for commercial purposes and that they do not alter, transform or build upon it. For any reuse or redistribution, researchers must make clear to others the licence terms of this work.

Submitted:	October 10th, 2016
Date of examination:	January 12th, 2017
Revised:	February 27th, 2017

Abstract

Wide-band gap semiconducting oxides combine high electrical conductivity with optical transparency and find important applications as transparent contacts in solar cells, energy-efficient smart windows and thin film transistors used in flat-panel displays for smartphones and tablets. Among the material family of transparent conducting oxides, In_2O_3, SnO_2, ZnO and CdO are the most prominent examples which all exhibit excellent n-type conductivity. Transition metal oxides such as Cu_2O, $CuAlO_2$ and NiO were investigated for their p-type conductivity, which remains a great challenge to achieve in oxide semiconductors.

This thesis presents an investigation of the electronic structure and transport properties of $Ni_xMg_{1-x}O$, a fully miscible solid solution of NiO and MgO which allows for band gap tuning in the deep ultraviolet spectral region. Both materials crystallize in the cubic rock-salt structure with nearly identical lattice parameters, but their alloys exhibit an unusually large, non-parabolic band gap bowing which has led to controversial discussions in the literature.

The second part of this thesis focusses on the thin film crystal growth, the electron transport properties and doping in the ideal cubic perovskite $BaSnO_3$, which recently attracted significant interest as high-mobility electron transport material for oxide electronics composed of earth-abundant elements. An effective solid phase epitaxy method for preparation of high-mobility La:$BaSnO_3$ films is developed, employing the room temperature-deposited nanocrystalline films as precursor. Furthermore, the first experimental report of interstitial H-doping of $BaSnO_3$ films is demonstrated, presenting a promising n-type doping alternative for achieving excellent conductivity. Finally, the origin of the exceptionally high room temperature mobility is investigated through an in-depth characterization of the electron effective mass and carrier scattering mechanisms in epitaxial La:$BaSnO_3$ thin films.

List of Publications

C. A. Niedermeier, M. Råsander, S. Rhode, V. Kachkanov, B. Zou, N. Alford, M. A. Moram. "Band gap bowing in $Ni_xMg_{1-x}O$."
Scientific Reports **6**, 31230 (2016). Chapter 3 of this thesis.

C. A. Niedermeier, S. Rhode, S. Fearn, K. Ide, M. A. Moram, H. Hiramatsu, H. Hosono, T. Kamiya. "Solid phase epitaxial growth of high mobility La:$BaSnO_3$ thin films co-doped with interstitial hydrogen."
Applied Physics Letters **108**, 172101 (2016). Chapter 4 of this thesis.

C. A. Niedermeier, S. Rhode, K. Ide, H. Hiramatsu, H. Hosono, T. Kamiya, M. A. Moram. "Electron effective mass and mobility limits in degenerate perovskite stannate $BaSnO_3$."
Under review (2016). Chapter 5 of this thesis.

C. A. Niedermeier, T. Kamiya, M. A. Moram. "Polaron coupling constants in $BaSnO_3$."
arXiv **1612**.01343 (2016). Accompanies Chapter 5 of this thesis.

List of Conference Contributions

C. A. Niedermeier, S. Rhode, V. Kachkanov, B. Zou, N. Alford, M. A. Moram. "The pronounced band gap bowing of $Ni_xMg_{1-x}O$ at the percolation threshold."
9th Symposium on Transparent Oxide Materials and Devices, Epochal Tsukuba (2015). Poster gold award.

C. A. Niedermeier, S. Rhode, S. Fearn, K. Ide, M. A. Moram, H. Hiramatsu, H. Hosono, T. Kamiya. "Facile preparation of high mobility La:$BaSnO_3$ thin films co-doped with interstitial hydrogen."
Materials Research Society Spring Meeting, Phoenix (2016). Oral presentation.

C. A. Niedermeier, S. Rhode, L. Blumenthal, K. Ide, H. Hiramatsu, H. Hosono, T. Kamiya, M. A. Moram. "Electron effective mass and mobility limits in La:$BaSnO_3$ thin films."
European Materials Research Society Fall Meeting, Warsaw (2016). Oral presentation.

To my family for their enduring love and support.

Acknowledgments

I would like to thank my supervisors Dr Michelle Moram and Prof Neil Alford for the great support and giving me the opportunity to join the Materials department for PhD research.

I am very thankful to Prof T. Kamiya for the invaluable insight into the field of oxide semiconductors, the continuous support and interest in my research. I would like to thank Prof H. Hosono for the great facilities I could use during my visit, making my research really exciting, and Prof H. Hiramatsu for all the helpful suggestions and the support I have received in the lab.

Dr Peter Petrov, Dr Bin Zou and other colleagues of the thin film laboratory supported me greatly with my experiments. Thank you very much Dr Sneha Rhode for all the supporting microscopy work, and Dr Michael Råsander for the theory calculations and all other colleagues for their help.

Finally, I would like to thank all my friends who made the past three years a very memorable time. Thank you Jason, Chi, Max and Aaron for our fun and motivating lunch time meetings and the supporting friendship. Thank you K. Ide, J. Kim, H. Tang, Y. Kishida, N. Nakamura, Y. Kumagai, Lee, H. Sato, K. Hanzawa and all other members for giving me such a warm welcome at TokyoTech. I feel very lucky to have met you all and am very grateful for your support and kindness.

Contents

1 Introduction **1**

1.1 Wide-Band Gap Semiconductors 1

1.1.1 Definition and Applications 1

1.1.2 Classification of Wide Band Gap Semiconductors 3

1.1.3 Transparent Conducting Oxides 6

1.2 Fundamental Properties of Wide Band Gap Semiconductors 9

1.2.1 Thin Film Epitaxy and Optoelectronic Properties 9

1.2.2 Doping of Wide Band Gap Semiconductors 11

1.2.3 Electronic Band Structure 16

1.2.4 Light Emission 20

1.3 NiO and $Ni_xMg_{1-x}O$ 23

1.3.1 Structural Properties 23

1.3.2 Electronic Structure 23

1.3.3 Defect Chemistry and Doping 27

1.4 $BaSnO_3$ 29

1.4.1 Crystal Structure and Electronic Structure 29

1.4.2 Defect Chemistry and Doping 31

1.4.3 Thin Film Epitaxy and Electrical Transport Properties 33

2 Experimental Methods **37**

2.1 Thin Film Growth using Pulsed Laser Deposition 37

2.2 High Resolution X-ray Diffraction 38

2.3 Atomic Force Microscopy 41

2.4 Energy Dispersive X-ray Spectroscopy 42

2.5 Hall Effect Measurement 43

2.6 Optical Transmission and Reflection Spectroscopy 45

2.6.1 Ultraviolet-Visible-Near-Infrared Spectroscopy 48

2.6.2 Fourier Transform Infrared Spectroscopy 48

2.7 Spectroscopic Ellipsometry 49

3 Band Gap Bowing in $Ni_xMg_{1-x}O$ **53**

3.1 Introduction 54

3.2 Experimental Methods 56

3.3 Results 58

3.3.1 Structural Characterization 58

3.3.2 Compositional Analysis 61

3.3.3 Composition Dependence of the Optical Band Gap 62

3.4 Discussion 65

3.5 Conclusion 69

4 La:$BaSnO_3$ Solid Phase Epitaxy and Interstitial Hydrogen Doping **71**

4.1 Introduction 72

4.2 Experimental Methods 73

4.3 Results 76

4.3.1 La solubility in $BaSnO_3$ 76

4.3.2 Structural Characterization 76

4.3.3 Compositional Analysis 83

4.3.4 Electrical Transport Properties 84
4.3.5 Optical Characterization and Electrical Transport Properties . 89
4.4 Discussion 91
4.4.1 La Doping Concentration and Donor Activation Efficiency . . 91
4.4.2 Interstitial Hydrogen Doping 92
4.4.3 Electron Mobility, Electron Effective Mass and Carrier Scattering 93
4.5 Conclusion 95

5 Electron Mobility Limits in Epitaxial $BaSnO_3$ Thin Films 97

5.1 Introduction 98
5.2 Experimental Methods 99
5.3 Results 100
5.3.1 La:$BaSnO_3$ Epitaxy on MgO Substrate 100
5.3.2 Structural Characterization of La:$BaSnO_3$/NiO Epitaxial Films 104
5.3.3 Electron Effective Mass 107
5.3.4 Burstein-Moss Shift 114
5.3.5 Electrical Transport Properties 116
5.4 Discussion of Electron Scattering Mechanisms 117
5.5 Conclusion 121

6 Summary and Conclusion 123

Appendix: P-type Conduction in $Ni_xMg_{1-x}O$ 127

Copyright Acknowledgements 131

References 133

List of Figures

1.1 Band gap energy and lattice parameter of wide-band gap semiconductors. 4

1.2 Optical spectra of La:$BaSnO_3$ film and schematic electronic band structure. 6

1.3 Electrical resistivity of impurity-doped SnO_2, In_2O_3, ZnO and $BaSnO_3$ thin films. 7

1.4 Relative abundance of chemical elements in Earth's upper continental crust. 9

1.5 Reciprocal space map analysis of ZnO epitaxial thin films. 11

1.6 Electron mobility and carrier concentration in epitaxial ZnO thin films. 12

1.7 Schematic diagram of dopant levels in $Al_xGa_{1-x}N$, NiO and $BaSnO_3$. . 14

1.8 Formation enthalpy of an intrinsic defect in different charge states as a function of Fermi energy. 15

1.9 Energy band alignment of group III-V, II-VI and stannate wide-band gap semiconductors. 16

1.10 The electronic band structure of wurtzite GaN. 17

1.11 The electronic band structure of rutile SnO_2. 19

1.12 Energy band diagram and partial density of states of LaCuOS. 20

1.13 Phase diagram of the isomorphous NiO-MgO system. 24

1.14 Calculated electronic band structure and density of states for NiO. . . 25

1.15 Calculated electronic band structure and density of states for MgO. . 26
1.16 Defect formation and Fermi level pinning energies in NiO and MgO. . 28
1.17 Crystal structure and electronic band structure of $BaSnO_3$. 30
1.18 Formation energy of intrinsic and extrinsic defects in $BaSnO_3$. 32
1.19 Lattice parameters of (pseudo)cubic crystals with close matching to $BaSnO_3$. 34
1.20 La:$BaSnO_3$ Hall mobility for PLD and MBE-prepared epitaxial films. 35

2.1 Experimental set-up of thin film growth using pulsed laser deposition. 38
2.2 Elastic X-ray scattering in a simple cubic crystal. 39
2.3 Ewald sphere determining the accessible range of the reciprocal lattice of a crystal. 40
2.4 Schematic diagram of AFM using an optical lever sensor. 42
2.5 Characteristic energy levels and X-ray formation in atoms. 43
2.6 Schematic depiction of the Hall effect in a thin semiconductor sheet. . 44
2.7 Transmission of light through a transparent semiconductor sheet. . . 46
2.8 Diffraction grating in an energy dispersive UV-VIS-NIR spectrometer. 48
2.9 Michelson interferometer in a FTIR spectrometer. 49
2.10 Schematic set-up for ellipsometry measurement. 50

3.1 HR-XRD $\omega - 2\theta$ patterns of $Ni_xMg_{1-x}O$ epitaxial thin films. 58
3.2 200 reciprocal space map analysis of $Ni_xMg_{1-x}O$ epitaxial thin films. . 59
3.3 204 reciprocal space map analysis of NiO epitaxial thin film. 60
3.4 AFM micrograpahs of $Ni_xMg_{1-x}O$ thin films. 61
3.5 Cross-sectional STEM and HR-TEM micrographs of $Ni_{0.23}Mg_{0.77}O$ epitaxial thin film. 62
3.6 EDX spectrum and composition analysis of $Ni_xMg_{1-x}O$ thin films. . . 63
3.7 Optical transmission and absorption spectra of $Ni_xMg_{1-x}O$ thin films. 64

3.8 Composition dependence of the $Ni_xMg_{1-x}O$ band gap. 66
3.9 $Ni_xMg_{1-x}O$ density of states and localized impurity Ni 3d states. . . . 68

4.1 XRD patterns of $La_xBa_{1-x}SnO_3$ ceramic targets. 77
4.2 Surface topography of step-and-terrace $SrTiO_3$ substrate and nanocrystalline La:$BaSnO_3$ thin films with corresponding XRD patterns. . 78
4.3 Surface topography and XRD patterns of La:$BaSnO_3$ thin films prepared by solid phase epitaxy 80
4.4 Crystal quality and annealing temperature of La:$BaSnO_3$ prepared by solid phase epitaxy. 81
4.5 La:$BaSnO_3$ 310 reciprocal space map analysis. 81
4.6 Cross-sectional BF and HR-TEM micrographs of (H,La):$BaSnO_3$ after solid phase crystallization. 82
4.7 Surface topography and XRD patterns of a La:$BaSnO_3$ thin film prepared by solid phase crystallization on MgO substrate. 83
4.8 SIMS depth profiles of La:$BaSnO_3$ and co-doped (H,La):$BaSnO_3$ thin films. 86
4.9 Electrical transport properties of (H,La):$BaSnO_3$ thin films. 87
4.10 TDS spectra of mass/charge ratio m/z = 2 (H_2) and m/z = 18 (H_2O) for (H,La):$BaSnO_3$ thin films. 88
4.11 Optical transmission of (H,La):$BaSnO_3$ thin film. 89
4.12 IR optical properties of (H,La):$BaSnO_3$ thin film and dielectric function. 90
4.13 Universal H^+/H^- charge transition level in ZnO, SnO_2, $SrTiO_3$ and $BaSnO_3$. 93

5.1 HR-XRD patterns of 7 at.% La:$BaSnO_3$ thin films on MgO substrate. 101
5.2 Surface topography of MgO substrate and NiO buffer layer. 102
5.3 Surface topography of 7 at.% La:$BaSnO_3$ thin films on MgO substrate. 103

5.4 HR-XRD pattern of La:$BaSnO_3$ thin film on 50 nm NiO-buffered MgO substrate. 104
5.5 HR-XRD 204 reciprocal space map of La:$BaSnO_3$/NiO/MgO. 105
5.6 Cross-sectional TEM micrographs of La:$BaSnO_3$ on NiO-buffered MgO susbtrate. 106
5.7 FTIR spectra and IR dielectric function of La:$BaSnO_3$ films. 108
5.8 Ellipsometry spectra and dielectric function of La:$BaSnO_3$ films. . . . 109
5.9 La:$BaSnO_3$ high frequency dielectric constant as function of carrier concentration. 111
5.10 Increase in La:$BaSnO_3$ electron effective mass with doping level. . . . 113
5.11 Increase in La:$BaSnO_3$ optical band gap with carrier concentration. . 115
5.12 La:$BaSnO_3$ carrier concentration obtained by Hall measurements and La impurity concentration. 117
5.13 Arrhenius plot for evaluation of the grain boundaries potential barrier height in La:$BaSnO_3$ films. 118
5.14 Mobility limits in La:$BaSnO_3$ films as function of temperature and carrier concentration. 120

A.1 Optical transmission of Li:$Ni_xMg_{1-x}O$ thin films. 129

List of Tables

1.1 Optoelectronic and dielectric properties of important semiconductors. 22

1.2 Lattice parameters and effective cation radii in NiO and MgO. 23

4.1 Electrical transport properties of (H,La):$BaSnO_3$ thin films. 85

4.2 Electronic transport properties of H:$BaSnO_3$ and (H,La):$BaSnO_3$ thin films before and after the thermal desorption of H_2 and H_2O. 86

4.3 Electron effective mass of ZnO_2, (H,La):$BaSnO_3$, SnO_2 and In_2O_3. . . 94

5.1 Electrical transport properties of 7 at.% La:$BaSnO_3$ thin film on MgO substrate. 103

5.2 Tauc-Lorentz and Drude model parameters of the La:$BaSnO_3$ dielectric function. 112

A.1 Hole transport properties of epitaxial Li:$Ni_xMg_{1-x}O$ thin films. 128

A.2 List of copyright figures used in the dissertation. 132

Acronyms

3D	3-dimensional
ABSF	average background subtraction filtered
AC	alternating current
AFM	atomic force microscopy
CB	conduction band
DC	direct current
DFT	density functional theory
DOS	density of states
EDX	energy dispersive X-ray spectroscopy
FT	Fourier transform
HAADF	high angle angular dark-field
HR	high resolution
HSE	Heyd, Scuseria and Ernzerhof
IGZO	indium gallium zinc oxide
IR	infrared
ITO	indium tin oxide
LDA	local density approximation
LED	light-emitting diode
MBE	molecular beam epitaxy

NIR	near-infrared
PLD	pulsed laser deposition
RMSR	root mean square surface roughness
RT	room temperature
SEM	scanning electron microscopy
SIMS	secondary ion mass spectroscopy
STEM	scanning transmission electron microscopy
TCO	transparent conductive oxide
TDS	thermal desorption spectroscopy
TEM	transmission electron microscopy
UV	ulraviolet
VB	valence band
VIS	visible
XRD	X-ray diffraction

1 Introduction

1.1 Wide-Band Gap Semiconductors

1.1.1 Definition and Applications

The band gap of a semiconductor determines the energetic separation of the valence band, which is occupied by electrons, from the conduction band, which is unoccupied at absolute zero temperature. While electrons may be excited from the filled valence band to the empty conduction band by thermal activation or photon excitation, no states exists within the band gap which may be occupied by electrons. The forbidden energy gap presents a fundamental property of a semiconductor, and its magnitude and the ability to adjust it determines a semiconductor's potential for device applications. For example, in solar cells semiconductor layers of different band gaps are stacked to efficiently harvest the entire solar spectrum with wavelengths in the near infrared (IR) and visible spectrum for energy conversion. Vice versa, light-emitting diodes (LEDs) employ semiconductors to convert electrical energy into light of a specific wavelength determined by the band gap energy.

Wide-band gap semiconductors are characterized by a forbidden energy gap which is significantly larger than those of the most widely employed semiconductors Si (1.1 eV) and GaAs (1.4 eV) in electronics and photovoltaics. They exhibit fundamental optical absorption edges in the green, blue or even ulraviolet (UV) spectral region. Wide-

band gap semiconductors find important applications as photoconversion materials in UV light detectors, active light emission layers in short-wavelength blue and UV semiconductor LEDs and laser diodes. The available colour spectrum of semiconductor LED chips and laser diodes is now covering the entire visible region including red, green and blue light emission and has modernized lighting solutions, because the devices are very small and robust, energy-saving due to their high conversion efficiency and exhibit significantly longer lifetimes than incandescent light bulbs.

An increasingly important class of wide-band gap semiconductors is represented by transparent conductive oxides (TCOs), which combine high optical transparency in the visible spectral region with good electronic conductivity and find important applications as transparent contacts for solar cells, energy-efficient smart windows and high mobility electron transport layers in thin film transistors for flat panel displays. Since the growth of the TCO market strongly benefits from the rising demand in sustainable energy solutions using solar power generated from photovoltaic cells and the world-wide adoption and integration of flat panel displays and smart devices in everyday life, application and integration of oxide semiconductors is a key technology in the future. Furthermore, development of oxide power electronics is still in its infancy and its full potential is yet to be explored.

The first chapter of this thesis provides a comprehensive overview of the fundamental properties and applications of different classes of wide-band gap semiconductors. Secondly, the scientific background and an introduction to the current status of research on the wide-band gap semiconducting oxides $Ni_{1-x}Mg_xO$ and $BaSnO_3$ is provided, which will be the focus in the results chapters of this thesis.

1.1.2 Classification of Wide Band Gap Semiconductors

Wide band gap semiconductors are typically classified according to their chemical affiliation into group II oxides and chalcogenides (ZnO, ZnSe, NiO), group III nitrides (GaN, AlN, InN), and the group IV semiconductors (SiC, diamond). Since optoelectronic devices based on these semiconductors require high quality crystals, these materials are usually prepared in form of nanometer-scale thin films by vapour phase epitaxy at high temperatures on lattice-coherent single crystal substrates. Thus different wide-band gap semiconductors are often compared by their band gap energy and lattice parameter as shown in Fig. 1.1. The lattice constant a of hexagonal crystals can be compared with those of cubic crystals after dividing by a factor of $\sqrt{2}$ in terms of atomic bond lengths. Direct and indirect band gap semiconductors are indicated with filled and empty symbols, respectively. For application in solar cells and LEDs, direct-band gap semiconductors are of particular interest since they generally exhibit better light absorption and light emission properties than indirect band gap semiconductors. The wide-band gap semiconductors subject of this work are $Ni_xMg_{1-x}O$, a fully miscible solid solution formed of NiO (3.7 eV) and MgO (7.8 eV), and the ideal cubic perovskite $BaSnO_3$ (3.1 eV).

Extensive research on the III nitride $Ga_xIn_{1-x}N$ system has been conducted with the prospect of realising efficient green and blue LEDs. The development of the shorter wavelength GaN (3.4 eV) LEDs which enabled energy-efficient and environmentally friendly white lighting has recently been awarded with the 2014 Nobel Prize in Physics [2]. The III nitride wide band system has then been extended using $Al_xGa_{1-x}N$ alloys to increase the band gap up to 6.2 eV for development of deep UV LEDs [3]. $Al_xGa_{1-x}N$ is commonly alloyed with InN to a small amount for enhancing light emission efficiencies, which is thought to be due to compositional segregations of InN creating built-in quantum wells [4]. While $Ga_xIn_{1-x}N$ LEDs are efficient light sources

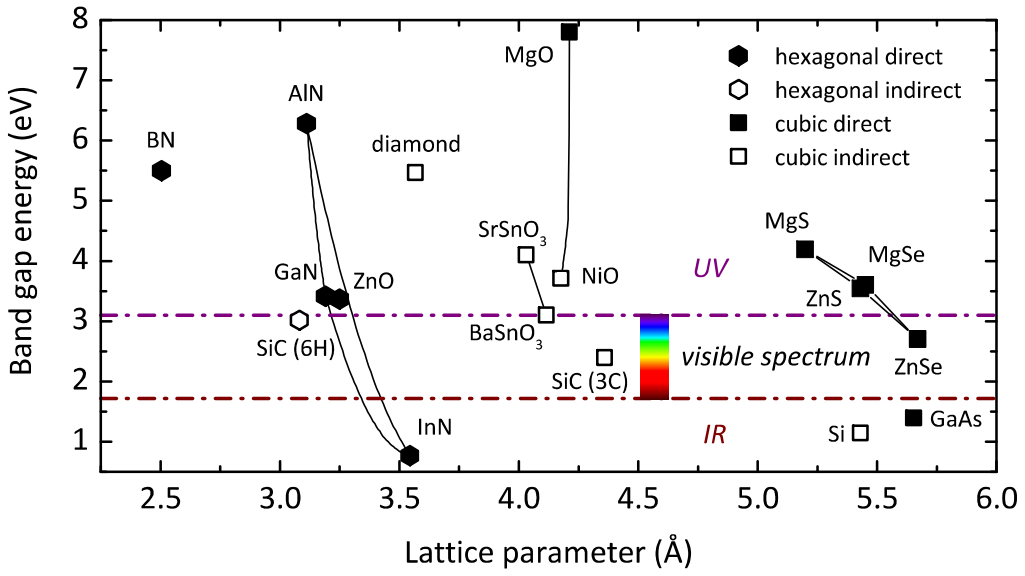


Fig. 1.1: Comparison of the band gap energy, lattice parameter and crystal symmetry of important wide-band gap semiconductors (reproduced after Wang in Ref. [1]). Direct and indirect band gap semiconductors are indicated with filled and empty symbols, respectively.

in the visible range, the efficiency of UV LEDs based on $Al_xGa_{1-x}N$ suffer mainly from the high density of dislocations arising from the hetero-epitaxial growth on foreign substrates [5] and the difficulty of p-type doping for the higher band gap materials [6]. However, high crystal quality epitaxial GaN films on sapphire can be obtained using a low-temperature buffer layer of AlN [7]. Homoepitaxial growth on native GaN substrates results in the highest crystal quality, but large-area GaN single crystals are very difficult and expensive to prepare.

Among all oxide semiconductors, ZnO demonstrates the greatest potential for fabrication of efficient UV LEDs and laser diodes as very sharp excitonic emission at around 385 nm wavelength can even be observed at room temperature [8]. ZnO is a direct band gap semiconductor (3.3 eV) which also crystallizes in the wurtzite structure and the lattice parameters are very close to GaN. Likewise, high quality ZnO

thin films can be grown on Al_2O_3 and $ScAlMgO_4$ substrates [9]. The key problem to solve for fabrication of more efficient UV LEDs is the difficulty of p-type doping of ZnO [10], which poses a problem for most oxide semiconductors in general. Only few reports of p-type conductive ZnO exist and the reproducibility of hole transport properties has been questioned. An UV LED composed of p-n homojunction ZnO with a ZnO-$Be_{0.2}Zn_{0.8}O$ quantum well structure with a sharp light emission wavelength of 362 nm has been reported [11], but efficiencies are low as compared to III-nitride LEDs.

ZnSe is a direct band gap semiconductor (2.7 eV) crystallizing in the zinc blende structure for which bright blue emission was obtained. Alloying with other isostructural II chalcogenides to form MgS-ZnSe solid solutions allows for tuning of the band gap within the UV spectral region. Multi quantum wells with a wide flexibility to adjust the lattice parameter can be prepared on the commonly used GaAs substrate. Even though efficient white ZnSe-based LEDs can be produced [12], the major drawback of the chalcogenide-based devices is the short lifetime due to microscopic defects that cause device degeneration [13].

SiC crystallizes in different modifications, among them the stable SiC 4H in wurtzite structure with a band gap of 3.2 eV is widely used in high power electronic devices. SiC has also been used to fabricate blue LEDs [14], but due to its indirect band gap light emission efficiencies are low. Diamond also belongs to the group of indirect band gap semiconductors (5.5 eV), but due to its extraordinary high exciton binding energy it shows strong light emission at room temperature and is investigated for application in deep UV LEDs [15]. Furthermore diamond shows a very large breakdown electric field and is being developed for power electronics [16].

1.1.3 Transparent Conducting Oxides

Transparent conducting oxides (TCOs) such as In_2O_3, ZnO, SnO_2 and $BaSnO_3$ present an important class of wide-band gap semiconducting oxides which are characterized by their functionality in combining high optical transparency in the visible region with large electrical conductivity. An example of the optical spectra of a typical TCO is given by a La-doped $BaSnO_3$ film on a MgO substrate in Fig. 1.2(a). TCOs are optically transparent in the visible spectrum from about $300 - 800$ nm and the oscillation fringes result from interference effects in the film. The fundamental absorption edge in the short wavelength blue or UV spectral region is determined by the band gap (Fig. 1.2(b)) and at high doping levels enhanced IR absorption and reflectance is observed due to plasma oscillations of quasi-free electrons occupying the conduction band [17].

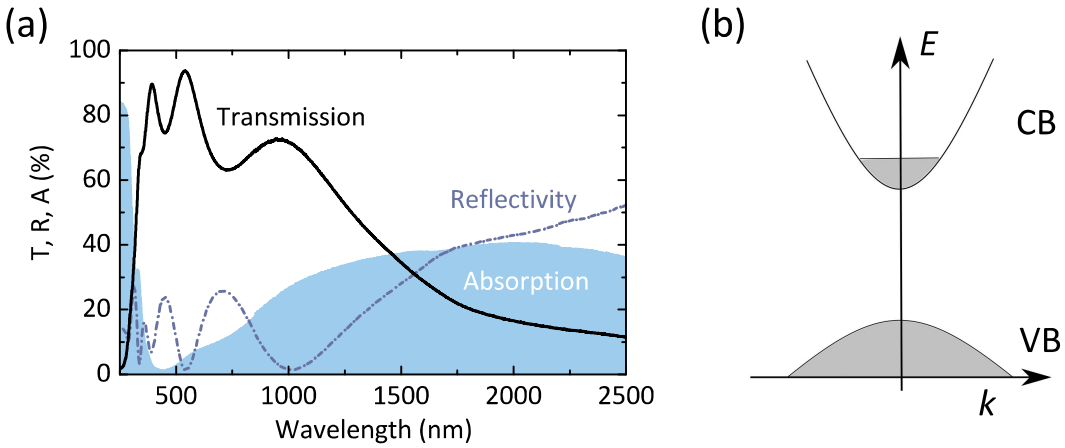


Fig. 1.2: (a) Optical transmission, reflectance and absorption spectra of a La-doped $BaSnO_3$ film for wavelengths of $250 - 2500$ nm. (b) Schematic electronic band structure of degenerate La:$BaSnO_3$ (reproduced after Ginley et al. [17]).

After doping, In_2O_3, ZnO and SnO_2 exhibit a resistivity as low as 10^{-4} Ωcm (Fig. 1.3) [18]. Polycrystalline Sn-doped In_2O_3 (indium tin oxide, ITO) is extensively used in commercial applications as transparent contacts in solar cells and flat

panel displays since it provides the largest conductivity while maintaining 90 % optical transparency in the visible spectral region. Further TCOs include related alloys or compounds, such as $ZnSnO_3$, Zn_2SnO_4 and $MgIn_2O_4$. CdO and Cd_2SnO_4 are also subject of research, but are unlikely to find commercial applications due to Cd toxicity. All of these semiconductors can be deposited at low temperature which is beneficial for industrial production to reduce manufacturing costs and enables device preparation on soft and flexible polymer substrates for a large variety of applications. La-doped $BaSnO_3$ is an emerging TCO which recently gained significant attention since the report of a 320 cm^2/Vs room temperature mobility in single crystals [19], presenting the highest reported for any TCO material at a similar high doping level and the highest mobility among all perovskite oxides.

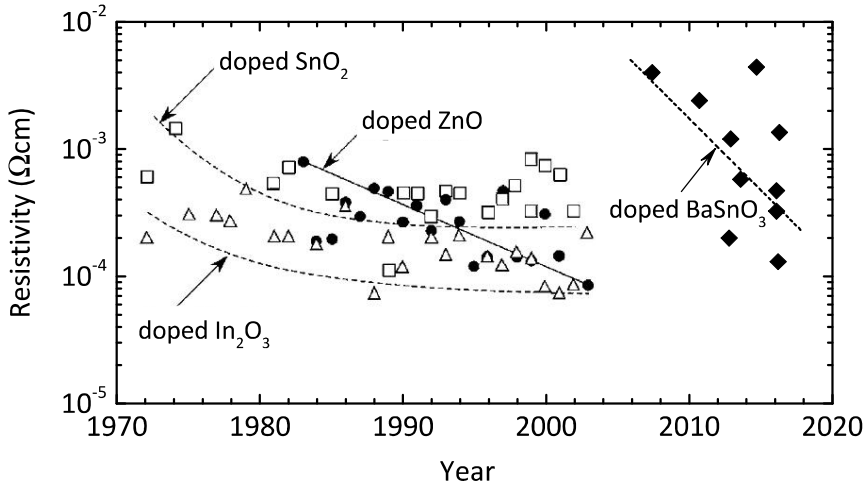


Fig. 1.3: Progress of decreasing the electrical resistivity of impurity-doped SnO_2, In_2O_3 and ZnO thin films from 1970 until 2005 (after T. Minami [18]). Research on improving the electric transport properties of impurity-doped epitaxial $BaSnO_3$ thin films started in 2007 with increasing research efforts up to present (data after Refs. [19–27]).

Most TCOs are characterized by a dispersive parabolic metal s orbital-derived conduction band with closed d-shell $(n-1)d^{10}ns^0$ electronic configuration ($n \geq 4$),

where n denotes the principal quantum number. Since the electron transport proceeds through the large metal s orbitals of the cations, even amorphous oxides of these elements may be converted into transparent conductors [28]. The volume of published research on amorphous oxide semiconductors has grown significantly since the demonstration of a flexible and transparent high mobility thin film transistor employing amorphous InGaZnO (IGZO) as channel layer [29]. Due to its ease of fabrication and excellent performance, amorphous IGZO is increasingly used to replace Si:H in thin film transistors for flat panel displays.

TCOs based on the element In are increasingly becoming expensive, since In is a scarce element in the Earth's crust (Fig. 1.4). Current research efforts aim at the development of transparent conductors composed of earth-abundant elements like Zn [30] and Sn [31]. Besides considering the material cost, it is essential to develop alternative TCOs since the material of choice for the desired application depends on the specific application. Multiple factors like the TCO stability, the energy band alignment as well as the structural match to other materials demand a wider palette of materials to chose from for preparation of heterojunction devices. In this regard, the emerging TCO $BaSnO_3$ which is composed of abundant elements is increasingly attracting attention not only due to its extraordinary high electron mobility, but also the high temperature stability in air and oxygen [19] as well as its application potential for integration into multi-functional perovskite-based optoelectronic devices [32, 33].

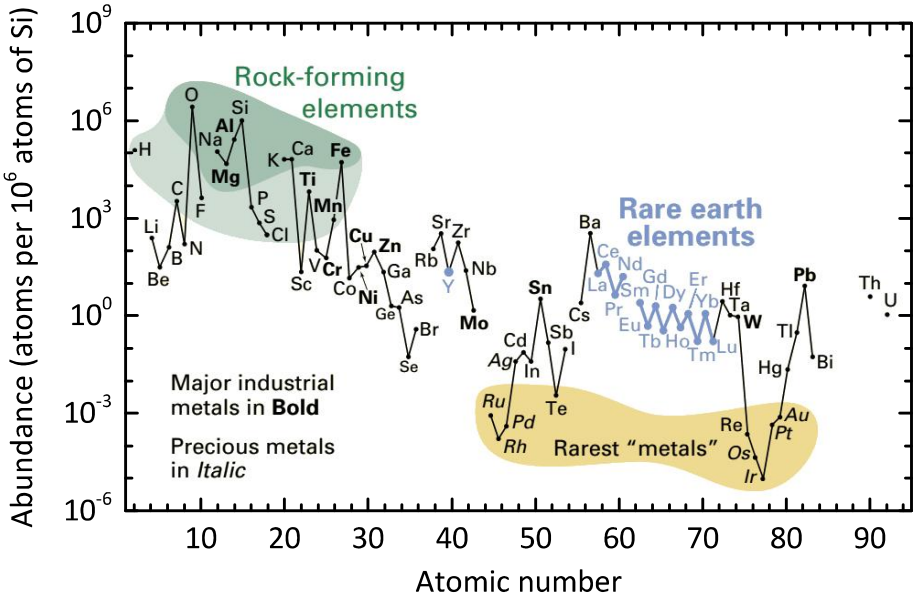


Fig. 1.4: Relative abundance of chemical elements in Earth's upper continental crust (after G.B. Haxel et al [34]).

1.2 Fundamental Properties of Wide Band Gap Semiconductors

1.2.1 Thin Film Epitaxy and Optoelectronic Properties

The optoelectronic properties of semiconductors can only be fully exploited when it is possible to prepare semiconductor crystals of high quality with a minimum defect density. Polycrystalline semiconductors have grain boundaries which act as scattering centres for carriers and deteriorate the device performance. Thus semiconductors are generally prepared as epitaxial thin films by growth on structurally-coherent single crystal substrates. Homoepitaxial semiconductor growth on a native substrate is preferred to achieve the highest quality films, but often a bulk single crystal of the same material is commercially unavailable, has undesired physical or chemical properties

or is too expensive to prepare in large dimensions. Commonly a compromise is made by employing heteroepitaxial growth on a lattice-matched single crystal substrate at the cost of thin film quality.

Typical examples demonstrating the importance of heteroepitaxial semiconductor growth on foreign substrates is the preparation of GaN-based or ZnO-based LEDs on sapphire substrates with a large lattice mismatch of ∼16 % and ∼18 %, respectively. For GaN on sapphire LEDs, a high density of dislocations is introduced which poses a major problem for preparation of more efficient UV-LEDs, since defects significantly reduce radiative recombination probabilities of electron and holes [35]. Typically, a low-temperature buffer layer of AlN is first grown on the sapphire substrate to minimize the density of dislocations in the semiconductor layers of the device structure grown on top [36].

The importance of substrate choice for the preparation of high quality epitaxial semiconductor thin films is demonstrated by the difference in crystal quality of ZnO films epitaxially grown by laser molecular beam epitaxy (MBE) on sapphire and $ScAlMgO_4$ substrates. Epitaxial growth on $ScAlMgO_4$ substrates reduces the mismatch to only ∼0.1 % and XRD analysis of the out-of-plane tilting and in-plane twisting angles indicated very small deviations in the crystal orientation as opposed to films on sapphire substrates [9]. Reciprocal space map analysis further demonstrates that the ZnO($11\bar{2}4$) diffraction peak is much sharper for thin films grown on $ScAlMgO_4$, indicating a higher crystalline quality comparable to that of a ZnO bulk single crystal (Fig. 1.5).

The electron mobility of undoped ZnO thin films is increased by growth on $ScAlMgO_4$ as compared to growth on sapphire substrates due to the reduction of crystalline defects and also the residual carrier concentrations is significantly reduced by more than an order of magnitude (Fig. 1.6). In particular, a 100 nm $Mg_{0.15}Zn_{0.85}O$ buffer layer annealed at high temperature of 1000 °C is employed to benefit from

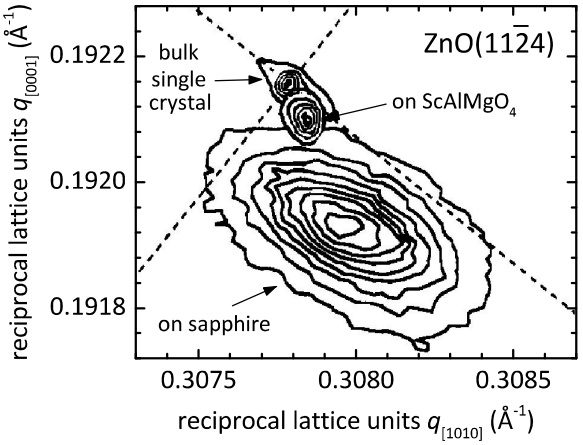


Fig. 1.5: Reciprocal space map of ZnO(11$\bar{2}$4) diffraction peaks for a bulk ZnO single crystal and ZnO thin films grown on sapphire and $ScAlMgO_4$ substrates (after Ohtomo et al. [9]).

an atomically flat surface before deposition to enable layer-by-layer growth of highly oriented films with minimal mosaicity [37]. Sharp photoluminescence peaks and clear splitting of exciton peaks could only be observed from high quality samples grown on $ScAlMgO_4$ substrates [38]. From the example it becomes evident that the choice of a suitable single crystal substrate and buffer layer is crucial to optimize the electron transport and optoelectronic properties in crystalline semiconductor films.

1.2.2 Doping of Wide Band Gap Semiconductors

The ability to dope a wide-band gap semiconductor with free carriers for tuning of the electrical transport properties is essential for device applications. In general doping is achieved by introducing intrinsic or extrinsic defects into the semiconductor which act as either electron donors or acceptors. The concentration of intrinsic defects in compound semiconductors such as cation/anion vacancies and interstitials is controlled by selecting appropriate growth conditions. The extrinsic defect concen-

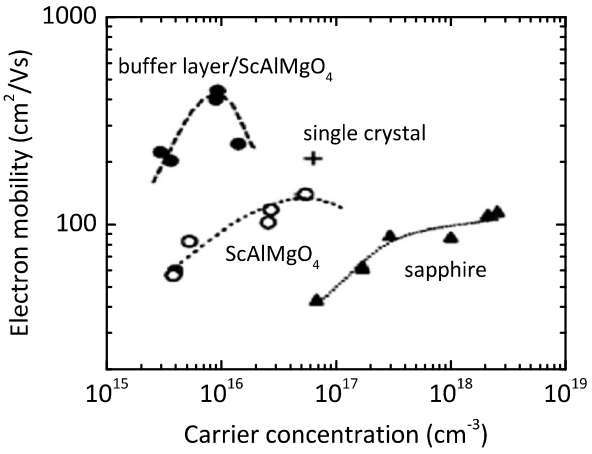


Fig. 1.6: Relationship between electron mobility and carrier concentration in ZnO thin films grown on sapphire (triangles), on $ScAlMgO_4$ (open circles) and on $ScAlMgO_4$ with a $Mg_{0.15}Zn_{0.85}O$ buffer layer (filled circles) and that of a ZnO single crystal (cross) at room temperature (after Ohtomo et al. and Tsukazaki et al. [9, 37]).

tration is controlled by incorporation of foreign atoms either on lattice or interstitial sites in the crystal structure of the semiconductor. Effective substitutional doping requires [17]

- solubility of the dopant atoms in the host lattice,
- low activation energy of the dopant,
- and absence of compensating intrinsic defects.

The solubility of the dopant in the host lattice is generally large when there is only a small difference in effective ionic radii of the host and impurity atoms. A compilation of effective ion radii taking into account the oxidation states as well as coordination number within the crystal is provided by Shannon [39]. For example, in the case of substitutional n-type doping of $BaSnO_3$, the maximum La solubility in $BaSnO_3$ is only about 3 at.% [40], which is attributed to the smaller effective La^{3+}

cation (1.36 Å) as compared to the Ba^{2+} cation (1.61 Å). A prominent example for interstitial defects is incorporation of H, which behaves as a compensating impurity in most semiconductors, but can donate electrons in ZnO, SnO_2 and also $BaSnO_3$ (see chapter 4 of this thesis).

One of the greatest challenges in wide-band gap semiconductor technology is to be able to achieve both, good p-type and n-type conduction for the same material, which is essential for preparation of complimentary pn homojunction devices. For example, the fabrication of high-efficiency UV LEDs is difficult because hole activation in Mg-doped $Al_xGa_{1-x}N$ with high Al content is low and the doping efficiency decreases further with increasing magnitude of the band gap [41].

The ease of doping is determined by the localized energy level of the dopant with respect to the band edges as schematically shown in Fig. 1.7. Taking the example of Mg-doped $Al_xGa_{1-x}N$, the dopant level indicates the Fermi energy for the charge transition of the neutral defect Mg^0_{Al} to the ionized acceptor defect Mg^-_{Al} under equilibrium conditions. Since the $(0/-)$ charge transition level lies well above the valence band (VB) maximum, a considerable activation energy for ionization of the defect is required. Dopants with a shallow energy level (e.g. Li acceptor in NiO [42]) or a state inside the band (e.g. La donor in $BaSnO_3$ [43]) are much more effective in providing free carriers for the electrical transport. In the latter case, the electrons localized at the defect level inside the continuum of host bands may relax and lower their energy to the conduction band edge [44]. Because the conduction band of the host is perturbed by the energy of the defect level inside the band states, such donors are termed resonant with the conduction band (CB).

In the case of n-type doping of $BaSnO_3$ with La, the energy level presents the Fermi energy at which the $(+/0)$ charge transition of the ionized donor La^+_{Ba} to the neutral La^0_{Ba} impurity occurs under equilibrium conditions (cf. section 1.4.2). When the Fermi level lies below the La dopant energy level, La impurities will readily form

ionized La^{+}_{Ba} to contribute to the reservoir of free electrons. Only when the Fermi level is raised significantly to exceed the La dopant energy level, La atoms will remain as neutral impurities in $BaSnO_3$ without providing additional free carriers.

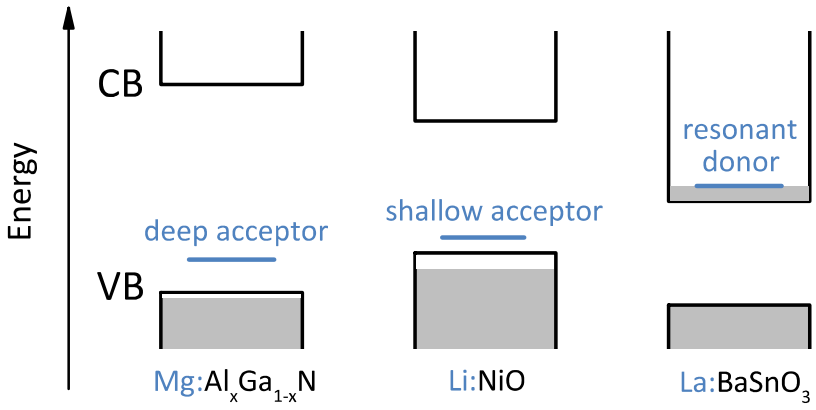


Fig. 1.7: Schematic diagram of the energy levels of Mg, Li and La impurities in $Al_xGa_{1-x}N$, NiO and $BaSnO_3$, respectively. The shallowness of the impurity level (charge transition level) with respect to the band edges determines the ease of doping.

Spontaneous formation of native defects can compensate the free carriers which are introduced by the donor or acceptor impurities [45–48]. If the formation enthalpy of an intrinsic compensating defect is smaller than the energy gain of creating the free electron (or hole), carriers will instantaneously be compensated under equilibrium conditions. A schematic diagram of the variation of defect formation enthalpy with Fermi energy level is shown in Fig. 1.8. In the case of introducing donor impurities, the increase in free electron concentration raises the Fermi level and consequently the formation energy of an intrinsic acceptor defect α^{-} such as a cation vacancy will decrease. The doping limit is determined by the Fermi level energy at which acceptor defects α^{-} will have net zero formation energy and form spontaneously. Same considerations hold for the case of acceptor doping which can be compensated by formation of intrinsic donors α^{+} such as anion vacancies. The corresponding Fermi

energy level which determines the maximum doping level is called pinning energy E^{pin}. From the schematic diagram it becomes clear that doping with free electrons (holes) without compensation by intrinsic defects is only possible when the Fermi level pinning energy $E^{\mathrm{pin}}_{\mathrm{n(p)}}$ lies within the CB (VB).

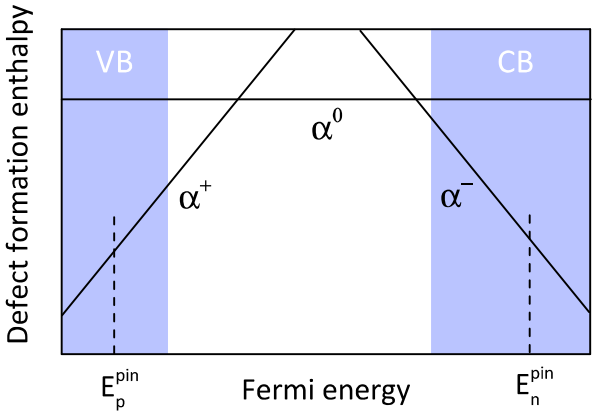


Fig. 1.8: Schematic diagram of the formation enthalpy of an intrinsic defect α with charge states +, 0 and − as a function of Fermi energy (reproduced after Zunger [48]). The Fermi level pinning energies $E^{\mathrm{pin}}_{\mathrm{p}}$ and $E^{\mathrm{pin}}_{\mathrm{n}}$ determine the maximum doping limits.

The exact level of the Fermi pinning energy with respect to the band edges varies depending on the specific semiconductor, but comparing the relative positions of valence band maxima and conduction band minima of all materials is useful to discuss doping propensities. The band alignment for relevant wide-band gap III-V nitride, II-VI oxide and chalcogenide, perovskite stannate and III-VI sesquioxide semiconductors is shown in Fig. 1.9, adopting the band offsets reported in Refs. [42, 49–52].

As a general rule it holds that semiconductors with a small electron affinity have CB minima that lie comparably high in energy and are difficult to dope n-type (e.g. AlN). Vice versa, those semiconductors with large work functions have VB maxima that lie comparably low in energy and are difficult to dope p-type (e.g. ZnO, SnO_2, $BaSnO_3$,

In_2O_3). Taking ZnO as an example, p-type doping under equilibrium conditions is not possible since the VB maximum lies well below the Fermi level pinning energy E_{pin}^{p} and O vacancies and Zn interstitials will spontaneously form when holes are introduced by acceptor doping [53]. It is rare to find semiconductors for which both n-type and p-type doping can be readily achieved despite their large band gap (e.g. GaN).

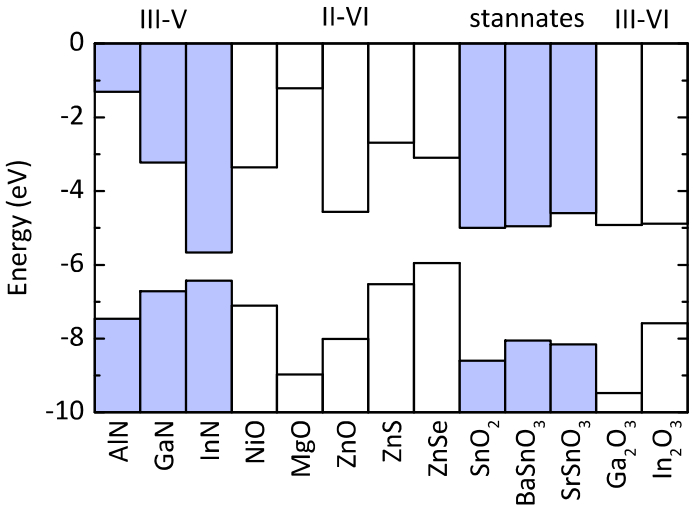


Fig. 1.9: Energy band alignment of group III-V, II-VI and stannate wide-band gap semiconductors with reference to the vacuum level (adopting the band alignments reported by van de Walle et al. [49], Robertson et al. [50], Lany et al. [42], King et al. [51] and Bjaalie et al. [52]).

1.2.3 Electronic Band Structure

First-principles density functional (DFT) theory provides a powerful tool for a better understanding of the electronic properties of semiconductors. Elaborate models allow for detailed calculations of the defect formation energies and electronic band structure of semiconductors which help to explain their optical and electronic properties. The knowledge of the electronic band structure of a semiconductor helps to assess its

relevance for specific applications before any experimental investigations are carried out or can suggest synthesis of previously undiscovered materials for which desirable properties are expected.

An example of a computer-calculated electronic band structure of wurtzite GaN is shown in Fig. 1.10. At the Γ point of the Brillouin zone the VB maximum and CB minimum coincide making GaN a *direct* band gap semiconductor, which is a highly desirable attribute for application in optoelectronics. Since the electronic band structure relates the energy E of an electron to its wave vector $\mathbf{k}$, a different $\mathbf{k}$-vector implies a difference in momentum ($\mathbf{p} = \hbar\mathbf{k}$). Upon photoexcitation with an energy larger than the band gap, an electron can be excited from the top of the VB to a higher energy state at the bottom of the CB, leaving behind a hole. In a two-particle process, the direct transition in GaN allows for efficient radiative recombination of electrons in the CB with holes in the VB because the momentum is conserved as indicated by a vertical transition in an E-$\mathbf{k}$ diagram.

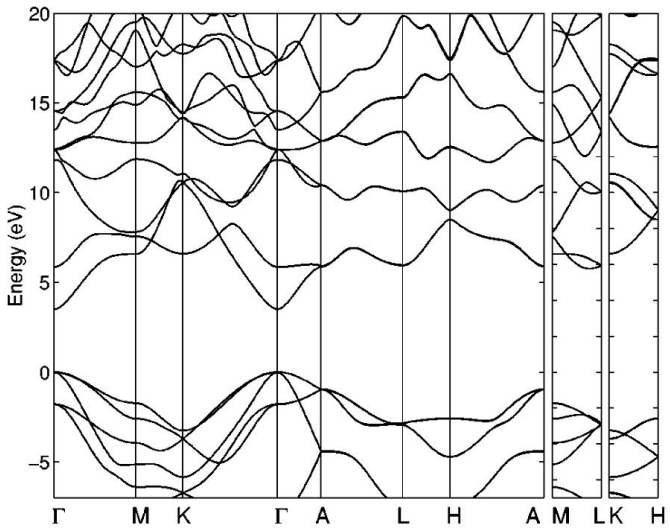


Fig. 1.10: The electronic band structure of wurtzite GaN along the high symmetry lines of the first Brillouin zone (after Goano et al. [54]).

In contrast, for indirect semiconductors like Si the VB maximum and CB minimum

are located at different positions of the Brillion zone. In the case of recombination of an electron and a hole via an indirect transition, the emission of a photon must be mediated by phonons to comply with the conservation of momentum. As a result, the probability of radiative recombination in indirect band gap semiconductors is significantly reduced in comparison to non-radiative recombination processes via defects. Furthermore absorption of light with an energy close to the band gap in an indirect semiconductor is less efficient and thus absorption layers in solar cells composed of indirect semiconductors (e.g. Si) must be thicker than those composed of direct semiconductor photovoltaics (e.g. GaAs). It follows that the nature of the fundamental electronic band gap is an important criterion for realization of high efficiency optoelectronic devices, for which direct band gap materials are generally preferred.

Another important conclusion can be drawn from the shape of individual bands comprising the electronic structure of semiconductors as given in E-$\mathbf{k}$ diagrams. Materials with good electrical transport properties are characterized by carriers having a small effective mass m^*, since according to Newton's law

$$F = m\frac{dv}{dt} \tag{1.1}$$

the acceleration $\frac{dv}{dt}$ of an electron in an electric field with force F will be large. The velocity of a particle is given by the group velocity [55]

$$\frac{d\omega}{dk} = \frac{d(E/\hbar)}{dk} \tag{1.2}$$

where ω is the angular frequency of the particle with energy $E = \hbar\omega$ and $\hbar$ is the reduced Planck constant. Derivation of Eq. (1.2) after time yields the acceleration

$$\frac{dv}{dt} = \frac{1}{\hbar^2}\frac{d^2E}{dk^2}\frac{dp}{dt} \tag{1.3}$$

where $p = \hbar k$ is the electron momentum. Comparing Eq. (1.3) with (1.1), it is seen that the electron effective mass

$$m^* = \hbar^2\left(\frac{d^2E}{dk^2}\right)^{-1} \tag{1.4}$$

is inversely proportional to the second derivative of energy E(**k**) after wave vector **k**. As a consequence, a strong curvature of the CB minimum (VB maximum) in the electronic structure indicates a small electron (hole) effective mass and a large carrier mobility.

The energy band diagram of SnO_2 shows a wide-band gap and highly dispersive CB minimum indicating a large electron mobility making it a prototype transparent conductor (Fig. 1.11). However, the relatively flat and localized O 2p orbital derived energy bands comprising the VB maximum indicate a small hole mobility which is a common feature of many oxide semiconductors.

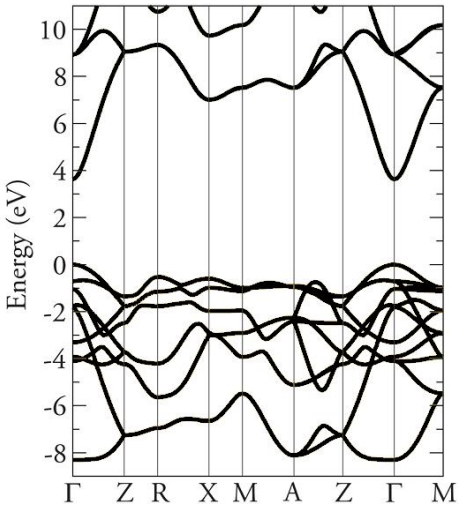


Fig. 1.11: The electronic band structure of rutile SnO_2 along the high symmetry lines of the first Brillouin zone (after Scanlon et al. [56]).

The problem of achieving reasonable p-type conductivity presents the bottleneck for the development of pn junction devices based on semiconducting oxides. The most promising materials with reasonably good p-type conductivity are Cu-based oxides and oxychalcogenides, like $CuAlO_2$ [57], $SrCu_2O_2$ [58] and LaCuOS [59]. In these, Cu 3d and S 3p orbitals merge with the O 2p orbitals comprising the top of the valence band result in a greater band dispersion (Fig. 1.12). However, the reported

hole mobilities of ~10 Vs/cm^2 at maximum are lower by up to two orders of magnitude as compared to the high electron mobilities found in n-type semiconducting oxides ZnO, SnO_2, $BaSnO_3$ and In_2O_3.

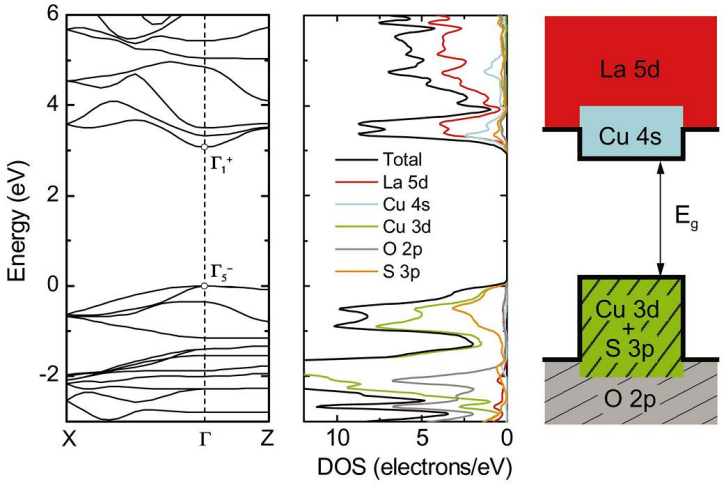


Fig. 1.12: Energy band diagram and partial density of states of LaCuOS as well as a schematic band structure diagram (after Ueda et al. [59]).

1.2.4 Light Emission

When a current is applied to a pn junction semiconductor diode, photons with a wavelength determined by the energy of the band gap may be emitted by radiative recombination of electrons in the CB and a holes in the VB. Free electrons or holes can be introduced by doping, but may also be formed by excitation with light of a wavelength corresponding to an energy larger than the band gap. The generated electron-hole pair exists as free electron and hole at elevated temperature, but may be spatially confined by weak Coulomb interaction at low temperature [1]. The bound electron-hole pair is called an exciton and is associated with a defined binding energy characteristic for the material.

The probability of the radiative recombination process of electrons and holes de-

termines the light emission efficiency of a semiconductor. The tendency to exciton emission is an intrinsic property which is independent of the nature of the band gap. Semiconductors with an exciton binding energy of more than about 25 meV show a comparably large concentration of electron-hole pairs at room temperature and are generally brilliant light emitters (e.g. GaN, ZnO and diamond). The exciton binding energy can be calculated applying the hydrogen atom model assuming spherical and non-degenerate energy surfaces for the electron and hole. The exciton binding energy level of order n referred to the CB minimum is given by [60]

$$E_{\mathrm{b}} = -\frac{e^4}{2h^2\varepsilon_0^2 n^2}\left(\frac{1}{m_{\mathrm{e}}} + \frac{1}{m_{\mathrm{h}}}\right) \tag{1.5}$$

where h is the Planck constant, ε_0 is the static dielectric constant, m_{e} and m_{h} are the electron and hole effective masses, respectively. In theory, a high exciton binding energy is expected for semiconductors with a small dielectric constant and small carrier effective masses (Tab. 1.1).

To enhance the radiative recombination probability of electrons and holes, narrow quantum well structures are employed which may increase the exciton binding energy by carrier confinement [68]. A double heterostructure LED employs an active light emitting region comprised of a multi quantum wells to locally confine electron and holes to enhance light emission efficiencies [69]. Preparation of such quantum well structures requires facile band gap tuning and it is therefore beneficial if the semiconductor can be alloyed with isostructural compounds of similar lattice parameter, but different band gap (e.g. GaN and $\mathrm{Ga_xIn_{1\text{-}x}N}$ or ZnO and $\mathrm{Zn_xBe_{1\text{-}x}O}$).

Table 1.1: Optoelectronic and dielectric properties of important semiconductors and wide-band gap materials.

Material	Band gap*		Exciton binding energy	Dielectric constants	
	E_g (eV)		E_b(meV)	ε_0	ε_∞
Si[a]	1.1	i	15	11.7	11.7
GaAs[a]	1.4	d	4.2	13.1	10.9
GaN[b]	3.4	d	25	8.9	5.4
ZnO[b]	3.4	d	60	8.8	3.8
ZnSe[b]	2.7	d	20	9.1	6.3
NiO[c]	3.7†	d	-	11.8	5.7
MgO	7.8[d]	d	-	9.8[e]	3.0[f]
$BaSnO_3$[g]	3.1	i	-	19	3.3
3C-SiC[h]	2.4	i	14	9.8	6.5
Diamond[i]	5.5	i	80	5.5	5.5

*At room temperature, d = direct, i = indirect.
†This value refers to the optical direct band gap which is by about 0.2 eV larger than the indirect band gap calculated by DFT.
[a]Reference [60].
[b]Reference [61].
[c]Reference [62].
[d]Reference [63].
[e]Reference [64].
[f]Reference [65].
[g]Reference [66].
[h]Reference [67].
[i]Reference [1].

1.3 NiO and $Ni_xMg_{1-x}O$

1.3.1 Structural Properties

NiO and MgO both crystallize in the cubic rock-salt structure with very close lattice parameters resulting in a small structural mismatch of merely ∼0.8 % (Tab. 1.2). The effective Mg^{2+} ion radius is only marginally greater than the effective Ni^{2+} ion radius and thus the ions easily substitute each other to form a homogeneous $Ni_xMg_{1-x}O$ solid solution over the entire composition range [70]. The calculated phase diagram of the NiO-MgO solid solution indicates full miscibility [71] with liquidus and solidus lines confirmed by experiment [72] (Fig. 1.13).

Table 1.2: Comparison of lattice parameters and effective cation radii in NiO and MgO.

Material	Structure	Lattice constant (Å)	Effective cation radius (Å)
NiO	rock-salt	4.177[a]	0.69[b]
MgO	rock-salt	4.212[a]	0.72[b]

[a]Reference [70].
[b]Reference [39].

1.3.2 Electronic Structure

A precise description of the electronic structure of transition metal oxides like NiO presented a challenge for conventional theory calculations. Since the Ni^{2+} ion has $3d^8$ electron configuration with octahedral coordination to O 2p orbitals, the 3d-orbitals are energetically split into two degenerate e_g and three degenerate t_{2g} orbitals which may be filled with 4 and 6 electrons, respectively. Thus one would expect metallic conduction in NiO as some of the resulting orbitals will be only partially filled with electrons. In a first theory Mott suggested that conduction in NiO occurs by charge transfer of Ni 3d electrons between Ni^{3+} and Ni^{+} ions after electron-hole pairs have

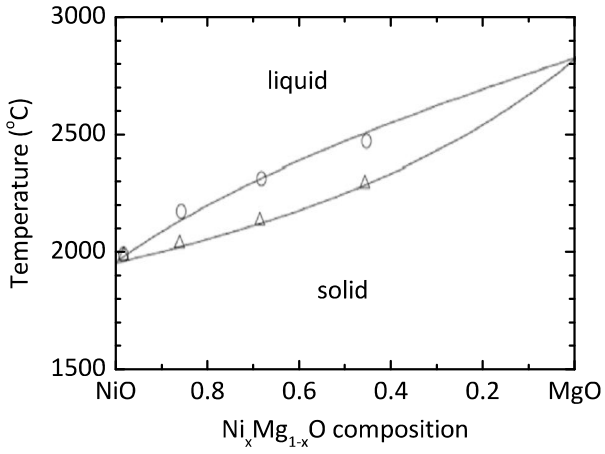


Fig. 1.13: Calculated NiO-MgO phase diagram (after Prostakova et al. [71]) with experimental data points of the solidus and liquidus line (after Wartenberg et al. [72]).

been created [73]. NiO is insulating at low temperature because the creation of such electron-hole pairs requires thermal activation. The magnitude of activation energy required for charge transfer of 3d electrons is associated with the forbidden energy gap.

Later it has then been demonstrated that the NiO band gap can not specifically be attributed due to Coulomb and exchange interactions among 3d electrons of Ni ions. Since it has been realized the band gap is largely determined by the electronegativity of the O anion, charge fluctuations in NiO were suggested to result from charge-transfer of an electron from an O^{2-} anion to a Ni^{2+} cation and creation of a hole in the anion valence band [74,75]. It has been shown that conduction in transition metal compounds can be classified into Mott-insulators with electron and holes moving in d bands and charge-transfer insulators with holes in the anion valence band and electrons in d bands [76]. NiO belongs to the group of charge-transfer insulators since the d-d Coulomb interaction is greater than the charge-transfer energy, and the band gap is shown to be roughly proportional to electronegativity of the O^{2-} anion.

The calculated electronic band structure of NiO using a hybrid functional approach,

excelling in the improved treatment of the electron exchange interaction as compared to other electronic structure theories, is shown in Fig. 1.14(a) [77]. The top of the VB is mainly comprised of Ni 3d states and O 2p states while the CB minimum is of pure Ni 4s character with a parabolic band dispersion. It shall be noted that the energy of the unoccupied and rather localized Ni 3d e_g states in the presented band structure lie high in energy as compared to other calculations in which the bottom of the CB is comprised of a mixture of Ni 3d and Ni 4s states [78]. NiO shows a calculated indirect band gap of about 3.9 eV between the VB maximum at the Z-point and the CB minimum at the Γ point and a direct gap of 4.1 eV at the Γ point of the Brillouin zone.

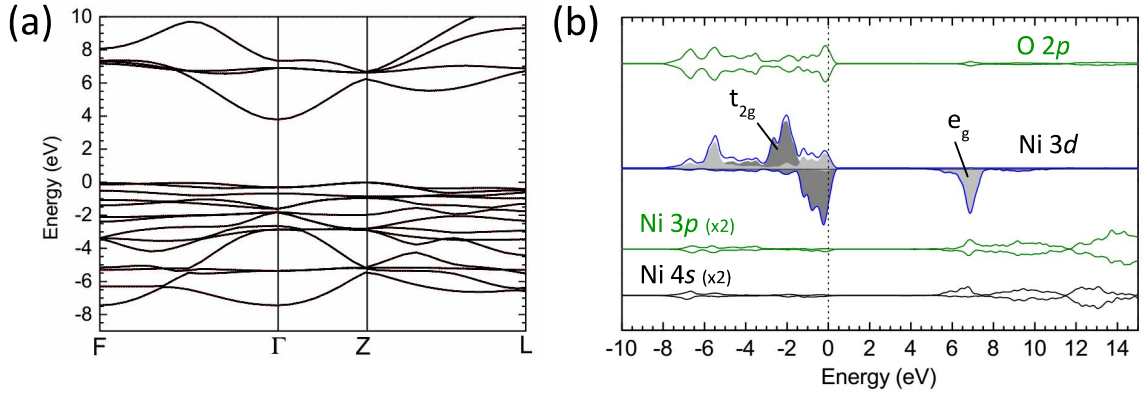


Fig. 1.14: (a) Calculated electronic band structure for NiO along the high symmetry lines of the first Brillouin zone. (b) Calculated spin-resolved local density of states for NiO with Ni 3d states decomposed into contributions from t_{2g} (dark grey) and e_g (light grey) orbitals (after Gillen et al. [77]).

The calculated local density of states (DOS) diagram indicates that the fundamental band gap of NiO can be attributed to transitions from O 2p or Ni 3d e_g and t_{2g} states at the top of the VB to unoccupied Ni 3d e_g and Ni 4s states at the bottom of the CB (Fig. 1.14(b)). The DOS diagram also shows that the opening of the NiO band gap is mainly attributed to the crystal-field splitting of Ni 3d states into lower-energy

occupied e_g and t_{2g} states and higher-energy e_g states.

The composition of the MgO electronic band structure is much more simple because only main group element 2s and 2p orbitals are involved. The local density approximation (LDA) yields a direct band gap of 5.2 eV at the Γ point of the Brillouin zone (Fig. 1.15(a)) [79]. Due to the largely ionic character of bonding in MgO, such a large band gap is expected. However, the LDA underestimates the band gap as compared to the experimental value of 7.8 eV [65]. The partial density of states at the top of the VB is mainly derived from O 2p orbitals while the bottom of the CB is characterized by Mg 2s orbitals and a large hybridization between Mg and O.

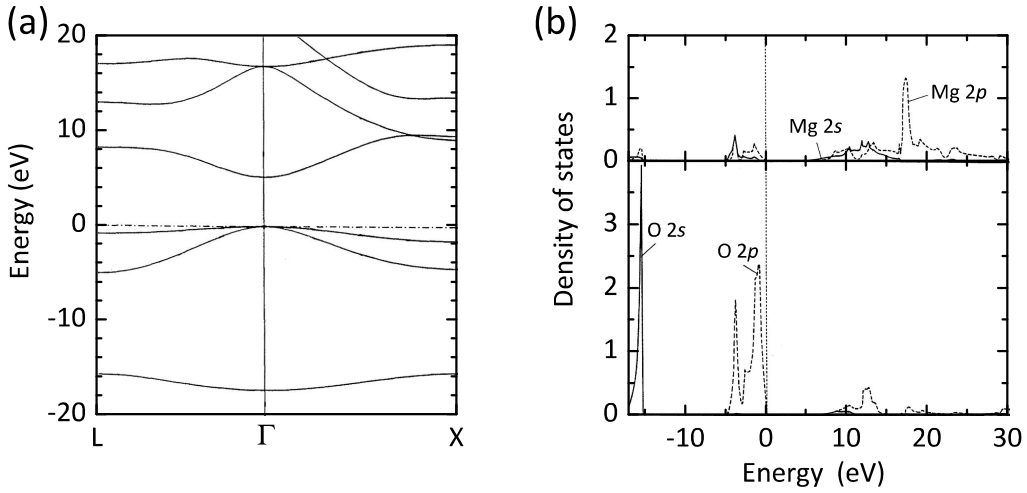


Fig. 1.15: (a) Calculated electronic band structure for MgO along the high symmetry lines of the first Brillouin zone. (b) Calculated partial local density of states for MgO decomposed into contributions from Mg and O 2s and 2p orbitals (after Schönberger et al. [79]).

As compared to many other semiconductor alloys, the wide-band gap $Ni_xMg_{1-x}O$ system is unique in demonstrating an enormous flexibility for band gap tuning from 3.7 eV to 7.8 eV in the deep UV spectral region, while maintaining complete miscibility over the entire composition range with only a negligible change in lattice

parameter. Despite the very similar structural properties, the electronic configuration of NiO and MgO is distinctly different. Thus it is of interest to investigate the electronic structure and band gap behaviour of $Ni_xMg_{1-x}O$ alloys, which will be the subject of chapter 3 in this thesis.

1.3.3 Defect Chemistry and Doping

NiO is known to exhibit intrinsic p-type conductivity due to its non-stoichiometry with a deficiency of Ni cations [80]. It presents one of the few p-type semiconducting oxides with sufficiently good electrical transport properties for application as hole injection layer in heterojunction devices, for example in combination with ZnO to prepare UV photodetectors and light-emitting diodes [81, 82]. However, even though NiO thin films can be doped with intrinsic defects to hole concentrations of ca. 1×10^{19} cm^{-3} [83], the carrier mobility of $\sim$3 Vs/cm^2 is low as compared to n-type oxide semiconductors.

The defect chemistry of NiO has been investigated by theoretical calculation of defect formation energies as a function of Fermi level (Fig. 1.16(a)) [42]. Under O-rich conditions the Ni vacancy V_{Ni} is the most stable defect with formation energies smaller than 1 eV even for Fermi levels close to the VB maximum and p-type doping is not compensated by intrinsic donors such as O vacancies due to the large formation energy. Thus the Fermi level pinning energy E_p^{pin} lies well inside the VB indicating that holes can be introduced without compensation (Fig. 1.16b), which is facilitated by the high VB maximum energy (low ionization potential) of NiO. The peroxide $(O_2)_O$ species, which can be thought of as an interstitial O atom O_i displacing a lattice O atom to form a dumbbell structure, will not play a role since it is high in formation energy and of neutral charge for all Fermi levels considered.

P-type conduction in NiO shall be more effective when Ni atoms are substituted with

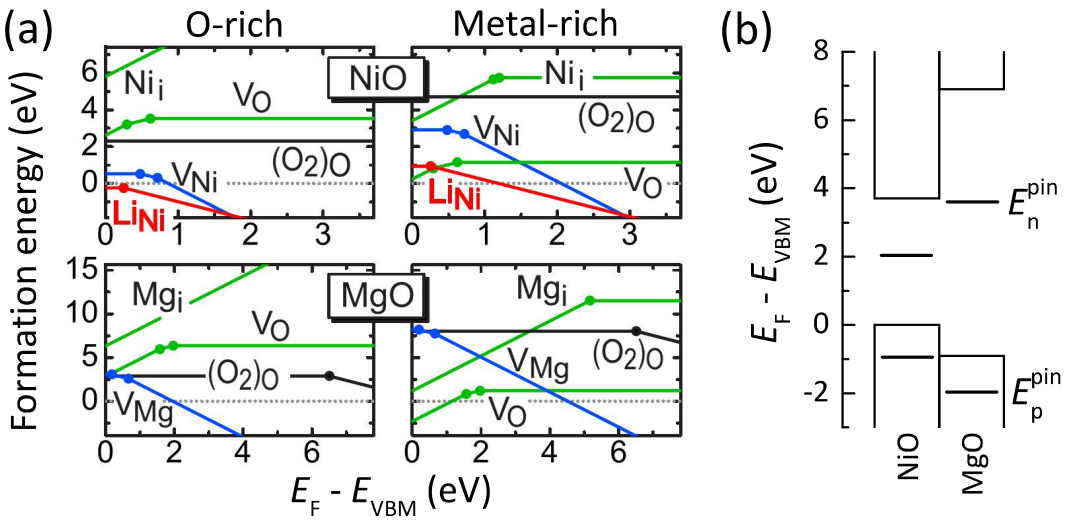


Fig. 1.16: (a) Calculated defect formation energies as a function of Fermi level in NiO and MgO under O-rich and metal-rich conditions. (b) Calculated band offsets between NiO and MgO and corresponding Fermi level pinning energies $E_{\mathrm{n}}^{\mathrm{pin}}$ and $E_{\mathrm{p}}^{\mathrm{pin}}$ (after S. Lany et al. [42]).

Li impurities ($\mathrm{Li_{Ni}}$), since the calculation demonstrates a smaller formation enthalpy of $\mathrm{Li_{Ni}}$ as compared to $\mathrm{V_{Ni}}$. The reduced $\mathrm{Li_{Ni}}$ activation energy in comparison with $\mathrm{V_{Ni}}$ is indicated by the shift of the $(0/-)$ charge transition level to smaller Fermi energies. N-type doping of NiO is not possible, because free electrons would be readily compensated by $\mathrm{V_{Ni}}$ acceptors and thus the Fermi level pinning energy $E_{\mathrm{n}}^{\mathrm{pin}}$ lies well inside the band gap.

For MgO grown under O-rich conditions, intrinsic Mg vacancies or O vacancies in MgO have a large formation energy of 3 eV and MgO is expected to be stoichiometric. Under metal-rich conditions, O vacancies may form easily due to their low 1 eV formation energy. However, free electrons are not introduced due to the deep donor levels (high activation energy) and these would readily be compensated by formation of Mg vacancies which is indicated by the pinning energy $E_{\mathrm{n}}^{\mathrm{pin}}$ well below the MgO CB edge. Since the pinning energy $E_{\mathrm{p}}^{\mathrm{pin}}$ of MgO lies within the VB no compensation

by intrinsic defects is expected if free holes were introduced. However, MgO cannot be easily doped p-type because the VB edge lies very low in energy and thus the Mg vacancy level forms acceptor states that lie deep inside the gap [84]. N-type doping of MgO is also not possible, because electrons would be compensated by spontaneous formation of V_{Mg} acceptors and thus the Fermi level pinning energy E_n^{pin} lies well inside the band gap.

While the p-type conduction in Li-doped NiO has been well investigated [83, 85], this thesis will further investigate the hole transport properties in Li-doped $Ni_xMg_{1-x}O$ for band gap widening beyond 3.7 eV (see appendix of this thesis). Good hole transport characteristics in band gap-tunable $Ni_xMg_{1-x}O$ could open up new path ways for designing transparent optoelectronic devices such as wavelength-tuneable UV photodetectors [86–90].

1.4 $BaSnO_3$

1.4.1 Crystal Structure and Electronic Structure

The stannate $BaSnO_3$ crystallizes in an undistorted cubic perovskite structure, which is described by a three-dimensional network of corner-sharing $[SnO_6]^{2-}$ octahedra of 180° Sn−O−Sn bond angle with Ba^{2+} cations filling the cubo-octahedral gaps in coordination to 12 O^{2-} anions (Fig. 1.17(a)) [91]. The calculated electronic band structure of $BaSnO_3$ is presented in a fatband diagram, in which orbital contributions to the corresponding bands are indicated by coloured hatched areas as shown in Fig. 1.17(b). The band structure indicates an indirect allowed band gap between the M and Γ point and a direct allowed band gap at the Γ point of the Brillouin zone. Accurate Perdew-Burke-Ernzerhof (PBE) exchange-correlation functional calculations indicate indirect and direct band gaps of 3.2 eV and 3.7 eV, respectively [43].

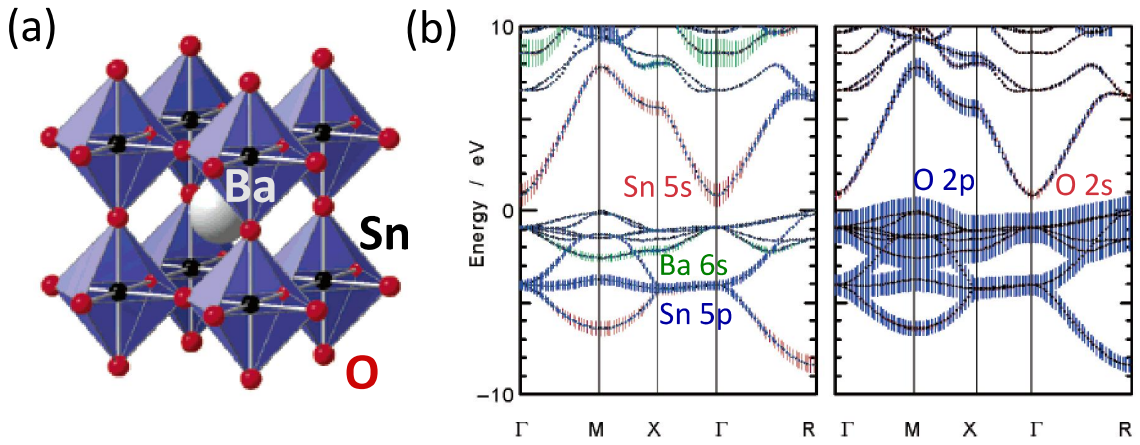


Fig. 1.17: (a) Ideal cubic $BaSnO_3$ perovskite composed of a three-dimensional corner-sharing $[SnO_6]^{2-}$ octahedral network and 180° Sn−O−Sn bond angle. (b) Calculated electronic band structure of $BaSnO_3$ indicating orbital contributions in a fatband presentation. Left diagram: Contributions of Sn 5s (red), Sn 5p (blue) and Ba 6s (green) orbitals to the $BaSnO_3$ electronic band structure. Right diagram: Contributions of O 2s (red) and O 2p (blue) orbitals to the $BaSnO_3$ electronic band structure (after Mizoguchi et. al [91]).

At the Γ point of the Brouillin zone, the bottom of the CB shows a parabolic, free electron-like band dispersion arising from the Sn 5s orbital which is characteristic for high mobility n-type oxide semiconductors of closed d-shell $(n\text{-}1)d^{10}ns^0$ electron configuration, where n indicates the principal quantum number. The next higher electronic bands at the Γ point derived from Sn 5p and Ba 6s orbitals lie several eV above the CB minimum and thus a high optical transparency is expected for $BaSnO_3$. The top of the VB is dominated by contributions of rather localized O 2p orbitals giving rise to flat energy bands for which hole conduction is very difficult. Based on these results presented in 2004 it could already be predicted that $BaSnO_3$ would show great promise as high mobility n-type TCO. However, rising interest in $BaSnO_3$ as n-type semiconductor did not arise until 8 years later when an extraordinarily

high Hall mobility of up to 320 Vs/cm^2 had been reported for La-doped $BaSnO_3$ single crystals [19, 92]. The delay in $BaSnO_3$ research may be due to the fact that excellent electronic transport requires preparation of high quality crystals, while it is considerably deteriorated in polycrystalline $BaSnO_3$. This indicates that the oriented structure with an ideal cubic three-dimensional network of $[SnO_6]^{2-}$ octahedra is a prerequisite for the large mobilities.

1.4.2 Defect Chemistry and Doping

The defect chemistry of $BaSnO_3$ has been investigated using a hybrid density functional theory by calculation of intrinsic and extrinsic defect formation energies as function of Fermi level [43]. Under metal-rich conditions, the oxygen vacancy V_O is the most stable donor, but the (+2/0) charge transition lies below the CB minimum and good n-type conductivity in $BaSnO_3$ is unlikely to result from O deficiency (Fig. 1.18(a)). However, one experimental study reports mobilities of 20 cm^2/Vs at a doping level of 5×10^{19} cm^{-3} for vacuum annealed $BaSnO_3$ films which has been attributed to formation of O vacancies [93]. Under O-rich conditions, formation of electrons by V_O will be compensated by formation of the acceptor V_{Ba} and the Fermi-level is pinned well inside the band gap (Fig. 1.18 (b)). It follows that p-type conduction in $BaSnO_3$ is impossible to achieve and excellent n-type conduction may require doping with extrinsic defects more shallow than V_O.

The calculated formation energies of relevant extrinsic impurities for n-type doping of $BaSnO_3$ such as H, F, Sb and La as a function of Fermi level is shown in Fig. 1.18(c). Under metal-rich conditions, H_O, interstitial H (H_i) bound next to an O atom, Sb_{Sn}, La_{Ba} and F_O all have low formation energies even for a high Fermi level and form shallow donors without compensation by acceptor defects. While La is known to be an effective donor in $BaSnO_3$ [19–25], no studies of H or F doping to $BaSnO_3$ films

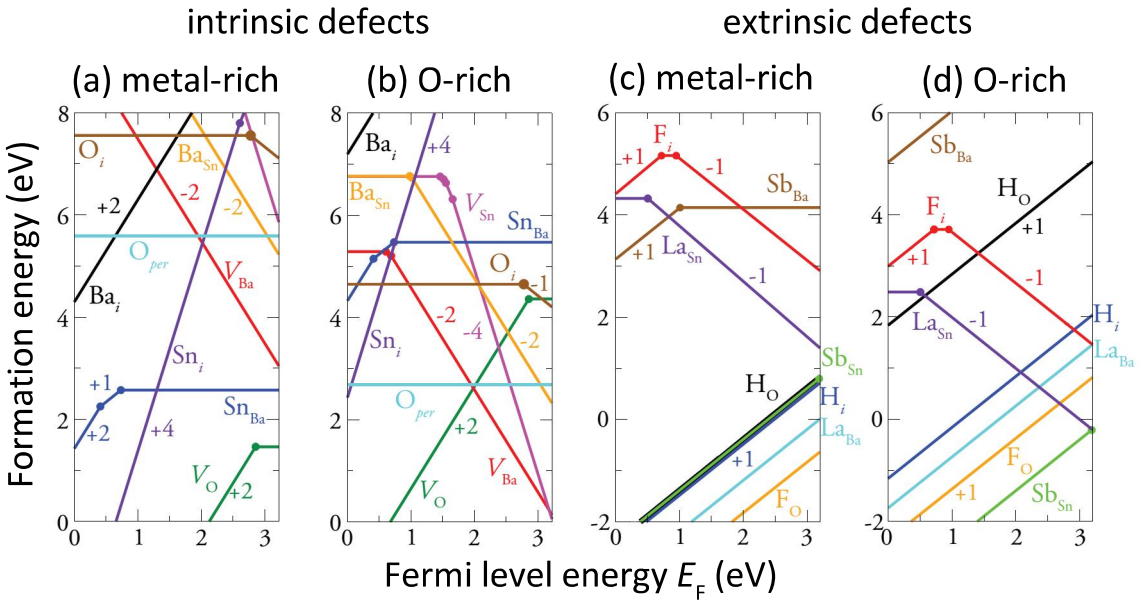


Fig. 1.18: Formation energy of intrinsic defects in $BaSnO_3$ under (a) metal-rich and (b) O-rich conditions, as well as that of extrinsic defects upon doping of $BaSnO_3$ with H, F, La or Sb under (c) metal-rich and (d) O-rich conditions as a function of Fermi level. The slope of the lines represent the defect charge state and the solid dots indicate the charge transition levels (after Scanlon [43]).

have yet been presented. The first experimental investigation of H doping to $BaSnO_3$ films will be presented in chapter 4 of this thesis.

Among all extrinsic impurites, the solubility of F_O in $BaSnO_3$ is the largest and high doping levels may be expected, but the high growth temperatures required for $BaSnO_3$ epitaxy lead to F evaporation. Because the Sb_{Sn} (+1/0) charge transition level is just below the CB minimum, it is not an effective donor when the Fermi level is increased. This observation is corroborated by experimental studies confirming that Sb doping on the Sn site is generally less preferred than La doping on the Ba site [94].

Under O-rich conditions, the formation energies of H_O, H_i, La_{Ba} and F_O all increase resulting in a smaller solubility in $BaSnO_3$ (Fig. 1.18(d)). The donor Sb_{Sn} becomes

more stable under O-rich conditions, but the (+1/0) charge transition level is close to the CB minimum. Moreover, the acceptor defect La_{Sn} can now lead to compensation and thus O-rich growth conditions are less preferred for achieving good n-type conductivity.

1.4.3 Thin Film Epitaxy and Electrical Transport Properties

The superior electrical transport in $BaSnO_3$ can only be fully exploited when the material is prepared either as bulk single crystal or epitaxial thin film. Since $BaSnO_3$ single crystal substrates are yet to be developed, the preparation of $BaSnO_3$-based devices requires heteroepitaxial thin film growth on structurally matched crystals. The lattice parameters of cubic and pseudocubic crystal oxides with close matching to the $BaSnO_3$ perovskite are shown in Fig. 1.19. $SrTiO_3$ substrates were chosen for most investigations since it is isostructural with $BaSnO_3$ and widely available, but a large lattice mismatch of 5.4 % must then be tolerated, resulting in a high dislocation density [95]. By using orthorhombic rare-earth scandate substrates like $PrScO_3$, the mismatch with $BaSnO_3$ can be reduced to 2.3 %, but these are very expensive. Growth of $BaSnO_3$ thin films on rocksalt MgO substrates provides an option for reducing the mismatch to only 2.3 % with tensile strain in the films, however, electrical transport properties comparable to those films grown on perovskite substrates have not yet been reported. In chapter 5 of this thesis, growth of $BaSnO_3$ films on MgO substrates is presented, applying a NiO buffer layer to further reduce the mismatch to only 1.4 %.

Up to present, La:$BaSnO_3$ thin films prepared by pulsed laser deposition (PLD) show mobilities of 70 cm^2/Vs when grown heteroepitaxially on $SrTiO_3$ substrates [96] and 100 cm^2/Vs when grown homoepitaxially on $BaSnO_3$ substrates [24] (Fig. 1.20). For the latter, enhanced mobilities are attributed to the improved crystal quality and smaller defect concentrations resulting in reduced electron scattering and

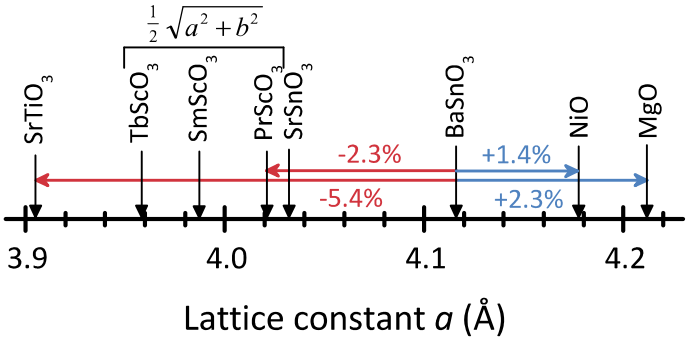


Fig. 1.19: Comparison of lattice parameters of (pseudo)cubic crystals with close lattice matching to cubic perovskite $BaSnO_3$.

a lower density of carrier traps. This argument is corroborated by comparison with the enhanced mobilities observed for La:$BaSnO_3$ single crystals at intermediate carrier concentrations of about 3×10^{20} cm^{-3} and below. For doping levels above 3×10^{20} cm^{-3}, the mobility is dominated by ionized impurity scattering in both, epitaxial La:$BaSnO_3$ thin films and single crystals. In contrast to the high energetic PLD method, MBE allows for preparation of high crystal-quality La:$BaSnO_3$ thin films with record Hall mobilities of 150 cm^2/Vs on $PrScO_3$ substrates at a doping level of only 7.3×10^{19} cm^{-3} [25].

The choice of thin film growth method and substrate both have a large impact on the electron transport in $BaSnO_3$ epitaxial thin films. While it has been recognized that the reduced mobilities may be largely attributed to dislocation scattering [95], a fundamental quantitative analysis of the prevailing scattering mechanisms is still lacking and would be of great importance for the design of high mobility transport layers in devices. The electron mobility μ in a semiconductor is determined from the equilibrium electron drift velocity obtained after the acceleration force due to the applied potential and the friction force due to scattering effects are in balance. It is described by [55]

$$\mu = \frac{e\tau}{m_e^*} \tag{1.6}$$

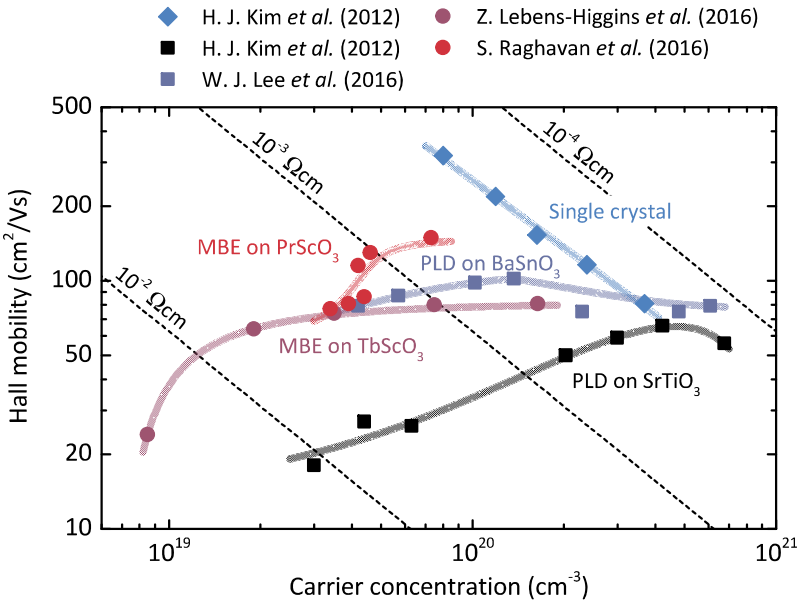


Fig. 1.20: Dependence of Hall mobility on carrier concentration for La-doped $BaSnO_3$ thin films prepared by PLD on $SrTiO_3$ substrates (in black, after Kim et al. [19]) and $BaSnO_3$ substrates (in purple, after Lee et al. [24]) as well as films prepared by MBE on $TbScO_3$ substrates (in brown, after Lebens-Higgins et al. [23]) and $PrScO_3$ substrates (in red, after Raghavan et al. [25]). The mobility of La-doped $BaSnO_3$ single crystals is given for comparison (in blue, after Kim et al. [19]). Dashed lines indicate constant values of electrical resistivity.

where m_e^* is the electron effective mass and τ is the momentum relaxation time denoting the average time of momentum loss by scattering. Chapter 5 of this thesis will present an in-depth evaluation of the $BaSnO_3$ electron effective mass m^* as a function of carrier concentration and find an analytical description for the momentum relaxation time τ. The results shall contribute to the design of low-defect density, high mobility epitaxial films at moderate doping levels for application in oxide electronics such as field-effect transistors.

2 Experimental Methods

2.1 Thin Film Growth using Pulsed Laser Deposition

Pulsed laser deposition (PLD) presents a facile method for epitaxial thin film growth using a wide range of materials, in particular oxides. The material source is a dense, sintered ceramic target usually prepared by solid state powder processing. A 248 nm KrF excimer laser is focussed in pulses of 25 ns duration at a frequency of 10 Hz on the target with a laser beam fluency of $\sim$1 J/cm^2. The pulsed laser shots quickly heat the subsurface of the ceramic target to temperatures of $\sim 10^5$ K. Because of the rapid thermal expansion the top surface of the target breaks into atoms, atom clusters and ions forming a dense laser-induced plasma plume and a highly directional material flow towards the substrate in 5 cm distance opposite to the target (Fig. 2.1).

The thin film growth is performed in a high vacuum deposition chamber in which the O_2 partial pressure can be controlled within the range of $0.1 - 25$ Pa. The background O_2 gas serves as a reactive species for oxide growth and at the same time offers to control the kinetic energies of particles in the plasma plume [97]. The substrate temperature is controlled with an IR laser diode heating an absorber in contact to the back of the crystal substrate. The great advantage of PLD as compared to more sophisticated deposition techniques such as MBE and electron beam evaporation is the stoichiometric transfer of material from the target to substrate. Beyond a certain ablation threshold energy of the laser beam, the vaporization of the target material is

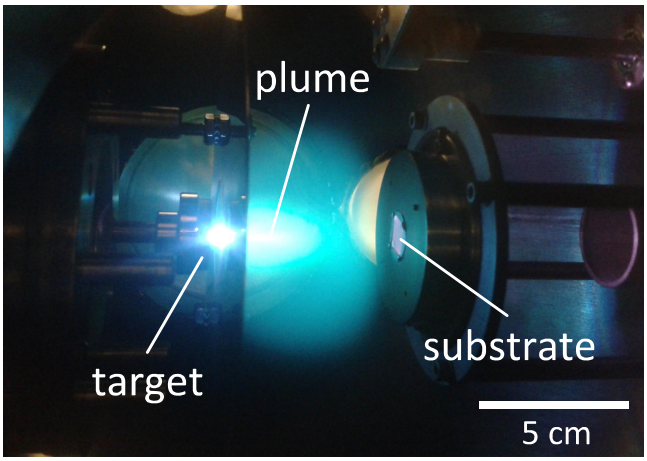


Fig. 2.1: Experimental set-up of pulsed laser ablation of a ceramic oxide target by a 248 nm KrF laser for epitaxial thin film growth on a heated single crystal substrate.

independent of the vapour pressure of its constituent elements and thus a wide range of complex oxides can be deposited while maintaining the stoichiometric composition of the target.

2.2 High Resolution X-ray Diffraction

High Resolution X-ray Diffraction (HR-XRD) is a very powerful crystal characterization method for assessing the quality of epitaxially grown thin films. It is a non-destructive method and requires only minimum sample preparation. To generate X-rays, electrons are accelerated by a high voltage towards a water-cooled Cu cathode to trigger electronic transitions in Cu atoms whose inner K shell electrons have been ionized by the high energy electron irradiation. A Ni filter is used to absorb all radiation with energies above the $Cu_{K\alpha}$ X-ray lines and a monochromator mirror system composed of Ge single crystals is used to separate the $Cu_{K\alpha 1}$ (1.5406 Å) from the $Cu_{K\alpha 2}$ (1.5444 Å) radiation. After diffraction at the crystal, the elastically scattered X-rays pass through a parallel beam slit collimator in front of the detector to filter

out any non-parallel beam components of the diffracted beam which could lead to diffraction peak broadening and thus the resolution of the instrument is increased.

An incident beam of monochromated X-ray radiation is scattered elastically from a crystal if the path length difference between two X-rays diffracted at a family of crystallographic planes is a multiple of the X-ray wavelength λ (Fig. 2.2), according to Bragg's law:

$$n\lambda = 2d_{\mathrm{hkl}} \sin\theta \tag{2.1}$$

where n is the order of diffraction, d_{hkl} is the lattice spacing of the respective crystallographic plane with Miller indices hkl and θ is the angle of incidence between lattice plane and incoming X-rays [98].

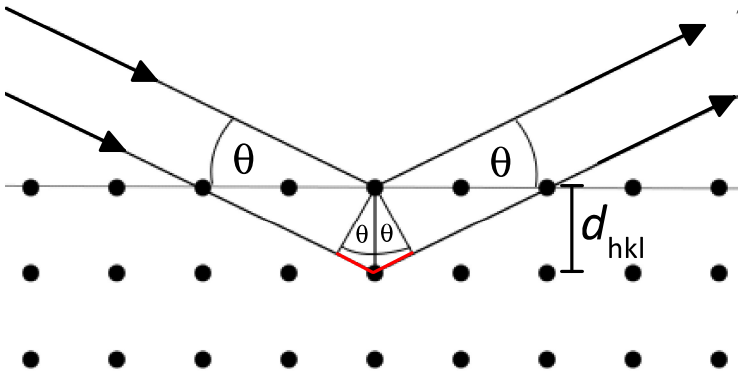


Fig. 2.2: Schematic illustration of elastic scattering of X-rays at lattice planes of atoms in a simple cubic crystal.

Epitaxial thin films are generally grown on lattice-coherent single crystal substrates and a mismatch of the crystal structure will result in strain affecting the film lattice parameters. To understand the results of X-ray diffraction analysis in detail, it is useful to consider the reciprocal lattice of the crystal, providing the structural information along all crystallographic directions. The components of the scattering

vector **Q** are obtained by [99]

$$Q_{\mathrm{x}} = \frac{2\pi}{\lambda}\left(\cos(2\theta - \omega) - \cos(\omega)\right), \tag{2.2}$$

and

$$Q_{\mathrm{z}} = \frac{2\pi}{\lambda}\left(\sin(2\theta - \omega) + \sin(\omega)\right), \tag{2.3}$$

where λ is the X-ray wavelength, θ is the diffraction angle and ω is the angle between specimen surface and incident X-rays (Fig. 2.3). The scattering vector **Q** is determined by the direction and length $2\pi/\lambda$ of incident and reflected wave vectors $\mathbf{k}_{\mathrm{i}}$ and $\mathbf{k}_{\mathrm{r}}$, and it follows that only those diffraction peaks are accessible which lie within the Ewald sphere of radius $2|\mathbf{k}|$.

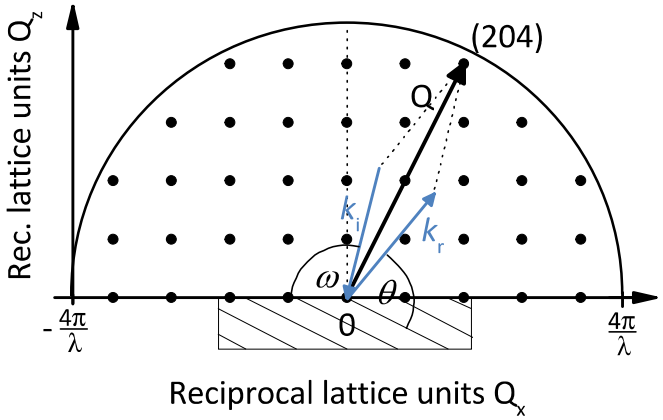


Fig. 2.3: Ewald sphere with radius $2|\mathbf{k}| = 4\pi/\lambda$ determining the accessible range of the reciprocal lattice of a crystal employing an X-ray wavelength λ. The 204 diffraction by elastic scattering at (102) lattice planes of a crystal is given as an example. The diffraction angle is θ and the angle between specimen surface and incident X-rays is ω. The scattering vector **Q** is defined by the difference of reflected and incident wavevectors $k_{\mathrm{r}} - k_{\mathrm{i}}$.

In a symmetric diffraction experiment ($\omega = \theta$), the reciprocal scattering vector **Q** is oriented perpendicular to the specimen surface, corresponding to diffraction at crystallographic planes (00l) parallel to the surface. In this case, only information about

the out-of-plane lattice parameter a_z is obtained. The crystal quality can be investigated by rocking the specimen through a change in ω, which provides information about the crystal mosaicity. A broad ω-rocking curve indicates crystallographic domains in the film with lattice planes not well aligned with the single crystal substrate surface. In an asymmetric diffraction experiment ($\omega \neq \theta$), further information about the in-plane lattice parameters a_x and a_y is obtained, which allows for characterization of the strain state of the epitaxial film. For a cubic crystal, the lattice parameter a is obtained by [100]

$$Q = \frac{2\pi}{a}\sqrt{h^2 + k^2 + l^2}. \tag{2.4}$$

When a highly monochromatic or variable energy X-ray source is required, synchrotron radiation is used which employs X-rays being generated from acceleration of electrons confined to a circular trajectory by a magnetic field. By employing a longer X-ray wavelength, fewer diffraction spots will be accessible since they fall outside the Ewald sphere, but the spatial resolution between diffraction signals is improved.

2.3 Atomic Force Microscopy

Atomic force microscopy (AFM) is used to obtain topographical images of the surface of a thin film. A sharp probe tip is physically brought in contact with the specimen surface and line scans on a raster map are performed to obtain height information. A visible laser is focused on the back side of a cantilever with the probe tip and any physical deflection due to interaction with the specimen is recorded by a change in location of the signal on a photodiode detector (cf. Fig. 2.4). The force between the specimen surface and cantilever is then related to the change in the position of the laser spot detected by the detector [101].

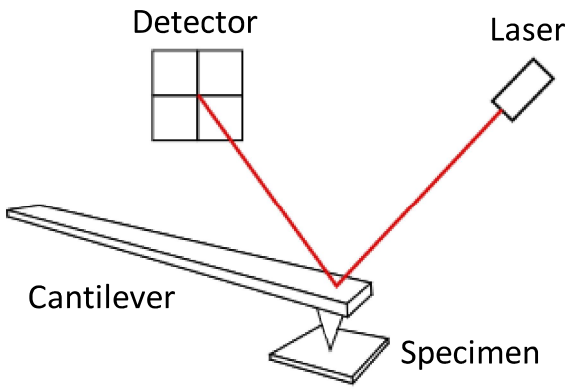


Fig. 2.4: Schematic diagram of atomic force microscopy using an optical lever sensor.

2.4 Energy Dispersive X-ray Spectroscopy

Energy dispersive X-ray spectroscopy (EDX) is a technique available in many scanning electron microscopes (SEM) to investigate the chemical composition of a specimen [102]. Upon interaction of a high energy electron beam ($5 - 20$ keV) with the specimen, inner shell electrons of atoms may be removed and subsequent electron transition to deeper energy levels of the atoms occur upon release of X-ray radiation (Fig. 2.5). The X-rays are detected with a Si solid state detector and are characteristic for a specific chemical element due to the defined energy levels for atoms of different atomic number.

To evaluate the elemental composition of a specimen, characteristic X-ray emission lines for the elements are selected which ideally appear at different energies and thus can be resolved without peak overlap and also exhibit high intensities to be clearly distinguished from the spectrum's radiation background. For a precise quantitative analysis of the specimen composition, reference intensities from a series of specimens of standard (known) compositions are recorded to determine sensitivity factors for the corresponding X-ray emission lines.

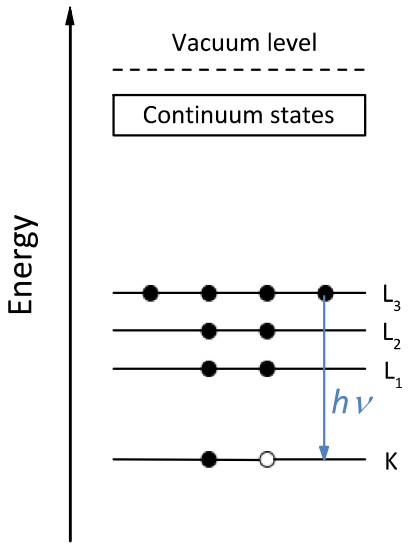


Fig. 2.5: Schematic diagram of energy levels in an atom that has been ionized by losing an inner K-shell electron due to excitation with a high energy primary electron beam. X-ray K_α emission occurs after the hole on the K-shell is filled by an electron from the L_3 shell (reproduced after Williams [102]).

2.5 Hall Effect Measurement

Hall effect measurements allow for a detailed investigation of the electrical transport properties of a semiconductor. When a current I_x is applied along the x-direction to a semiconductor sheet of geometric dimensions l_x, l_y and l_z and a magnetic field B_z is applied perpendicular to the flow of carriers with velocity v_x, the Lorentz force will deflect the trajectory of electrons (holes) to the negative (positive) y-direction (Fig. 2.6).

Due to carrier deflection by the magnetic field B_z, an electrostatic force will build up and a Hall voltage U_H can be measured along the y-direction. Under equilibrium conditions the electrostatic force will be in balance with the Lorentz force [55]

$$e\,\frac{U_H}{l_y} = e v_x B_z \tag{2.5}$$

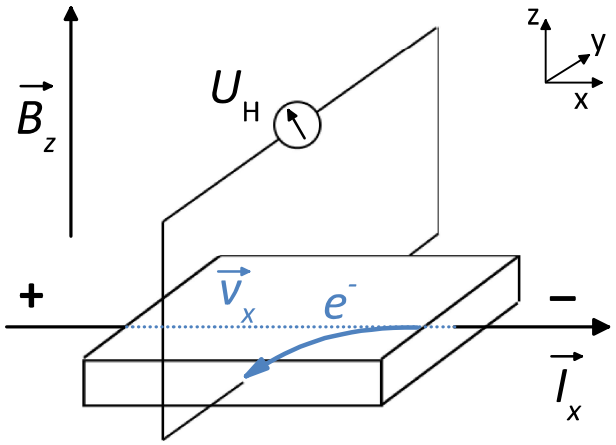


Fig. 2.6: Schematic depiction of the Hall effect in a thin semiconductor sheet through which a magnetic field B_z is applied perpendicular to the electrical current direction I_x.

where e is the electron charge. Since the current density along the x-direction is given by

$$\frac{I_x}{l_y l_z} = n e v_x \tag{2.6}$$

the free carrier concentration n per unit volume can be calculated from all experimental parameters:

$$n = \frac{I_x B_z}{e U_H l_z} \tag{2.7}$$

Once the carrier concentration n is known, the Hall mobility μ_H can be derived from the measured electrical conductivity σ

$$\sigma = n e \mu_H = \frac{\sigma}{R_H} \tag{2.8}$$

where $R_H = 1/ne$ is called the Hall constant.

From equation (2.8) it is seen that electrical conductivity can be improved by increasing the doping level or improving the Hall mobility. While high carrier concentrations can be readily achieved by introduction of more defects that provide free carriers, increasing the mobility is more difficult as it depends on the detailed scattering mechanisms of carriers. A method of understanding the electronic transport

in more detail is to apply temperature-dependent Hall measurements usually in the range of $4-300$ K as the free carrier concentration may sensitively depend on thermal activation. Furthermore, defects which present scattering centres may be identified as thermal activation is required to overcome potential barriers for carrier transport.

The measured Hall voltage as described above is assumed to be solely a result of the carrier displacement in the semiconductor due to the applied magnetic field. However, very precise measurements require taking into account the effects of thermal electrical voltages and misalignment voltages [103]. This is particularly important for semiconductors of low Hall mobility, because the magnitude of the Hall voltage will be small and comparable to the undesired voltages affecting the measurement. In this case, an alternating current (AC) magnetic field is applied and the undesired direct current (DC) voltages are separated from the resulting AC Hall voltage using a lock-in amplifier with reference to the magnetic field.

2.6 Optical Transmission and Reflection Spectroscopy

Optical transmission and reflection spectroscopy is a non-destructive and quick, but yet very powerful method for the electro-optical characterization of semiconductors. For the semiconductors investigated in this thesis, the optical absorption is calculated from transmission and reflectance spectra to determine the direct allowed optical band gap which for wide band gap semiconductors usually lies in the blue visible or UV spectral region. Furthermore, while TCOs are characterised by their optical transparency in the visible region, free carrier absorption can be observed in IR spectra for high doping levels.

The optical absorption is determined by measuring the transmission through the semiconductor and the reflectance at near-normal incidence (Fig. 2.7). The intensity loss is determined by the absorption coefficient α and thickness Δx of the material,

but also by the reflection loss at the semiconductor/vacuum interface both at the front- and backside of the semiconductor sheet. For thin films grown by vapour phase deposition only specular reflectance must be taken into account since generally they have very smooth, mirror-like surfaces for which diffuse reflectance is insignificant.

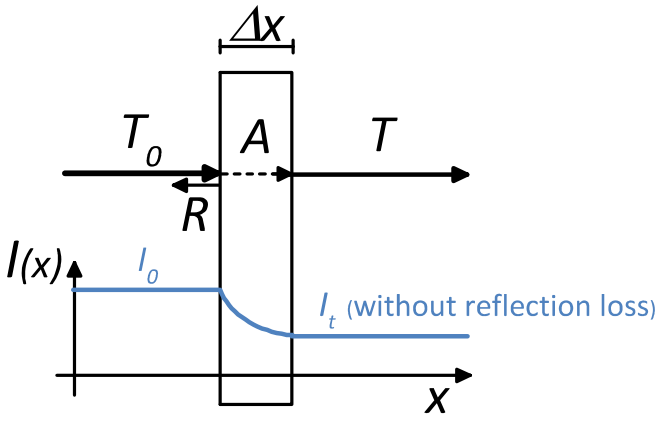


Fig. 2.7: Transmission of light through a material sheet of thickness Δx with reflections occurring at the vacuum/semiconductor interfaces and corresponding intensity profile without reflection loss.

The change in light intensity $dI/I(x)$ due to optical absorption in an infinitesimal small sheet dx is determined by

$$\frac{dI}{I(x)} = -\alpha dx \tag{2.9}$$

which after integration yields

$$I_\mathrm{t} = I_0 e^{-\alpha \Delta x} \tag{2.10}$$

where I_t and I_0 are the transmitted and initial intensities, respectively. The optical transmittance T can be related to the intensity ratio I_t/I_0 when the reflection loss R at the interface is taken into account [104],

$$T = (1-R) T_0 e^{-\alpha \Delta x} \tag{2.11}$$

where T_0 is the 100% intensity of the incident beam. A more refined analysis also takes into account the backside reflection at the interface after transmission through the specimen. However, the backside reflection is negligible when the back surface is roughened as is the case for one-side polished single crystal substrates.

From the transmittance and reflectance of the semiconductor sheet with known thickness, the refractive index n_r and extinction coefficient k_e is obtained from the Fresnel coefficients [105]. A normal incidence of the light for the transmittance and reflectance measurements is generally preferred as it largely simplifies the analytical equations. Even for a more complicated multilayer system, the optical constants for each layer may be obtained. The refractive index and extinction coefficient is related to the dielectric function $\varepsilon = \varepsilon_1 + i\varepsilon_2$ via equations [17]

$$n_\mathrm{r} = \sqrt{\frac{1}{2}\left(\varepsilon_1^2 + \varepsilon_2^2\right)^{1/2} + \frac{\varepsilon_1}{2}} \tag{2.12}$$

and

$$k_\mathrm{e} = \sqrt{\frac{1}{2}\left(\varepsilon_1^2 + \varepsilon_2^2\right)^{1/2} - \frac{\varepsilon_1}{2}}. \tag{2.13}$$

The dielectric function of a semiconductor does not only provide information about optical transitions such as the band gap, but further allows for the characterization of electron transport properties when the IR absorption of free carriers is investigated (cf. Fig. 1.2). The IR dielectric function of semiconductors with a high carrier concentration is described by the Drude free electron model [55]

$$\varepsilon(\omega) = \varepsilon_\infty - \frac{\varepsilon_\infty \omega_\mathrm{p}^2}{\omega^2 - i\gamma\omega}, \tag{2.14}$$

where ϵ_∞ is the high frequency dielectric constant, ω is the phonon frequency, ω_p is the plasma frequency and γ is the broadening frequency. The effective mass m_e^* which determines the electron mobility in Eq. (1.6) is determined by the plasma frequency via

$$m_\mathrm{e}^* = \frac{ne^2}{\varepsilon_0 \varepsilon_\infty \omega_\mathrm{p}^2}, \tag{2.15}$$

where n is the carrier concentration.

2.6.1 Ultraviolet-Visible-Near-Infrared Spectroscopy

In UV-VIS-NIR sprectroscopy the transmission and reflectance of a specimen is measured as a function of wavelength within the range of about 200 nm to 2500 nm. A deuterium gas-discharge and a quartz iodine incandescent lamps are used as light sources for the UV and VIS-NIR spectrum regions, respectively. A key element in the optical hardware of the spectrometer is a micro-machined diffraction grating for separation of light into its spectral components through a collimating and focussing mirror system as shown in Fig. 2.8. Different scanning wavelengths are selected by rotation of the diffraction grating which will change the wavelength in focus of the aperture.

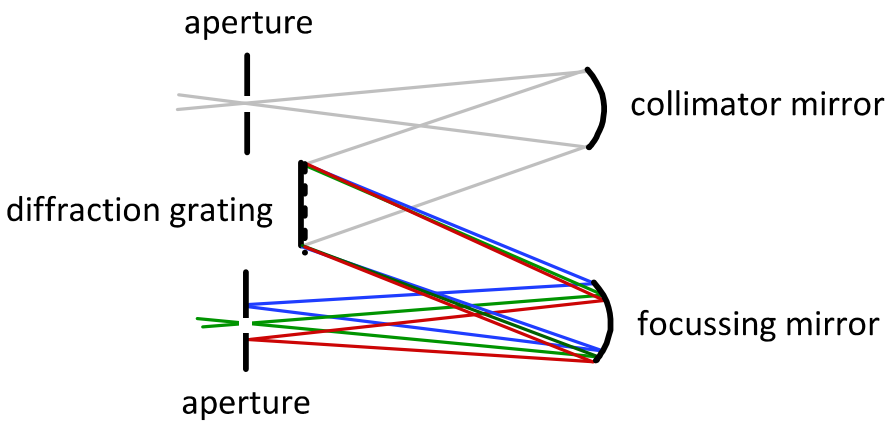


Fig. 2.8: Diffraction grating in an energy dispersive UV-VIS-NIR spectrometer.

2.6.2 Fourier Transform Infrared Spectroscopy

For measurements in the longer wavelength IR region, the use of a dispersive grating spectrophotometer is problematic since a whole set of gratings with different groove frequency would be required to cover a large region of the spectrum. To overcome these problems, Fourier transform IR (FTIR) spectroscopy employs non-monochromated light from a heated SiC element as black-body IR source.

An FTIR spectrometer employs a Michelson interferometer as shown in Fig. 2.9. The beam is split by a KBr crystal which shows 50% reflectance and 50% transmittance for the incoming light. The two beams are then again reflected back by mirrors for coalescence. One of the mirrors is moving to continuously increase or decrease the path length difference leading to periodically constructive and destructive wave interference of light of different wavelengths. With the help of Fourier transformation, the recorded interferogram, which relates intensity to the corresponding mirror position, is converted into a diagram relating the measured intensity to the wavelength. Since certain air molecules such as H_2O and CO_2 absorb IR light, the measurement is performed in a sealed and evacuated sample compartment.

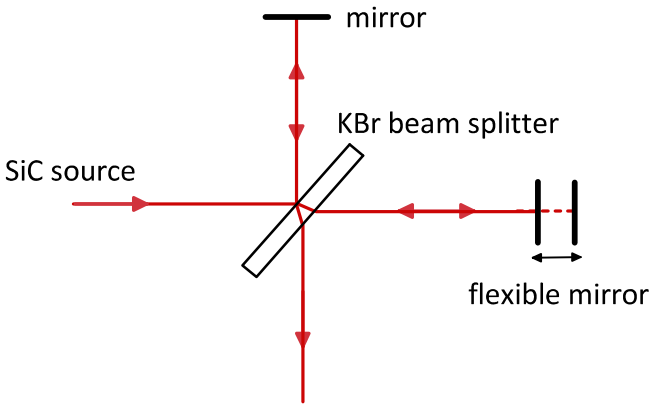


Fig. 2.9: Michelson interferometer in a FTIR spectrometer.

2.7 Spectroscopic Ellipsometry

Spectroscopic ellipsometry is used to determine thin film thickness and optical constants. It is a particularly powerful technique to characterise multilayer structures, for which the thickness of individual layers cannot be determined independently or for which the optical absorption of one of the layers interferes with characterization of

the other. A beam of linearly polarized light from a Xenon light source ($0.6 - 4.8$ eV) is irradiated at an incident angle of about $60 - 70°$ on the specimen surface and the change in polarization state of reflected light is analysed. After reflection and transmission through the specimen surface, the light becomes elliptically polarized and the relative change in amplitude and phase is measured (Fig. 2.10).

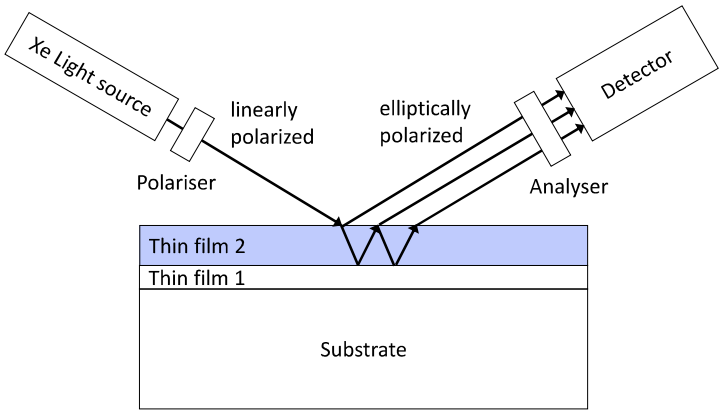


Fig. 2.10: Schematic set-up for ellipsometry measurement. Linearly polarized light from a Xenon lamp is reflected at the specimen surface and becomes elliptically polarized, which is analysed according to amplitude and phase change.

The reflected elliptically polarised light is characterized by two plane polarised waves [106]. The p-wave (p = parallel) is defined as lying in the plane of incidence and the s-wave (s = senkrecht, German for perpendicular) as lying perpendicular to the plane of incidence. The measured ellipsometry parameters $\tan\Psi$ and Δ denote the amplitude ratio and relative phase difference of incident and reflected p-wave and s-wave, respectively. The ratio of Fresnel reflection coefficients R_p and R_s according to the fundamental equation of ellipsometry given by

$$\tan\Psi \cdot \exp(i\Delta) = \frac{R_\mathrm{p}}{R_\mathrm{s}} \,. \tag{2.16}$$

Ellipsometry is an indirect method and a model of the specimen structure must be developed in order to derive absolute quantities such as the film thickness and the

optical constants of individual layers. By fitting appropriate dispersion models for the dielectric function of each layer to the corresponding amplitude ratio $\tan\Psi$ and relative phase change Δ in a least mean square error fitting routine, a set of absolute optical parameters is obtained which reproduces the recorded ellipsometry spectra the best.

3 Band Gap Bowing in $Ni_xMg_{1-x}O$

This chapter resolves the controversy over the origin of the non-parabolic $Ni_xMg_{1-x}O$ band gap bowing in the literature. High-resolution synchrotron X-ray diffraction and high-resolution transmission electron microscopy analysis of epitaxial transparent $Ni_xMg_{1-x}O$ ($0 \leq x \leq 1$) thin films indicate a compositionally and structurally homogeneous microstructure, confirming formation of a completely miscible solid solution. Nevertheless, the composition dependence of the $Ni_xMg_{1-x}O$ optical band gap shows a strong non-parabolic bowing with a discontinuity at dilute NiO concentrations of $x < 0.12$. It is suggested that deep Ni 3d levels are introduced into the MgO band gap, which account for the anomalously large band gap narrowing in the $Ni_xMg_{1-x}O$ solid solution system. While the standard bowing theory is inapplicable to describe the $Ni_xMg_{1-x}O$ band gap, the composition dependence is simply described by a linear interpolation of the band gaps of NiO and Ni impurity doped MgO.

3.1 Introduction

The wide-band gap semiconductor NiO (3.7 eV) is one of the few p-type transparent conductive oxides demonstrating good electrical properties for application in optoelectronic devices [83]. Thus NiO is used as a transparent hole transport layer in oxide p-n heterojunction devices such as electrical current rectifiers [107,108], ultraviolet (UV) photodetectors [81,109] and light-emitting diodes [110,111]. The epitaxial growth of high-crystal quality NiO thin films is desired, since polycrystalline films exhibit inferior electrical transport properties and may lead to higher leakage currents in p-n heterojunction devices.

The epitaxial growth of NiO on MgO single crystal substrates offers a promising platform for the preparation of complete UV-transparent oxide devices. Both NiO and MgO crystallize in the cubic rock-salt structure and $Ni_xMg_{1-x}O$ thin films over the entire composition range can be grown with high crystalline quality on MgO single crystals [88], having a structural mismatch of only 0.8 % at maximum [70]. As compared to many other semiconductor alloys, the $Ni_xMg_{1-x}O$ system is unique in demonstrating a great flexibility for band gap tuning from 3.7 eV to 7.8 eV [65] in the deep UV region without the drawbacks of a significant change in lattice parameter or a phase transition. Therefore, $Ni_xMg_{1-x}O$ is increasingly receiving interest for application in deep UV photodetectors [86–90]. To tune the photosensitivity of these devices, it is essential to understand the $Ni_xMg_{1-x}O$ band gap evolution as a function of composition and to be able to accurately describe it using an analytical equation.

Experimentally it has been shown that the band gap dependence in most semiconductor alloys or solid solutions $A_xB_{1-x}C$ as a function of composition x follows the parabolic function [112]

$$E_g = xE_g^{AC} + (1-x)E_g^{BC} - bx(1-x) \tag{3.1}$$

where E_g^{AC} and E_g^{BC} are the band gaps of the pure compounds AC and BC, respect-

ively, and b is the bowing parameter. Since the band gap of the semiconductor alloy is generally smaller than indicated by the linear interpolation between the band gaps of its pure end members, the bowing parameter b is a positive constant. It has been proposed that the band gap bowing results from the aperiodic variation of the crystal potential in substitutional alloys, arising from random variations in occupation of the metal sites in the alloy by elements A and B, and its magnitude is a symmetric function of composition proportional to $x(1-x)$ [113].

The $Ni_xMg_{1-x}O$ band gap dependence has been determined by optical absorption spectra of epitaxial thin films on MgO substrates prepared by molecular beam epitaxy [114], textured thin films on quartz substrates prepared by magnetron sputtering [90, 115] and sol-gel spin coated thin films on quartz substrates [116]. Despite the large 7.8 eV MgO band gap, it has been observed that the $Ni_xMg_{1-x}O$ band gap increases only marginally to 4.8 eV as the MgO fraction increases from $0-92$ at.%. A density functional theory (DFT) calculation of the $Ni_xMg_{1-x}O$ band gap dependence on composition has investigated superstructures with NiO contents of 25, 50 and 75 at.% [117]. However, since the study excludes the dilute NiO concentration regime for $x < 0.25$, no band gap discontinuity has been identified and the underlying $Ni_xMg_{1-x}O$ electronic band structure has not been investigated.

The present work resolves the controversy over the $Ni_xMg_{1-x}O$ band gap bowing in the literature. Regardless of the strongly non-parabolic band gap dependence on composition, the standard bowing theory has been rigidly applied in previous studies to describe the band gap evolution in the $Ni_xMg_{1-x}O$ system [86, 87, 90, 115, 117, 118]. Moreover, the origin of the irregular $Ni_xMg_{1-x}O$ band gap dependence has often been attributed to apparent structural or compositional inhomogeneities in $Ni_xMg_{1-x}O$ films [87,115,117]. Thus this chapter first presents a detailed investigation of the thin film microstructure before addressing the $Ni_xMg_{1-x}O$ electronic structure.

3.2 Experimental Methods

Single-phase polycrystalline $Ni_xMg_{1-x}O$ ceramic targets were prepared by sintering high purity NiO and MgO powders at temperatures of 1200 °C – 1550 °C for 5 h, applying higher temperatures for the targets of high MgO content. $Ni_xMg_{1-x}O$ thin films were grown on single crystal Si and MgO(100) substrates by pulsed laser ablation of the $Ni_xMg_{1-x}O$ ceramic targets using a 248 nm KrF excimer laser. The growth temperature was 600 °C and the deposition pressure was 0.7 Pa O_2. The growth conditions were taken from a previous study employing MBE growth of $Ni_xMg_{1-x}O$ [114] (300 – 700 °C, $2 \cdot 10^{-3}$ Pa), which aims for the preparation of insulating and optically transparent $Ni_xMg_{1-x}O$ epitaxial thin films and for the sole purpose of determining the optical band gap. An investigation of the electrical transport properties in conducting Li-doped $Ni_xMg_{1-x}O$ thin films is not subject of this chapter and will be given in the thesis appendix. As compared to high-vacuum MBE growth, the O_2 deposition pressure for PLD growth is increased due to experimental limitations and for achieving a sufficiently widespread plume. The $Ni_xMg_{1-x}O$ ceramic targets were ablated with a laser beam fluence of 0.8 J/cm^2 per pulse at a frequency of 10 Hz, resulting in a film thickness of about 300 nm.

The crystal structure of the $Ni_xMg_{1-x}O$ thin films on MgO substrates was studied by HR-XRD employing a Philips PANalytical MRD diffractometer equipped with a Cu-$K_{\alpha 1}$ X-ray source (1.5406 Å) utilizing parallel beam geometry. The structure and crystalline quality of the $Ni_xMg_{1-x}O$ thin films on MgO were further investigated by HR-XRD carried out on beamline B16 at the Diamond Light Source, UK, using a 6 keV (2.067 Å) monochromated X-ray source. 3-dimensional (3D) diffraction-space mapping [119] was used to investigate the structural homogeneity of the films. As compared to the 2D reciprocal space map analysis introduced in section 2.3, the 3D reciprocal lattice is recorded by introducing to rock the specimen along an additional,

third angle such that the y-coordinate Q_y of the scattering vector **Q** will be different from zero and thus tilted in- and outside of the paper plane in Fig. 2.3. 3D reciprocal space maps were calculated from the obtained data set which show the $Ni_xMg_{1-x}O$ 200 diffraction peak intensity as a function of the components of the two orthogonal in-plane components Q_x and Q_y and the out-of-plane component Q_z of the scattering vector in the specimen frame of reference.

The electron transparent cross-sectional TEM specimen was prepared by grinding, polishing and dimpling until the specimen thickness was below 10 μm, followed by Ar ion milling using a PIPS Ion miller (Gatan USA). Conventional HR-TEM and scanning transmission electron microscopy (STEM) using the high angle angular dark-field (HAADF) detector and STEM-energy dispersive X-ray spectroscopy (EDX) was performed using a JEOL 2100 microscope equipped with a field emission gun operating at 200 keV. STEM-HAADF imaging was used to identify the $Ni_xMg_{1-x}O$/MgO interface and STEM-EDX spectral analysis performed recording the Ni L_α, Ni L_β and Mg K_α X-ray emission lines.

The surface topography of the $Ni_xMg_{1-x}O$ thin films was investigated with a Bruker atomic force microscope (AFM) in contact mode. The composition of the $Ni_xMg_{1-x}O$ thin films was determined by EDX in a JEOL JSM-6010LA scanning electron microscope (SEM). Using a primary beam voltage of 5 kV, EDX spectra of the Ni L_α (852 eV), Ni L_β (869 eV) and Mg K_α (1254 eV) X-ray emission lines were recorded. The optical transmission of the $Ni_xMg_{1-x}O$ thin films were measured with a Cary 5000 UV-Vis-NIR spectrophotometer using a bare MgO substrate as 100% transmission reference.

3.3 Results

3.3.1 Structural Characterization

In the $\omega-2\theta$ HR-XRD patterns of the $Ni_xMg_{1-x}O$ thin films ($x = 1$, 0.83, 0.64, 0.41, 0.23, 0.12) only the 200 and 400 diffraction peaks are observed, indicating that films are single-phase and grown in [100]-orientation on the MgO(100) substrates (Fig. 3.1). Due to the marginal difference in lattice parameters between NiO (4.177 Å) and MgO (4.212 Å), [70] the $Ni_xMg_{1-x}O$ 200 and 400 diffraction peaks overlap with the corresponding peaks of the MgO substrate, especially for the $Ni_xMg_{1-x}O$ specimens of high MgO content. The insets show a clear shift of the $Ni_xMg_{1-x}O$ 200 and 400 diffraction peaks with increasing MgO fraction towards the MgO substrate peaks, indicating an increase in the out-of-plane lattice parameter.

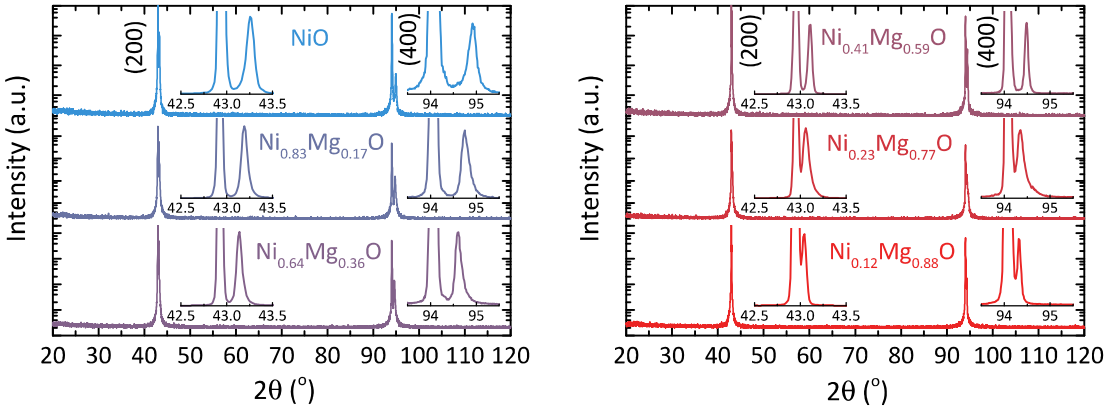


Fig. 3.1: HR-XRD $\omega-2\theta$ patterns of the $Ni_xMg_{1-x}O$ thin films ($x = 1$, 0.83, 0.64, 0.41, 0.23, 0.12) prepared by PLD showing the [100]-oriented epitaxial growth of $Ni_xMg_{1-x}O$ thin films on MgO(100) substrates. Insets show a magnification of the $Ni_xMg_{1-x}O$ 200 and 400 diffraction peaks on a linear scale.

The projection of the 3D reciprocal space maps of the $Ni_xMg_{1-x}O$ 200 reflection along the reciprocal lattice vector Q_x recorded with 6 keV synchrotron radiation is

given by an iso-intensity contour map on a logarithmic scale (Fig. 3.2). The increased X-ray wavelength of 2.067 Å as compared to the Cu $K_{\alpha 1}$ X-ray source of 1.5406 Å allows for a significantly improved spatial resolution of the high intensity 200 reflections of the $Ni_xMg_{1-x}O$ thin film and MgO substrate. Note that the observation of multiple peaks for the MgO 200 substrate indicates the presence of additional macroscopic crystallographic domains. The relatively narrow $Ni_xMg_{1-x}O$ 200 diffraction peak in the in-plane Q_y direction in reciprocal space as compared to the MgO substrate demonstrates the high crystalline quality and low degree of mosaicity of the thin films. In particular, the out-of-plane width of the $Ni_xMg_{1-x}O$ 200 diffraction peaks along Q_z ($x = 0.83$, 0.64 in Figs. 3.2(b,c)) does not indicate any compositional broadening as compared to the pure NiO thin film (Fig. 3.2(a)). The $Ni_xMg_{1-x}O$ 200 diffraction peak shifts to smaller Q_z values with increasing MgO content in accordance with the slight increase in lattice parameter from NiO (4.177 Å) to MgO (4.212 Å).

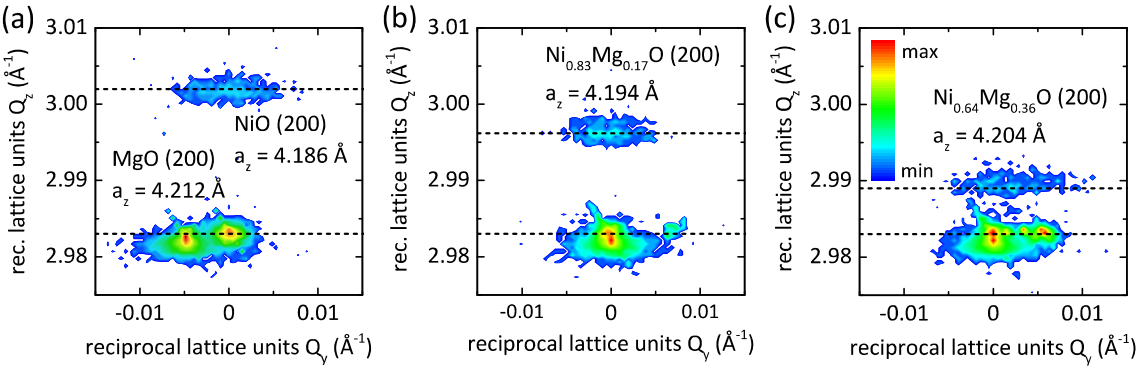


Fig. 3.2: Projection of the 3D reciprocal space maps of the $Ni_xMg_{1-x}O$ 200 reflection along the reciprocal lattice vector Q_x of $Ni_xMg_{1-x}O$ thin films (x = 1, 0.83, 0.64) grown on MgO(100) substrates recorded with 6 keV (2.067 Å) synchrotron radiation. The intensity of the diffraction peaks is given by an iso-intensity contour map on a logarithmic scale. The dashed lines give the local intensity maxima of the $Ni_xMg_{1-x}O$ 200 and MgO 200 diffraction peaks as indicated.

Reciprocal space map analysis of the asymmetric NiO 204 reflection shows that

the in-plane lattice parameter a_x is larger than the unstrained reference (Fig. 3.3). It follows that the $Ni_xMg_{1-x}O$ thin films are not completely relaxed, but strained to match the in-plane MgO substrate lattice parameter.

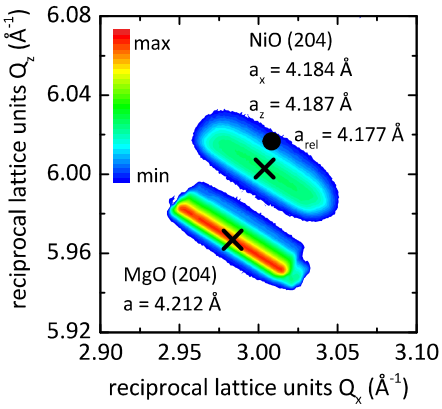


Fig. 3.3: Reciprocal space map of the NiO 204 reflection recorded with Cu $K_{\alpha 1}$ radiation (1.5406 Å). The intensity of the diffraction peaks is given by an iso-intensity contour map on a logarithmic scale. The given lattice parameters correspond to the maxima of the diffraction peaks of MgO substrate and NiO film (crosses) with reference to that of an unstrained NiO crystal (dot).

The offset-corrected AFM 3×3 µm^2 area scans of $Ni_xMg_{1-x}O$ (x = 1, 0.83, 0.64, 0.41 and 0.23) thin films are shown in Fig. 3.4. All films show atomically smooth surfaces with a root mean square mean roughness (RMSR) within $3 - 6$ Å, making them applicable for integration in multilayer device structures.

A cross-sectional STEM-HAADF image of the $Ni_{0.23}Mg_{0.77}O$ film on MgO substrate acquired along the <001> zone axis is shown in Fig. 3.5(a). To locate the $Ni_{0.23}Mg_{0.77}$/MgO interface, a STEM-EDX elemental map employing the Ni $L_{\alpha,\beta}$ (green) and Mg K_α (red) emission lines was recorded (Fig. 3.5(b)). The cross-sectional HR-TEM image of the $Ni_{0.23}Mg_{0.77}O$/MgO interface acquired along the <001> zone axis using multi-beam conditions shows coherency and a defect-free

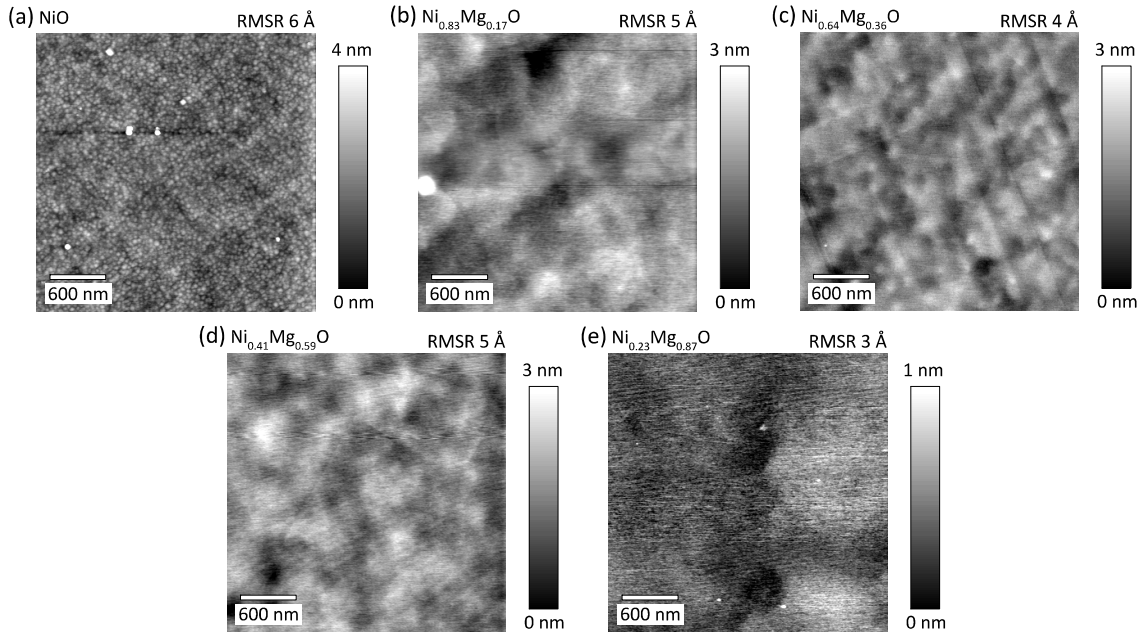


Fig. 3.4: Offset-corrected AFM 3×3 μm^2 area scans of $Ni_xMg_{1-x}O$ ($x = 1$, 0.83, 0.64, 0.41 and 0.23) thin films showing an atomically smooth surface.

$Ni_{0.23}Mg_{0.77}O$ bulk, demonstrating the single-domain epitaxy of the film on the MgO substrate (Fig. 3.5(c)). The very close lattice matching and coherent crystal interface between the $Ni_{0.23}Mg_{0.77}O$ film and MgO substrate is observed in the high magnification average background subtraction filtered (ABSF) HR-TEM image (Fig. 3.5(d)) of the region indicated in Fig. 3.5(c).

3.3.2 Compositional Analysis

The composition of the $Ni_xMg_{1-x}O$ thin films was determined from EDX spectra of the Ni L_α (852 eV), Ni L_β (869 eV) and Mg K_α (1254 eV) X-ray emission lines (Fig. 3.6(a)). The background-corrected, integrated peaks for all $Ni_xMg_{1-x}O$ thin films were evaluated based on a calibration curve obtained using data from the polycrystalline $Ni_xMg_{1-x}O$ targets of known composition. It was confirmed that the primary electron beam (5 keV) is entirely probing the $Ni_xMg_{1-x}O$ thin films and does

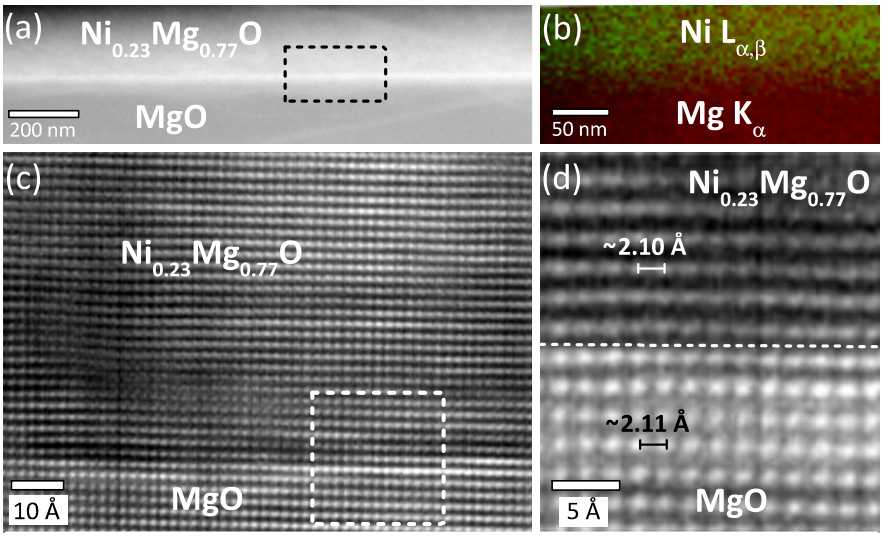


Fig. 3.5: (a) Cross-sectional STEM-HAADF image of the $Ni_{0.23}Mg_{0.77}O$/MgO interface acquired along the <001> zone axis and (b) STEM-EDX elemental map showing the Ni $L_{\alpha,\beta}$ (green) and Mg K_α (red) emission intensity for the area marked with the box in (a). (c) Cross-sectional HR-TEM image of the coherent $Ni_{0.23}Mg_{0.77}$/MgO interface acquired along the <001> zone axis demonstrating the single-domain epitaxial growth. (d) High magnification ABSF HR-TEM image of the region indicated with the box in (c). Micrographs were taken by S. Rhode, Imperial College London.

not reach the MgO substrate by investigating $Ni_xMg_{1-x}O$ thin films of equal layer thickness grown onto Si substrates for which the Si K_α emission (1740 eV) was not observed. The negligible deviation of the $Ni_xMg_{1-x}O$ thin film composition from that of the corresponding ceramic target confirms the near-stoichiometric ablation by the laser beam (Fig. 3.6(b)).

3.3.3 Composition Dependence of the Optical Band Gap

The optical transmission spectra of $Ni_xMg_{1-x}O$ thin films (x = 1, 0.83, 0.64, 0.41, 0.23, 0.17, 0.12) indicate about 80 % transparency in the visible and UV region

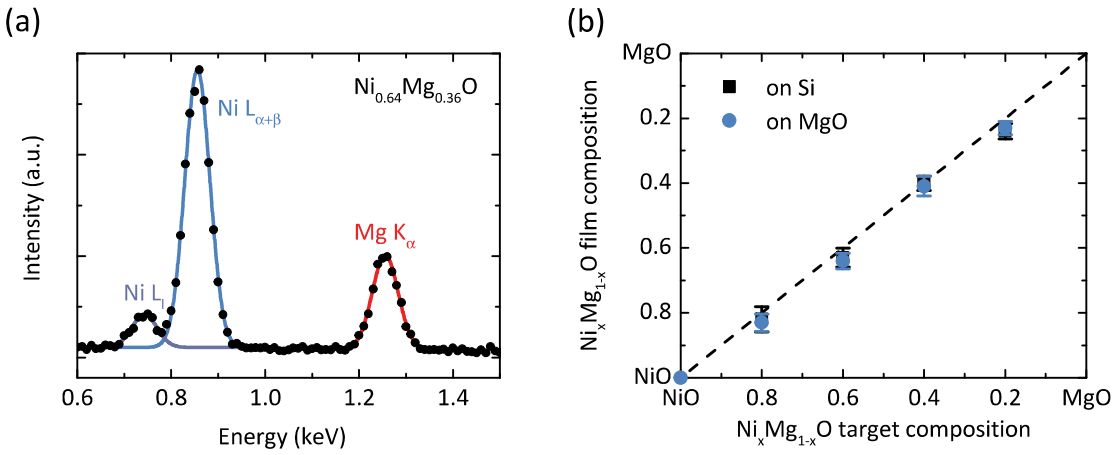


Fig. 3.6: (a) EDX spectrum of $Ni_{0.64}Mg_{0.36}O$ thin film on MgO substrate recorded with 5 keV primary electron beam energy. (b) EDX compositional analysis of $Ni_xMg_{1-x}O$ thin films grown on Si and MgO substrates in comparison to the corresponding ceramic target.

until the onset of their fundamental absorption (Fig. 3.7(a)). The optical absorption blue-shifts with increasing MgO content in the $Ni_xMg_{1-x}O$ thin films, from 340 nm for pure NiO to 200 nm for $Ni_{0.12}Mg_{0.88}O$. The absorption coefficient α is calculated from the transmission spectra and film thickness according to Eq. (2.11), neglecting the specular reflection at the specimen surface. The optical absorption spectra confirm the linear relationship between the photon energy $h\nu$ and $(\alpha h\nu)^2$, where α denotes the absorption coefficient, which is valid for direct transitions in semiconductors at the absorption edge (Fig. 3.7(b)) [120].

The growth conditions were chosen to prepare highly resistive and transparent $Ni_xMg_{1-x}O$ thin films with a negligible concentration of Ni vacancies V_{Ni} for the Ni-rich compositions that may reduce the optical band gap by subgap absorption [121]. For MgO-rich compositions, the O vacancy V_O is the most stable intrinsic defect (cf. Fig. 1.16(a)), for which absorption at 5 eV energy (248 nm) has been reported [122]. However, the shoulder of the absorption edge observed for $Ni_{0.17}Mg_{0.83}O$

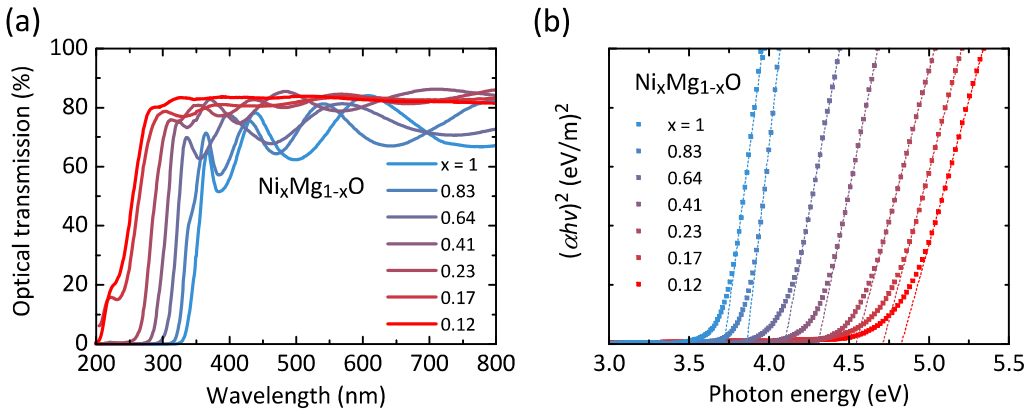


Fig. 3.7: (a) Optical transmission of $Ni_xMg_{1-x}O$ thin films (x = 1, 0.83, 0.64, 0.41, 0.23, 0.17, 0.12) in the UV-visible range from 200 nm to 800 nm. (b) Optical absorption showing the linear relationship between the photon energy $h\nu$ and $(\alpha h\nu)^2$, where α denotes the absorption coefficient, indicating a direct optical transition.

and $Ni_{0.12}Mg_{0.88}O$ at a wavelength of 220 nm cannot be unambiguously attributed to absorption by V_O defects, because the sensitivity of optical spectroscopy is too weak to detect subgap absorption by a small concentrations of defects and also the deuterium light source intensity considerably drops for the deep UV wavelength region.

The composition dependence of the $Ni_xMg_{1-x}O$ optical band gap as determined from the absorption spectra presented in this work is shown in Fig. 3.8. The optical band gaps which have been determined in previous studies of $Ni_xMg_{1-x}O$ thin films prepared by electron beam evaporation [87], molecular beam epitaxy [114], magnetron sputtering [90,115], pulsed laser deposition [123] and sol-gel spin coating [116] are included for comparison. In agreement with the previous studies, the present work confirms that the measured optical band gap of pure NiO is 3.7 eV and by alloying with MgO it increases linearly to 4.8 eV for $Ni_{0.12}Mg_{0.88}O$. Despite the small NiO fraction of only 12 at.%, it is striking to observe that the measured optical band gap remains 3 eV below that of pure MgO. It seems obvious that the $Ni_xMg_{1-x}O$ band gap bowing must be described by a linear function of composition, which is

in strong contrast to former studies attempting to apply the parabolic bowing equation (3.1) [86, 87, 90, 115, 117, 118].

Hybrid density functional calculations using the Heyd-Scuseria-Ernzerhof (HSE) approximation yields band gaps for $Ni_xMg_{1-x}O$ in agreement with experiment (for details see Ref. [124]). The slight overestimation (underestimation) of the calculated NiO (MgO) band gap from the experimental values is due to the difference in dielectric properties of NiO and MgO, as the empirical exchange mixing parameter used in the calculation should be adjusted with the dielectric tensor. However, optimization of the exchange mixing parameter would significantly increase the computational effort.

3.4 Discussion

By alloying with MgO, the NiO band gap increases about linearly from 3.7 eV to 4.8 eV in $Ni_{0.12}Mg_{0.88}O$. For MgO films doped with small concentrations below 12 at.% NiO a band gap discontinuity is expected. It is obvious that the standard bowing equation cannot be applied to describe the anomalous $Ni_xMg_{1-x}O$ band gap trend, because the bowing term $bx(1-x)$ only accounts for a parabolic deviation of the interpolated band gaps as a function of composition x, as a result of the variation in the crystal potential in the random alloy.

The very narrow $Ni_xMg_{1-x}O$ 200 diffraction spots obtained by HR-XRD shown in Fig. 3.2 do not show any peak broadening in the out of plane Q_z component in reciprocal space indicating that compositional fluctuations on a macroscopic level are insignificant. Compositional inhomogeneities are further very unlikely to be observed as it has been shown experimentally that NiO and MgO are fully miscible, typically forming a homogeneous $Ni_xMg_{1-x}O$ solid solution [72, 125]. A calorimetric investigation as well as thermodynamic modelling of the NiO-MgO system report a negative enthalpy of mixing describing a tendency towards atomic ordering

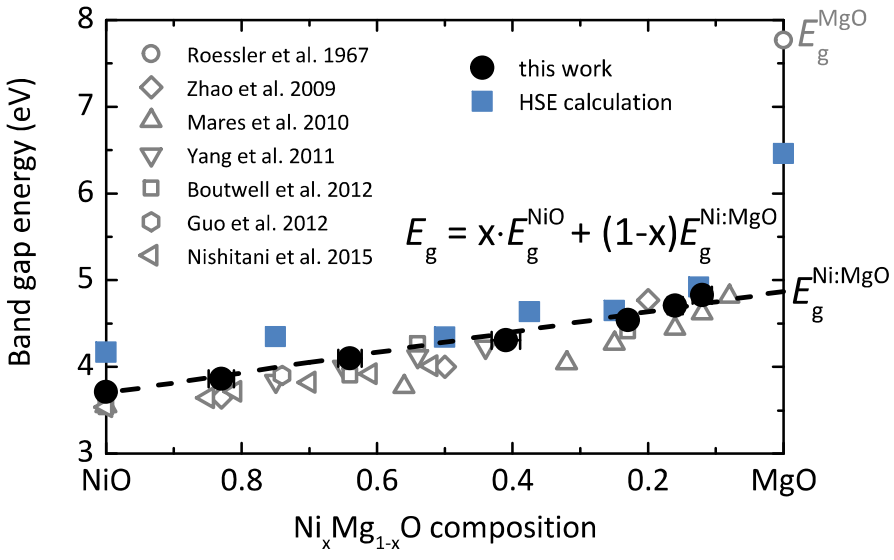


Fig. 3.8: Optical band gap of $Ni_xMg_{1-x}O$ thin films (x = 1, 0.83, 0.64, 0.41, 0.23, 0.17, 0.12) obtained by absorption spectra (black filled circles). The error in the determination of the optical band gap is contained within the size of the data points. Experimental optical band gaps which have been determined by absorption and reflectance spectra in previous studies are included for comparison (grey empty symbols, after Roessler [65], Zhao [87], Mares [114], Yang [115], Guo [123], Boutwell [116] and Nishitani [90]). Calculated electronic band gaps of $Ni_xMg_{1-x}O$ obtained from the density functional theory calculation using the HSE approach are given by blue filled squares (after Råsander in Ref. [124]).

rather than clustering [126, 127]. The microstructural homogeneity and high-quality epitaxial growth of the $Ni_xMg_{1-x}O$ is evident from the HR-TEM images showing a defect-free $Ni_xMg_{1-x}O$/MgO interface and suggesting single-domain epitaxial growth without evidence of either ordering or clustering (cf. Fig. 3.5).

The $Ni_xMg_{1-x}O$ band gap bowing cannot be attributed to any transition in crystal structure, direct-to-indirect electronic transition or variation in compositional homogeneity. However, calculations of the electronic properties of semiconductor alloy

systems have previously shown that the band gap bowing coefficient may nevertheless become largely composition dependent if the dilute alloy shows a localized deep impurity level in the band gap [128]. When there is a pronounced difference in properties between the alloy end members, the impurities in the dilute alloy may create new electronic states rather than altering the host energy levels [129].

Local spin density functional theory calculations of the $Ni_{0.125}Mg_{0.875}O$ density of states has shown that the octahedral coordination of Ni with O atoms leads to splitting of the degenerate d orbitals into occupied Ni 3d e_g and t_{2g} states which are separated by a small gap from unoccupied e_g states (Fig. 3.9(a)) [130]. The Ni 3d states are enclosed by O 2p and Mg 2s states forming the valence and conduction band in MgO. The calculations did not take into account the d-d Coulomb repulsion parameter of 4 eV, describing the additional energy required for creation of an electron-hole pair for charge transport via Ni 3d orbitals (cf. section 1.3.2). The occupied Ni 3d t_{2g} and e_g states are then shifted by -2 eV to merge with the O 2p states of the valence band and the unoccupied Ni 3d e_g are shifted by $+2$ eV. Despite the large MgO fraction, it follows that the resulting $Ni_{0.125}Mg_{0.875}O$ band structure is equivalent to that of NiO with a band gap characterized by a charge transfer from O 2p states in the valence band to unoccupied Ni 3d e_g states forming the conduction band (cf. Fig. 1.14(b)).

When the NiO concentration is diluted to the impurity limit in MgO, electronic structure calculations have shown that localized Ni 3d e_g and t_{2g} states are created inside the MgO band gap (Fig. 3.9(b)) [131]. Such localized states have been confirmed experimentally by absorption spectroscopy, cathodoluminescence and photoluminescence measurements of Ni-doped MgO crystals indicating electronic transitions attributed to the energy levels of Ni^{2+} impurities [132–134]. The anomalous $Ni_xMg_{1-x}O$ band gap narrowing is thus attributed to the fundamental difference in electronic structure between NiO and MgO, resulting in subgap absorption by Ni 3d e_g states

inside the MgO band gap.

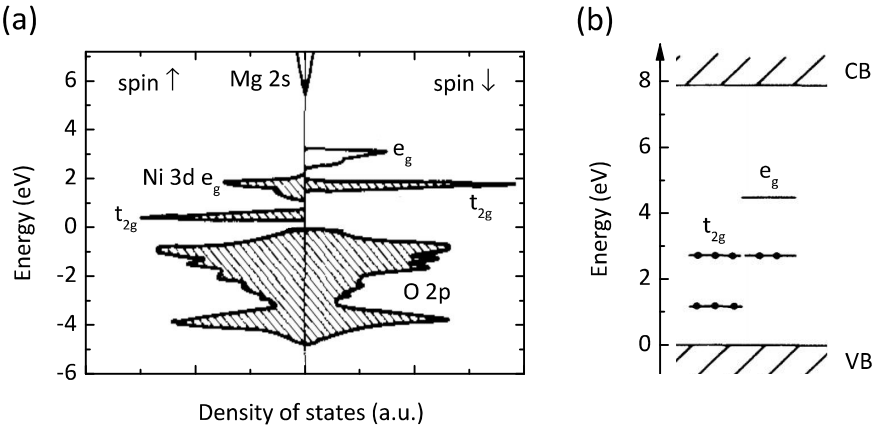


Fig. 3.9: (a) $Ni_{0.125}Mg_{0.875}O$ density of states obtained using the local spin density functional theory approach (after Kübler et al. [130]). (b) Localized Ni 3d states in impurity doped Ni:MgO inside the band gap obtained using the Fazzio-Caldas-Zunger [135] method (after Timmer et al. [131]).

The origin of the $Ni_xMg_{1-x}O$ band gap bowing is fundamentally different from that of most substitutional semiconductor alloys, for which the standard bowing equation holds. Instead, the non-parabolic $Ni_xMg_{1-x}O$ bowing behaviour induced by the Ni 3d-derived localized states can be related to the band gap narrowing observed for highly mismatched III-V semiconductor alloys such as GaN_xAs_{1-x} [136] and II-VI semiconductor alloys such as ZnS_xTe_{1-x} [137]. Alloying of GaAs (ZnTe) with a small amount of N (S) introduces localized states at an energy level close to the conduction band edge, resulting in splitting of the conduction band into subbands and an effective narrowing of the fundamental gap [138, 139]. However, the $Ni_xMg_{1-x}O$ solid solution system is different in that the localized Ni 3d e_g states remain as localized impurity states well inside the MgO band gap while no perturbation of the host conduction band structure is observed [124]. The $Ni_xMg_{1-x}O$ solid solution presents a unique system in which cation substitution of a small percentage of Ni^{2+} for Mg^{2+}

leads to a fundamental change in the electronic structure, while maintaining complete miscibility as well as structural stability over the entire composition range.

The $Ni_xMg_{1-x}O$ band gap trend is best described by a linear interpolation of the NiO band gap E_g^{NiO} (3.7 eV) and that of MgO doped with an infinitesimal Ni impurity concentration $E_g^{Ni:MgO}$ (4.9 eV):

$$E_g(x) = xE_g^{NiO} + (1-x)E_g^{Ni:MgO}. \tag{3.2}$$

The results suggest a critical Ni impurity concentration in $Ni_xMg_{1-x}O$ beyond which the defect-like impurity states become delocalised through the interaction of neighbouring Ni^{2+} cations distributed on the cation sublattice of the cubic rock-salt structure. For a random distribution of Ni^{2+} and Mg^{2+} cations on the face-centered cubic sublattice of $Ni_xMg_{1-x}O$, the calculated site percolation threshold of nearest-neighbour Ni^{2+} cations is 19.9 at.% NiO. [140]. The concentration threshold defines a "localized-to-delocalized" transition (cf. Ref. [129]) at which the $Ni_xMg_{1-x}O$ electronic structure changes from the characteristics of a concentrated $Ni_xMg_{1-x}O$ solid solution with a Ni 3d-derived conduction band to that of a dilute Ni:MgO solid solution with isolated Ni^{2+} impurity centres creating localized states in the MgO band gap. The concentration threshold indicates the length scale over which Ni^{2+}-Ni^{2+} interactions can appear assuming next-nearest neighbour interactions. The non-random ordering of Ni^{2+} atoms on the cation sublattice sites must be taken into account since it decreases the probability of Ni^{2+} nearest-neighbour site occupation.

3.5 Conclusion

Despite forming a completely miscible and compositionally homogeneous solid solution, alloys of NiO and MgO exhibit a strikingly anomalous band gap bowing behaviour. The non-parabolic $Ni_xMg_{1-x}O$ band gap dependence is attributed to the

fundamental difference in electronic structure between NiO and MgO. Localized Ni 3d impurity levels inside the MgO band gap account for a pronounced band gap narrowing as confirmed by optical absorption spectra. The standard bowing theory is inapplicable to describe the $Ni_xMg_{1-x}O$ band gap dependence and may in general not be applied to semiconductor systems, for which one of the alloy end members creates such deep levels in the band gap. Instead, the $Ni_xMg_{1-x}O$ band gap dependence on composition is simply described by a linear interpolation of the band gaps of NiO and Ni impurity doped MgO.

4 La:$BaSnO_3$ Solid Phase Epitaxy and Interstitial Hydrogen Doping

This chapter presents the solid phase epitaxial growth of high mobility La:$BaSnO_3$ thin films on $SrTiO_3$ single crystal substrates by crystallization through thermal annealing of nanocrystalline films prepared by pulsed laser deposition at room temperature. While vapour phase epitaxy of La:$BaSnO_3$ requires very high growth temperatures of $750 - 900$ °C under high vacuum, solid phase epitaxy is advantageous for film growth because the high temperature process may be separated from the vacuum deposition and easily performed in a conventional furnace. The La:$BaSnO_3$ thin films are investigated for their epitaxial quality, carrier transport properties and La doping activation efficiency.

The first experimental investigation of H doping to $BaSnO_3$ films is presented employing H plasma treatment at room temperature. Hall transport measurements show that after H doping, previously insulating $BaSnO_3$ films become highly conductive and in La:$BaSnO_3$ films the carrier concentration may be increased, supporting a theoretical prediction that interstitial H serves as an excellent n-type dopant. An analysis of the free electron absorption by IR spectroscopy yields a small (H,La):$BaSnO_3$ electron effective mass of 0.27 ± 0.05 m_0 which is comparable to the values obtained for other n-type conductive oxides like ZnO, SnO_2 and In_2O_3.

4.1 Introduction

The extraordinarily high carrier mobility of 320 cm^2/Vs recently reported for $BaSnO_3$ single crystals at a carrier concentration of 8×10^{19} cm^{-3} [19] has triggered a vast research effort to improve and understand the electronic transport in $BaSnO_3$ epitaxial thin films [22, 24, 25, 95, 96, 141, 142]. Besides its potential for commercial application as a transparent contact composed of abundant elements, La:$BaSnO_3$ epitaxial thin films may find applications as a high-mobility channel layer in multi-functional perovskite-based electronic devices and field effect transistors [143–145].

Pulsed laser deposition (PLD) and molecular beam epitaxy (MBE) are the preferred methods for preparation of high mobility $BaSnO_3$ thin films. Both vapour phase methods require elevated growth temperatures under high vacuum and stoichiometric $BaSnO_3$ growth with MBE is particularly difficult due to the difference in oxidation potentials of Ba and Sn, demanding replacement of a conventional metal Sn source by hexamethylditin $(CH_3)_6Sn_2$ or a pre-oxidized Sn source in form of SnO_x [25, 146]. In contrast, solid phase epitaxy presents an effective preparation method for single crystal-like thin films, as demonstrated for $In_2O_3(ZnO)_m$ (m = integer) [147] and La-CuOS [148, 149] epitaxial thin films. This chapter will present the successful adoption of solid phase epitaxy for preparation of high mobility La:$BaSnO_3$ thin films.

Room temperature Hall mobilities as high as 70 cm^2/Vs have been reported for vapour phase-grown epitaxial thin films at a doping level of 4×10^{20} cm^{-3} prepared by pulsed laser ablation of 4−7 at.% La:$BaSnO_3$ targets [19]. Despite La substitutional doping well beyond the 3 at.% equilibrium solubility limit in $BaSnO_3$ [40, 92, 150], the actual La composition in the thin films has rarely been questioned. So far only one report confirms the identical composition of 7 at.% La:$BaSnO_3$ target and pulsed laser-deposited thin film using proton induced X-ray emission [22]. In the latter study a La doping activation efficiency of 14 % is obtained, but other reports propose a 45-

69 % [96] and 30-45 % [23] La activation efficiency. This work will present an evaluation of the La doping efficiency from secondary ion mass spectroscopy concentration-depth profiles of 7 at.% La:$BaSnO_3$ thin films prepared by solid phase epitaxy.

$BaSnO_3$ offers great flexibility for substitutional doping by replacement of either Ba on the A-site or Sn on the B-site of the perovskite structure. However, substitutional doping with Sb for Sn [20,151] was found to be less effective in raising the free carrier concentration than doping with La for Ba, which is attributed to a more localized electron distribution around Sb impurities in $BaSn_{1-x}Sb_xO$ as compared to La substitutional doping in $La_xBa_{1-x}SnO_3$ [94] and the more shallow ionization level of the La_{Ba} defect as compared to Sb_{Sn} [43]. Moreover oxygen-deficient n-type conducting $BaSnO_{3-x}$ thin films with carrier concentrations of 5×10^{19} cm^{-3} can be obtained by vacuum annealing [93]. Further experimental studies of alternative n-type dopants for $BaSnO_3$ thin films have not been reported. However, first principles calculations predict the potential of interstitial hydrogen as a shallow donor in high electron affinity oxides, if the H^+/H^- charge transition lies well inside the conduction band [152,153]. In particular, calculations of the thermodynamic stability of interstitial H in $BaSnO_3$ indicate a low formation energy comparable to that of substitutional La on the Ba site, suggesting interstitial H as a promising alternative for n-type doping [43].

4.2 Experimental Methods

Polycrystalline $La_xBa_{1-x}SnO_3$ ($x = 0$, 0.03 and 0.07) targets for PLD were prepared from high purity $BaCO_3$, SnO_2 and La_2O_3 powders by solid state ceramic processing. The powders were mixed by ball-milling, pressed to pellets and calcined at 1200 °C for 12 h, then reground to powders, pressed and sintered at 1450 °C for 48 h. Rietveld refinement of the X-ray diffraction (XRD) pattern of the 7 at.% La:$BaSnO_3$ target showed that it is composed of two phases, 96.9 wt.% $La_xBa_{1-x}SnO_3$ (space group

Pm-3m, ICSD 100792) and 3.1 wt.% $La_2Sn_2O_7$ (spacegroup Fd-3m, ICSD 167144). $SrTiO_3$ (100) single crystal substrates were etched in NH_4F-buffered HF solution (pH 4.5) for 3 min and then ultrasonically cleaned in deionized water and ethanol. After annealing of the HF-etched $SrTiO_3$ substrates at 1050 °C for 1 h in air, a TiO_2-terminated step-and-terrace surface was obtained [154]. The $SrTiO_3$ substrates were inserted into a PLD system ($< 1 \times 10^{-5}$ Pa base pressure) and nanocrystalline (La:)$BaSnO_3$ thin films were deposited at room temperature and 7 Pa O_2 pressure using a 248 nm KrF laser with a fluence of 2 J/cm^2 at a pulse frequency of 10 Hz. The target-to-substrate distance was 5 cm and the thin film thickness was 100 nm.

The nanocrystalline structure of the La:$BaSnO_3$ thin films was investigated by X-ray diffraction (XRD) employing a Rigaku SmartLab diffractometer equipped with a monochromatic Cu $K_{\alpha 1}$ X-ray source (1.5406 Å) utilizing Bragg-Brentano optics. The thickness of the nanocrystalline thin films was obtained from X-ray reflectivity measurements utilizing parallel beam optics. The as-deposited La:$BaSnO_3$ thin film was then covered with the polished side of a yttria stabilized zirconia single crystal substrate and annealed at $800 - 1200$ °C for 1 h in air to induce the epitaxial crystallization. The annealing temperature was optimized to 1100 °C for preparation of highly conductive, epitaxial La:$BaSnO_3$ films of high crystalline quality. Parallel beam optics were used to acquire high resolution-XRD ω-2θ scans and a reciprocal space map of the La:$BaSnO_3$ 310 diffraction. The surface topography of the annealed $SrTiO_3$ substrates and the La:$BaSnO_3$ thin films before and after crystallization was investigated with a Bruker AXS MultiMode8 (for $SrTiO_3$ substrates) and a Seiko Instruments SPA-300 (for thin films) atomic force microscope (AFM).

Interstitial H doping of both $BaSnO_3$ and La:$BaSnO_3$ thin films at room temperature was implemented by H indiffusion during plasma treatment in 10 Pa H_2 atmosphere applying a radio frequency power of 50 W for 1 min. An IONTOF time-of-flight SIMS was used to analyse the H and La concentration profiles in the

La:$BaSnO_3$ and (H,La):$BaSnO_3$ thin films. The polycrystalline 7 at.% La:$BaSnO_3$ target was used as a standard to experimentally determine sensitivity factors for the recorded intensities of $LaOH^-$ anion clusters. 1 keV Cs^+ and 25 keV Bi^+ primary ion beams were used for sputtering and analysis in an area of 300 μm^2 and 100 μm^2, respectively.

The electron transparent cross-sectional TEM specimen was prepared by grinding, polishing and dimpling until the specimen thickness was below 10 µm, followed by Ar ion milling using a PIPS Ion miller (Gatan USA). Conventional and high resolution transmission electron microscopy (HR-TEM) was performed using a JEOL 2100 microscope equipped with a field emission gun operating at 200 keV.

Alternating current Hall measurements were performed with a ResiTest 8300 system (Toyo Co.) using the four-terminal method and van der Pauw geometry, employing electron beam-deposited Au/Ti contacts. Temperature-dependent electrical transport properties were measured in the range from 300 K to 80 K in He atmosphere. The desorption of H_2 and H_2O from (H,La):$BaSnO_3$ thin films was investigated with thermal desorption spectroscopy (TDS, ESCO 1400TV) during annealing up to temperatures of 700 °C in ultrahigh vacuum ($< 2 \times 10^{-7}$ Pa).

The optical transmission and reflectivity of the (H,La):$BaSnO_3$ thin films were measured with a Hitachi U-4100 UV-VIS-NIR and a Bruker Optics VERTEX70v FT-IR spectrophotometer. Profilometry and TEM images were used to determine the thin film thickness after epitaxial crystallization. A reduction to about 65 % of the original thickness was observed, which was taken into account for the evaluation of electronic and optical properties.

4.3 Results

4.3.1 La solubility in $BaSnO_3$

The XRD patterns of polycrystalline $La_xBa_{1-x}SnO_3$ ($x = 0$, 0.03 and 0.07) ceramic targets are shown in Fig. 4.1. While the $BaSnO_3$ and $La_{0.03}Ba_{0.97}SnO_3$ targets are comprised of a single perovskite phase, the 7 at.% La doped $BaSnO_3$ target shows an impurity pyrochlore phase of $La_2Sn_2O_7$ which is attributed to the limited La solubility in $BaSnO_3$. A maximum La solubility of 4 at.% in $BaSnO_3$ is determined from the weight fractions of phases obtained using Rietveld refinement and the overall 7 at.% La doping concentration of the target, which is in good agreement with previous analyses [40, 92, 150].

4.3.2 Structural Characterization

To facilitate the nucleation and solid phase epitaxial crystallization of La:$BaSnO_3$ thin films, $SrTiO_3$ (100) substrates with a TiO_2-terminated step-and-terrace surface structure were prepared (Fig. 4.2(a)). After etching of the $SrTiO_3$ (100) substrates in a NH_4F-buffered HF solution and annealing at 1050 °C, the surface profile shows steps of about 4 Å height corresponding to the $SrTiO_3$ unit cell size, and a terrace step width of about 110 nm (Fig. 4.2(b)). The AFM micrograph of a room temperature deposited 100-nm La:$BaSnO_3$ thin film shows a granular surface morphology indicating a nanocrystalline structure (Fig. 4.2(c)). Despite using a high intensity 9 kW X-ray source and Bragg-Brentano focussing optics, only diffraction peaks with weak intensities comparable to the background radiation are observed and it is concluded that the as-deposited La:$BaSnO_3$ thin films are of nanocrystalline nature (Fig. 4.2(d)).

After thermal annealing of the nanocrystalline 7 at.% La:$BaSnO_3$ thin films at 800 °C for 1 h in air, epitaxial growth through solid phase crystallization is initiated

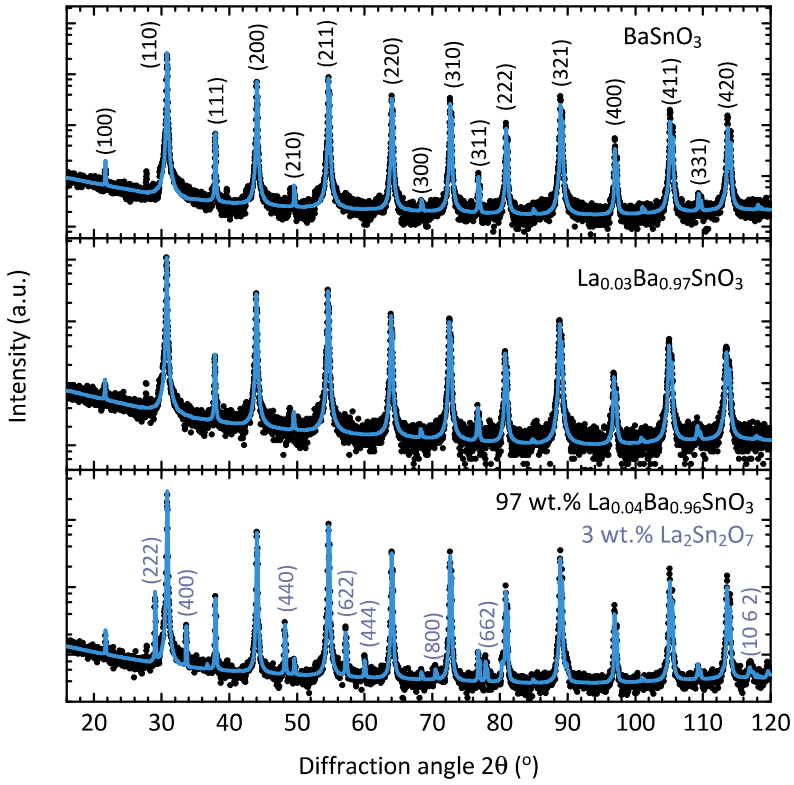


Fig. 4.1: XRD patterns of polycrystalline $La_xBa_{1-x}SnO_3$ (x = 0, 0.03 and 0.07) ceramic targets and simulated patterns using Rietveld refinement analysis (blue line).

as indicated by the roughened surface and HR-XRD pattern (Fig. 4.3(a,b)). The surface topography of La:$BaSnO_3$ films after solid phase epitaxy at 900 °C shows well-aligned, sharp cubic facets as consistent with the euhedral cubic La:$BaSnO_3$ crystals (Fig. 4.3(d)). However, the crystal mosaicity as indicated by the broad full width at half maximum of the 200 La:$BaSnO_3$ rocking curve is significantly high (Fig. 4.3(c,f)). The mosaicity of the solid phase epitaxially grown La:$BaSnO_3$ thin films is significantly reduced by annealing at a temperature of 1100 °C, resulting in a 0.07° full width at half maximum (FWHM) rocking curve (Fig. 4.3(i)).

The electrical resistivity and FWHM of the 200 rocking curves of 7 at.% La:$BaSnO_3$ thin films after annealed at temperatures of 950 to 1200 °C for 1 h in air shows

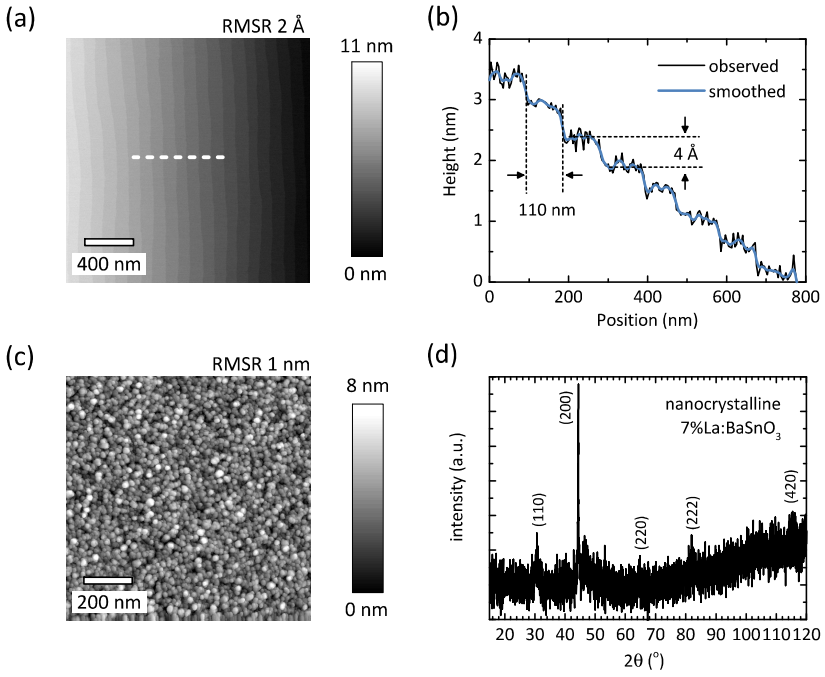


Fig. 4.2: (a) AFM micrograph of the step-and-terrace $SrTiO_3$ (100) surface after etching in NH_4F-buffered HF solution and annealing at 1050 °C for 1 h in air and (b) corresponding step profile. (c) Granular surface morphology of 100-nm nanocrystalline 7 at.% La:$BaSnO_3$ thin film deposited at room temperature and (d) corresponding XRD pattern recorded using Bragg-Brentano optics and an ω-offset to suppress $SrTiO_3$ substrate diffractions.

a minimum at about 1100 °C (Fig. 4.4). While a sufficiently high temperature is necessary for high quality epitaxial film growth from the amorphous phase, the crystal quality is again rapidly degrading at temperatures above 1200 °C. For all (La:)$BaSnO_3$ films characterized in the following, an annealing temperature of 1100 °C was used to induce the epitaxial crystallization.

The reciprocal space map analysis shows that the La:$BaSnO_3$ 310 diffraction spot is relatively narrow as compared to the $SrTiO_3$ substrate diffraction, demonstrating that epitaxial thin films of single crystal-like structure are obtained (Fig. 4.5). The in-plane and out-of-plane lattice parameters of 4.107 Å and 4.108 Å of the La:$BaSnO_3$ thin film are very close to the $La_{0.04}Ba_{0.96}SnO_3$ unstrained lattice parameter of 4.12 Å obtained by Rietveld refinement of the XRD pattern of the 7 at.% La:$BaSnO_3$ target. It is concluded that the thin films are almost completely relaxed due to the 5.5 % lattice mismatch with the $SrTiO_3$ substrate and the high-temperature crystallization process.

The microstructure of the (H,La):$BaSnO_3$ thin film is investigated by cross-sectional bright-field (BF) TEM acquired under two-beam conditions near the <100> zone axis (Fig. 4.6(a)). An array of equidistant misfit dislocations indicated by the dark contrast is observed at the interface between the (H,La):$BaSnO_3$ thin film and the $SrTiO_3$ substrate. The threading dislocations which proceed through the bulk of the film are indicated with thin arrows. The crystal quality of the La:$BaSnO_3$/$SrTiO_3$ interface is further investigated by cross-sectional HR-TEM images acquired along the <100> zone axis, for which the equidistant misfit dislocations are marked with bold arrows (Figs. 4.6(b) and (c)). Applying the measured in-plane La:$BaSnO_3$ and $SrTiO_3$ lattice parameters obtained in the 310 reciprocal space map analysis in Fig. 4.5(b), a theoretical misfit dislocation spacing of $a_{\mathrm{LBSO}}a_{\mathrm{STO}}/(a_{\mathrm{LBSO}} - a_{\mathrm{STO}}) =$ 7.9 nm is obtained, which is in excellent agreement with the experimentally observed 7.7 nm spacing and confirms that the thin film is relaxed with respect to the substrate. The selected-area electron diffraction pattern obtained for the La:$BaSnO_3$ thin film

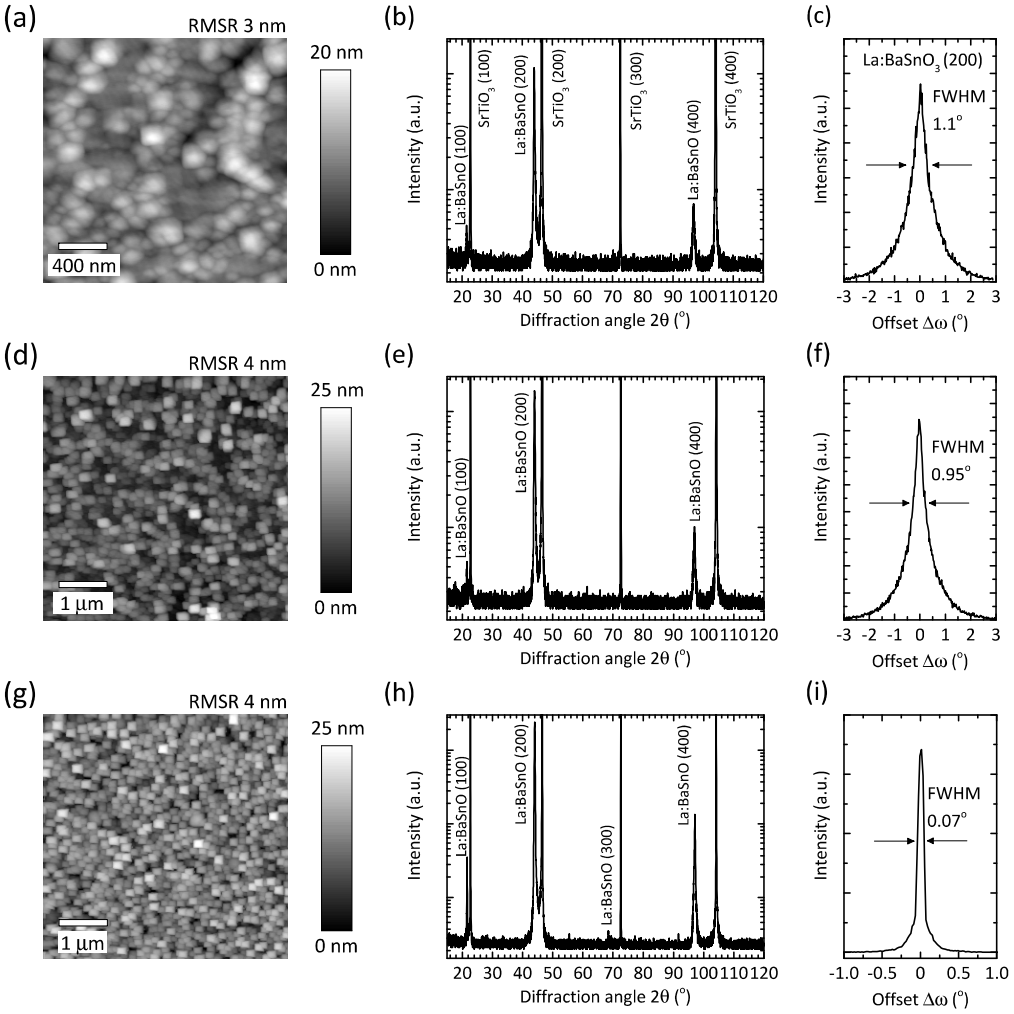


Fig. 4.3: 5×5 µm^2 AFM micrographs of La:$BaSnO_3$ thin films, corresponding HR-XRD patterns and 200 rocking curves using parallel beam optics after epitaxial crystallization at (a-c) 800 °C, (d-f) 900 °C and (g-i) 1100 °C for 1 h in air.

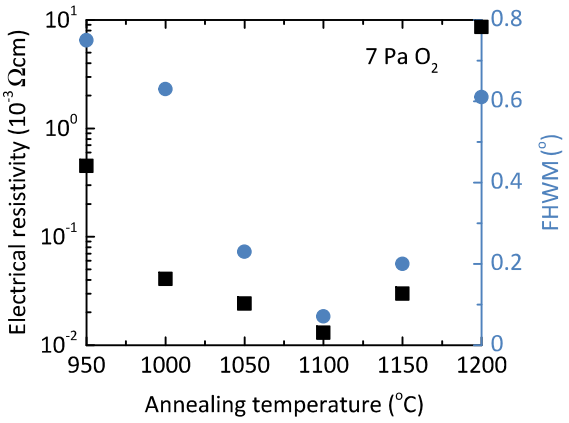


Fig. 4.4: Optimization of the annealing temperature of nanocrystalline La:$BaSnO_3$ according to crystal quality assessed by the electrical resistivity and FWHM 200 rocking curve analysis.

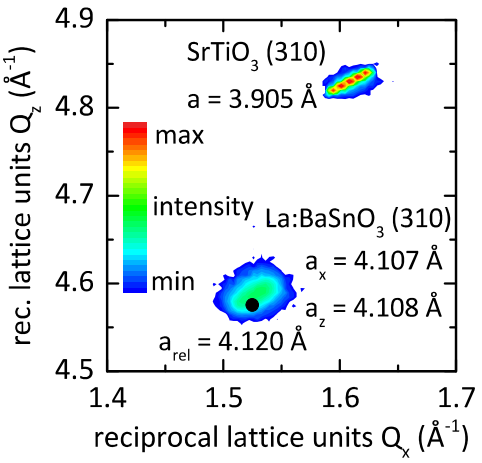


Fig. 4.5: Reciprocal space map of the 310 diffraction given by an equidistant iso-intensity contour map on a logarithmic scale. The epitaxial La:$BaSnO_3$ thin film is fully relaxed and the narrow diffraction peak relative to the $SrTiO_3$ single crystal substrate diffraction indicates the low degree of mosaicity.

confirms the La:$BaSnO_3$ (100) || $SrTiO_3$ (100) epitaxial relationship (Fig. 4.6(d)).

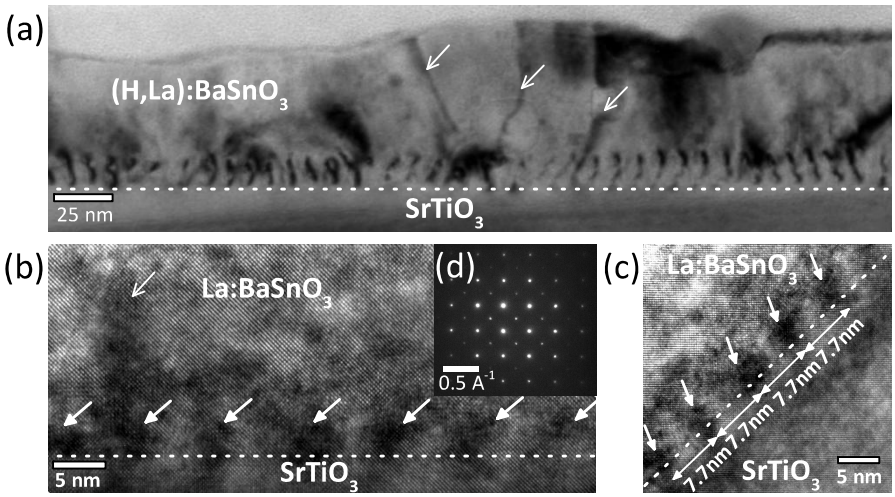


Fig. 4.6: (a) Microstructure of the (H,La):$BaSnO_3$ thin film investigated by BF cross-sectional TEM showing misfit dislocations along the (H,La):$BaSnO_3$/$SrTiO_3$ interface and threading dislocations (thin arrows) proceeding through the bulk of the film. (b),(c) Cross-sectional HR-TEM images showing the array of misfit dislocations (bold arrows) along the La:$BaSnO_3$/$SrTiO_3$ interface with an equidistant 7.7 nm spacing. (d) Corresponding selected area diffraction pattern of the La:$BaSnO_3$ thin film. Micrographs were taken by S. Rhode, Imperial College London.

The solid phase crystallization of nanocrystalline La:$BaSnO_3$ thin films on MgO substrates at a temperature of 1100 °C was also investigated. The surface topography shows a rough surface indicating formation of a polycrystalline film (Fig. 4.7(a)). The XRD pattern shows that La:$BaSnO_3$ epitaxy is observed with a large degree of mosaicity (Fig. 4.7(b,c)), but a secondary phase of spinel Mg_2SnO_4 develops which is attributed to interdiffusion of Sn from the nanocrystalline La:$BaSnO_3$ phase into MgO due to the high temperature process. It follows that the phase stability is a crucial factor in considering suitable substrates for the solid phase epitaxy process. All La:$BaSnO_3$ thin films characterized in the following sections were prepared by

solid phase epitaxy on $SrTiO_3$ substrates.

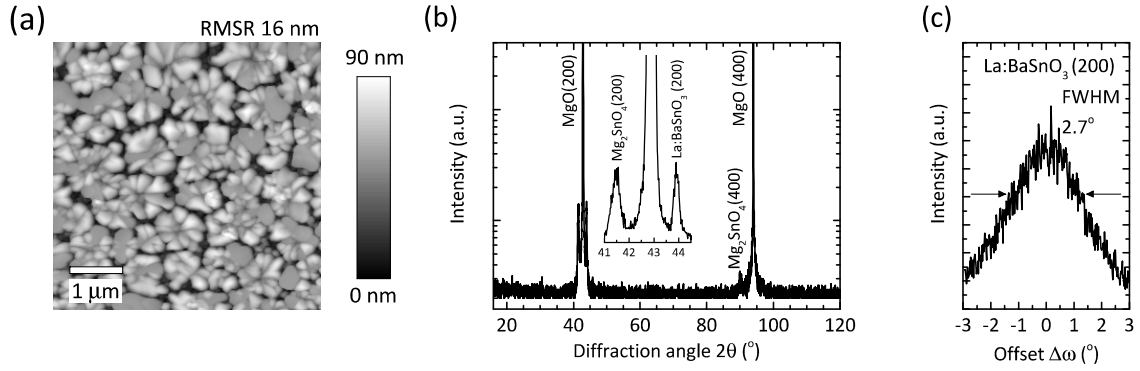


Fig. 4.7: (a) 5×5 µm^2 AFM micrographs of La:$BaSnO_3$ thin film on MgO substrate, (b) corresponding HR-XRD pattern indicating a secondary spinel Mg_2SnO_4 phase and (c) La:$BaSnO_3$ 200 rocking curve using parallel beam optics after solid phase crystallization at 1100 °C for 1 h in air.

4.3.3 Compositional Analysis

The recorded intensities of H^- anion, SnO_2^- and $LaOH^-$ anion clusters during SIMS depth-profiling of two 80-nm La:$BaSnO_3$ thin films after solid phase crystallization at 1100 °C, before and after H plasma treatment, are shown in Figs. 4.8(a) and (b), respectively. The $LaOH^-/SnO_2^-$ intensity ratio is constant over the entire depth profile indicating that La is uniformly distributed within the La:$BaSnO_3$ thin films. Employing experimentally derived sensitivity factors with a reference to the intensities obtained for the 7 at.% La:$BaSnO_3$ target, a La concentration of 7.4 ± 1.5 at.% in the crystallized La:$BaSnO_3$ thin films is determined. It follows that the La composition in the La:$BaSnO_3$ thin films is maintained during both room temperature PLD and solid phase crystallization at 1100 °C. The H^- concentration profiles include H desorption from the thin film surface, unintentional H incorporation during thin film deposition and the background intensity resulting from residual H within the analysis chamber.

The direct comparison of untreated and H plasma treated La:$BaSnO_3$ thin films shows a noticeably enhanced H concentration for the co-doped (H,La):$BaSnO_3$ thin film over the entire depth of the thin film.

4.3.4 Electrical Transport Properties

The electrical transport properties for a series of La:$BaSnO_3$ thin films prepared by solid phase epitaxial growth are summarized in Table 4.1. The electrical resistivity is as low as 3.3×10^{-3} Ωcm and Hall mobilities of 26 ± 1 cm^2/Vs are obtained at carrier concentrations of about 6×10^{19} cm^{-3}. Undoped $BaSnO_3$ thin films are insulating, but after H plasma treatment for 1 min they become highly conductive with Hall mobilities of 15 ± 1 cm^2/Vs, which is similar to that of the La:$BaSnO_3$ thin films but obtained at a doping level of only 3.3×10^{19} cm^{-3} Fig. 4.9. Co-doping of La:$BaSnO_3$ thin films by H indiffusion during the plasma treatment raises the doping level from about 8×10^{19} cm^{-3} to 1.6×10^{20} cm^{-3}, while the Hall mobility increases marginally. The temperature-dependent electrical transport properties of a La:$BaSnO_3$ thin film before and after H plasma treatment are shown in Fig. 4.9(b). The carrier concentration remains nearly constant with temperature indicating degenerate semiconductor (metal-like) behaviour.

TDS measurements show enhanced desorption of H_2 and H-related species such as H_2O for the H plasma treated $BaSnO_3$ and La:$BaSnO_3$ thin films in the temperature range from $100 - 370\,^{\circ}$C as compared to the H-undoped La:$BaSnO_3$ thin film (Fig. 4.10). Hall measurements after the high vacuum annealing process indicate that H doping is reversible, because the previously conducting H:$BaSnO_3$ thin film becomes insulating and the carrier concentration in the (H,La):$BaSnO_3$ thin film is reduced to the original La doping level (see Tab. 4.2).

Table 4.1: Electrical resistivity and Hall mobility for La-doped $BaSnO_3$ thin films as a function of carrier concentration before (left column) and after H doping (right column) presented in Fig. 4.9(a).

Material	Carrier concentration n (cm^{-3})		Resistivity ρ (10^{-3} Ωcm)		Hall mobility μ_H (cm^2/Vs)	
$BaSnO_3$	-	$2.9 \cdot 10^{19}$	-	23	-	9.2
$BaSnO_3$	-	$3.3 \cdot 10^{19}$	-	12	-	15
La:$BaSnO_3$	$5.6 \cdot 10^{19}$	$9.2 \cdot 10^{19}$	15	3.7	7.7	18
La:$BaSnO_3$	$5.6 \cdot 10^{19}$	$1.2 \cdot 10^{20}$	5.2	2.6	21	19
La:$BaSnO_3$	$5.7 \cdot 10^{19}$	$1.0 \cdot 10^{20}$	13	3.1	8.2	19
La:$BaSnO_3$	$6.0 \cdot 10^{19}$	-	4.0	-	26	-
La:$BaSnO_3$	$6.9 \cdot 10^{19}$	$1.6 \cdot 10^{20}$	3.3	1.9	26	22
La:$BaSnO_3$	$7.2 \cdot 10^{19}$	$1.2 \cdot 10^{20}$	3.6	2.0	24	27
La:$BaSnO_3$	$7.3 \cdot 10^{19}$	$1.3 \cdot 10^{20}$	11	2.7	7.7	17
La:$BaSnO_3$	$7.4 \cdot 10^{19}$	$1.1 \cdot 10^{20}$	6.6	2.4	13	23
La:$BaSnO_3$	$7.9 \cdot 10^{19}$	-	3.4	-	23	-
La:$BaSnO_3$	$8.3 \cdot 10^{19}$	$1.4 \cdot 10^{20}$	5.1	2.2	15	19

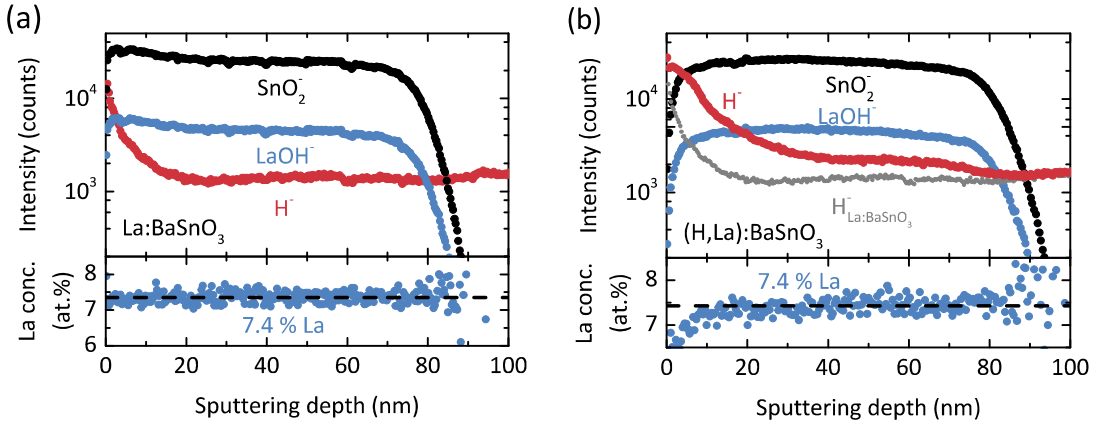


Fig. 4.8: SIMS depth profiles of (a) La:$BaSnO_3$ thin film after solid phase crystallization at 1100 °C and (b) co-doped (H,La):$BaSnO_3$ after subsequent H plasma treatment. The La doping concentration is evaluated by employing experimentally determined sensitivity factors. SIMS depth profiles were recorded by S. Fearn, Imperial College London.

Table 4.2: Comparison of the electrical resistivity ρ, carrier concentration n and Hall mobility μ_H of H:$BaSnO_3$ and (H,La):$BaSnO_3$ thin films before and after the thermal desorption of H_2 and H_2O.

specimen	after H plasma treatment			after H_2 and H_2O desorption		
	ρ (Ωcm)	n (cm^{-3})	μ_H (cm^2/Vs)	ρ (Ωcm)	n (cm^{-3})	μ_H (cm^2/Vs)
H:$BaSnO_3$	3.8×10^{-2}	1.3×10^{19}	13		insulating	
(H,La):$BaSnO_3$	2.0×10^{-3}	1.2×10^{20}	27	2.8×10^{-3}	8.1×10^{19}	28

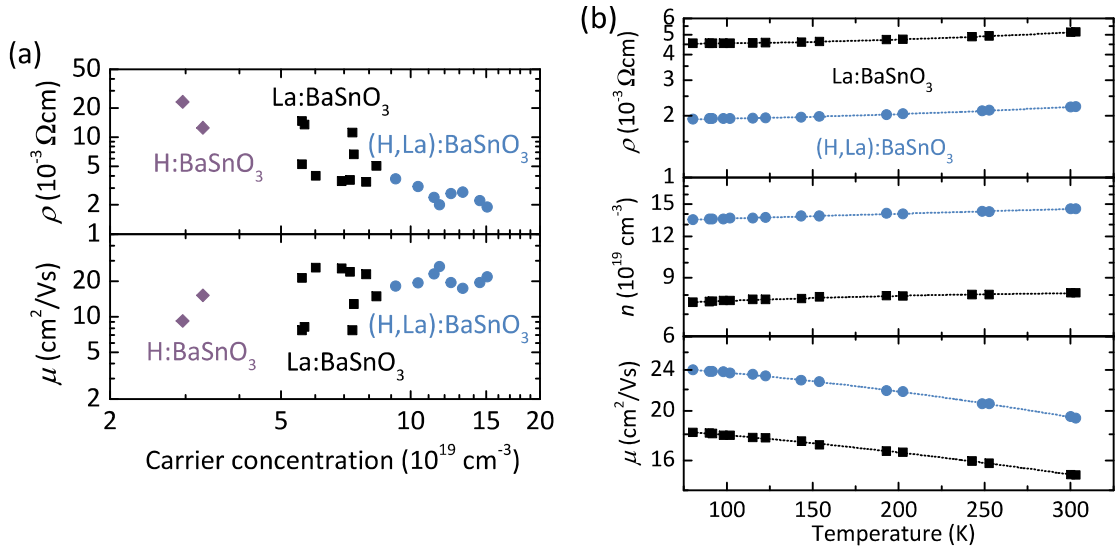


Fig. 4.9: (a) Electrical resistivity and Hall mobility for several H- and/or La-doped $BaSnO_3$ thin films as a function of carrier concentration. Co-doped (H,La):$BaSnO_3$ thin films show the highest carrier concentrations of about 1.6×10^{20} cm^{-3}. (b) The temperature-independent carrier concentration of both La:$BaSnO_3$ and co-doped (H,La):$BaSnO_3$ thin film indicates degenerate semiconductor (metal-like) behaviour.

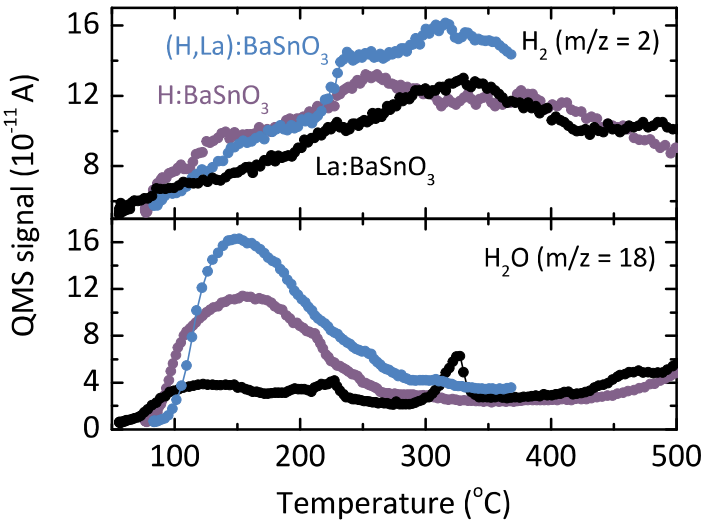


Fig. 4.10: TDS spectra of mass/charge ratio m/z = 2 (H_2) and m/z = 18 (H_2O) for H plasma treated H:$BaSnO_3$ and (H,La):$BaSnO_3$ thin films in comparison to a La:$BaSnO_3$ thin film without intentional H doping. Annealing of (H,La):$BaSnO_3$ was terminated at a temperature of 370 °C to demonstrate the change in electronic properties after H_2 and H_2O desorption (cf. Tab. 4.2). The amount of H_2O desorption between 100-370 °C was 5.4×10^{20} cm^{-3}, 5.8×10^{20} cm^{-3} and 2.0×10^{20} cm^{-3} for H:$BaSnO_3$, (H,La):$BaSnO_3$ and La:$BaSnO_3$, respectively. Measurements were conducted by K. Ide, Tokyo Institute of Technology.

4.3.5 Optical Characterization and Electrical Transport Properties

The optical transmission of a La:$BaSnO_3$ thin film before and after H plasma treatment is shown in Fig. 4.11. The co-doped (H,La):$BaSnO_3$ thin film shows enhanced free carrier absorption in the IR spectral region as compared to the La:$BaSnO_3$ thin film. The La-doped and co-doped (H,La):$BaSnO_3$ thin films are both about 85 % optically transparent in the visible region including the reflection loss.

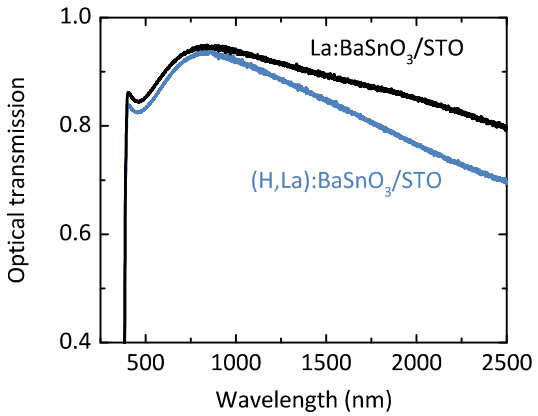


Fig. 4.11: Optical transparency of a La:$BaSnO_3$ thin films on $SrTiO_3$ substrate before and after H plasma treatment. The enhanced carrier density in the H-doped La:$BaSnO_3$ is indicated by the free carrier absorption in the IR spectral region.

The optical transmission and reflectivity of the (H,La):$BaSnO_3$ thin films was further investigated by FTIR spectra (Fig. 4.12(a)). A pronounced optical absorption in the region of $0.2 - 0.8$ eV is observed which is attributed to the free carrier absorption in the (H,La):$BaSnO_3$ thin film by comparison with the FTIR spectra of the bare $SrTiO_3$ single crystal substrate. The dielectric function $\varepsilon(\omega)$ of the (H,La):$BaSnO_3$ thin film at the IR spectral region is calculated by fitting theoretical transmission and reflectivity spectra to the measured ones at each data point (point-by-point analysis) with accounting for the dielectric function of the $SrTiO_3$ substrate. It is described by

the Drude free electron model in Eq. (2.14). The parameters used in the analytical model further allow for calculation of the DC resistivity $\rho = \frac{\gamma}{\varepsilon_0 \varepsilon_\infty \omega_p^2}$, optical mobility $\mu = \frac{\varepsilon_0 \varepsilon_\infty \omega_p^2}{ne\Gamma}$ and electron effective mass according to Eq. (2.15) of the (H,La):$BaSnO_3$ thin films.

The Drude free-electron model describes the dielectric function of the (H,La):$BaSnO_3$ thin film in the IR spectral region well (Fig. 4.12(b)). Since the optical mobility and the electron effective mass vary with the square of plasma frequency, the error in determination of these parameters for a single specimen is large. Thus an average optical mobility of 26 ± 7 cm^2/Vs and electron effective mass 0.27 ± 0.05 m$_0$ of (H,La):$BaSnO_3$ thin films is determined from a series of specimens.

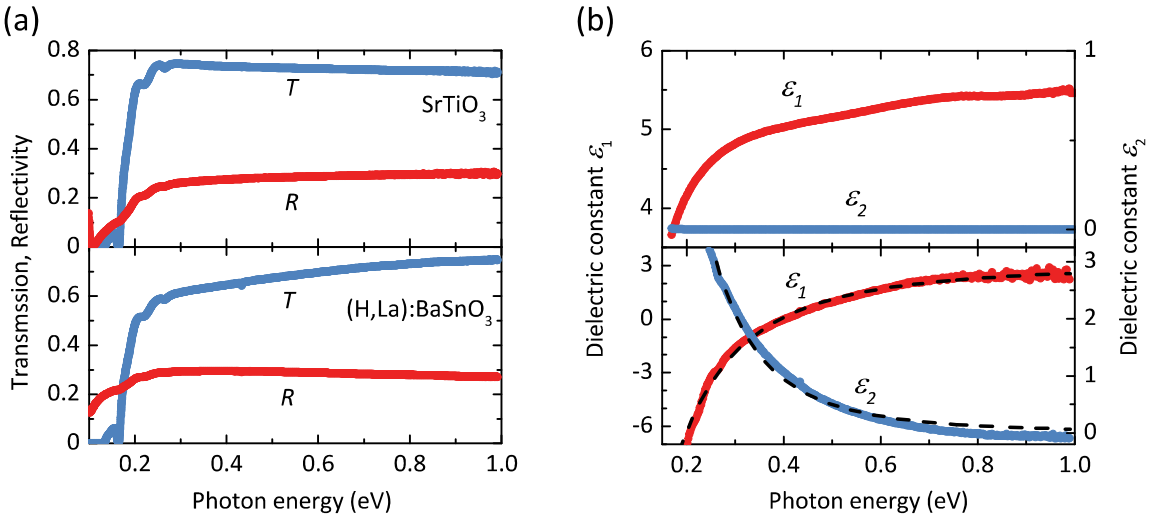


Fig. 4.12: (a) The IR optical transmission and reflectivity of the bare $SrTiO_3$ substrate and (H,La):$BaSnO_3$ thin film with (b) corresponding dielectric function obtained by a point-by-point analysis of the optical spectra. The dashed line indicates a fit of the Drude free electron model describing the free carrier absorption.

4.4 Discussion

4.4.1 La Doping Concentration and Donor Activation Efficiency

La:$BaSnO_3$ thin films of single crystal-like structure can be obtained employing the solid phase epitaxial growth method, but the high crystallization temperature of 1100 °C may result in purification of La:$BaSnO_3$ thin films with a reduced La concentration in analogy to the zone refining process of single crystals. The preparation of polycrystalline $La_xBa_{1-x}SnO_3$ powders and sintered ceramic targets showed that the equilibrium solid solubility limit of La in $BaSnO_3$ is only about 3 at.% [40, 92, 150], attributed to the smaller effective ion radius of La^{3+} (1.36 Å) as compared to Ba^{2+} (1.61 Å) [39]. The La solubility in $La_xBa_{1-x}SnO_3$ determined in this work is about 4 at.%, as obtained from the weight fractions of 96.9 % La:$BaSnO_3$ and 3.1 % $La_2Sn_2O_7$ after Rietveld refinement of the XRD pattern of the two-phasic 7 at.% La:$BaSnO_3$ target. Employing experimentally determined sensitivity factors for SIMS composition analysis, it is confirmed that the 7 at.% La doping concentration is maintained within the crystallized La:$BaSnO_3$ thin films after PLD and solid phase crystallization at 1100 °C temperature.

Epitaxial stabilization of the La:$BaSnO_3$ thin films may support La doping beyond the solubility limit without formation of a secondary phase. However, since the obtained La:$BaSnO_3$ thin film lattice parameters are similar to that of bulk La:$BaSnO_3$ with a La doping concentration of 4 at.%, excess La may have segregated at domain boundaries or likewise formed a secondary $La_2Sn_2O_7$ phase. These phases would not be identified by XRD analysis due to the random orientation and small crystallite size. Assuming that every La atom may contribute one free electron, the measured Hall carrier concentration of 9.0×10^{19} cm^{-3} for the La:$BaSnO_3$ thin film yields a La dopant activation efficiency of 9−16 %, depending on the actual La concentration in the La:$BaSnO_3$ grains of 4−7 at.%. The results are consistent with previous reports

of 7 at.% La:$BaSnO_3$ thin films deposited at 850 °C using pulsed laser deposition, for which a 14 % La doping activation efficiency was obtained [22].

The HR-TEM images indicate a high density of misfit dislocations at the La:$BaSnO_3$/$SrTiO_3$ interface resulting from the significant 5.4 % lattice mismatch between thin film and single crystal substrate. Because the dislocations may create deep electronic levels and trap carriers, a very high La doping concentration is required for screening of the defects before free carriers may be introduced that contribute to a high mobility [95, 142]. The trapping of carriers at dislocations is likely the reason why epitaxial La:$BaSnO_3$ thin films on $SrTiO_3$ single crystal substrates with doping levels below 2×10^{19} cm^{-3} have not been reported. For semiconductor thin films of high dislocation density the free carrier concentration may drop abruptly by several orders of magnitude below a certain carrier concentration threshold [155].

4.4.2 Interstitial Hydrogen Doping

The concept of interstitial H forming a shallow donor state in high electron affinity oxides was introduced by van de Walle et al. [152]. Since for most semiconductors the H^+/H^- charge transition level lies virtually constant at about 4.5 eV below the vacuum level, interstitial H may form a shallow donor if its level lies well inside the conduction band [49, 152, 153]. In analogy to ZnO and SnO_2, $BaSnO_3$ demonstrates a sufficiently high electron affinity to be doped by interstitial H (Fig. 4.13). Furthermore, first principles calculations of interstitial H in $BaSnO_3$ suggest a low formation energy, which is comparable to that of La substitution for Ba [43].

The large dispersion of the $BaSnO_3$ conduction band arising from the Sn 5s orbital as well as the ideal 180 ° Sn−O−Sn bond angle in the network of corner sharing $[SnO_6]^{2-}$ octahedra in the cubic perovskite structure are seen as the key factors for the high mobility [91]. The Hall measurements presented in this work show that

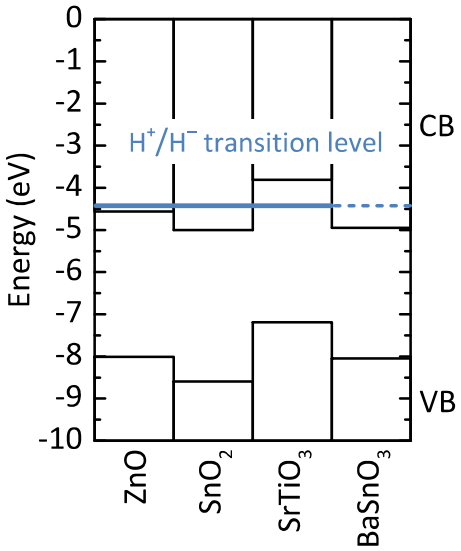


Fig. 4.13: Position of the universal H^+/H^- charge transition level in ZnO (after Van de Walle [49]), SnO_2, $SrTiO_3$ and $BaSnO_3$ with reference to the vacuum level (energy band alignments of ZnO/SnO_2, $SnO_2/SrTiO_3$ after Robertson [50] and $SrTiO_3/BaSnO_3$ after Bjaalie [52], respectively).

similar high mobilities are achieved by both, H- and La-doping (Fig. 4.9), as interstitial H does not perturb the electron conduction path through the $[SnO_6]^{2-}$ octahedra network. For example, Sb-doping on the Sn-site in $Sb:BaSnO_3$ is less beneficial as it results in inferior electronic transport and Hall mobilities as compared to $La:BaSnO_3$ [94, 142] and $H:BaSnO_3$. Thus interstitial H is suggested as the second most effective n-type dopant for $BaSnO_3$ after La reported up to date.

4.4.3 Electron Mobility, Electron Effective Mass and Carrier Scattering

According to equation (1.6), the electrical mobility μ in a semiconductor is determined by the ratio of the momentum relaxation time τ, denoting the average time

of momentum loss by scattering, and the electron effective mass m^*. As compared to other high mobility TCOs such as ZnO, In_2O_3 and SnO_2, the (H,La):$BaSnO_3$ electron effective mass of 0.27±0.05 m_0 is similarly small, indicating a large contribution to the high mobility (Tab. 4.3). Since the highest reported electron mobility of 320 cm^2/Vs has been reported for La:$BaSnO_3$ single crystals, the origin of the reduced mobility is proposed to result from the increased scattering rate (τ^{-1}) of electrons at defects in epitaxial (H,La):$BaSnO_3$ thin films.

Table 4.3: Comparison of the electron effective mass of high mobility TCOs ZnO_2, (H,La):$BaSnO_3$, SnO_2 and In_2O_3.

TCO	effect. mass (m_0)	Method	Ref.
ZnO	0.23	cyclotron resonance	[156]
(H,La):$BaSnO_3$	0.27 ± 0.05	FT-IR spectroscopy	this work
SnO_2	0.28	cyclotron resonance	[157]
In_2O_3	0.34	first-principles calculation	[158]

The optical mobility of 26 ± 7 cm^2/Vs obtained for (H,La):$BaSnO_3$ thin films from IR optical spectra is about equal to the electron mobility obtained by Hall measurements, indicating that scattering of electrons at grain boundaries is insignificant. The negative slope of the mobility-temperature relation indicating the non-thermally activated behaviour in Fig. 4.9(b) also supports this idea. This behaviour is typical for highly degenerated semiconductors, in which the trapped charges at the grain boundaries may be screened by the high density free electron gas, thereby reducing the effective barrier height for intergranular transport [159]. In comparison to La:$BaSnO_3$ single crystals, the dislocation density in La:$BaSnO_3$ thin films is generally larger by about an order of magnitude [142]. It is suggested that dislocations act as electron acceptors and the charged defects may significantly reduce

the optical mobility by long-range Coulombic interaction with carriers. Charged dislocation scattering is strongly screened due to the high carrier density and explains why for La:$BaSnO_3$ the Hall mobility generally increases with carrier concentration (cf. Fig. 4.9(b)). The nearly temperature-independent electrical mobility observed for (H,La):$BaSnO_3$ further shows striking similarity to the charged dislocation scattering mechanism reported for degenerately doped GaN [160] and InN [161] with high defect densities.

4.5 Conclusion

The La:$BaSnO_3$ solid phase epitaxy presents an effective method to obtain high mobility films of single crystal-like structure using the room temperature-deposited nanocrystalline phase as precursor. The relatively low La dopant activation of about $9 - 16$ % is attributed to dislocations in epitaxial La:$BaSnO_3$ thin films which act as carrier traps and possibly La segregation at grain boundaries due to the limited solubility in $BaSnO_3$ and high temperature crystallization process. Interstitial H doping as implemented by room temperature H plasma treatment is presented as the second most effective n-type doping possibility after substitutional La doping to enhance carrier concentrations. As compared to La:$BaSnO_3$ thin films, H:$BaSnO_3$ thin films show a similarly high mobility of 15 ± 1 cm^2/Vs, but at a doping level of only 3.3×10^{19} cm^{-3}.

The small electron effective mass of 0.27 ± 0.05 m_0 contributes to the high 29 ± 1 cm^2/Vs mobility observed for epitaxial co-doped (H,La):$BaSnO_3$ thin films, but the mobility is low as compared to 320 cm^2/Vs reported for La:$BaSnO_3$ single crystals. Both the TEM observation of the high misfit and threading dislocation density and the nearly temperature independent electron mobility suggest that charged dislocation scattering is the main cause for the reduced electron mobility in epitaxial

(H,La):$BaSnO_3$ thin films.

5 Electron Mobility Limits in Epitaxial $BaSnO_3$ Thin Films

In this chapter, the high room temperature mobility and the electron effective mass in $BaSnO_3$ are investigated in depth by evaluation of the free carrier absorption observed in infrared spectra for epitaxial films with free electron concentrations from 8.3×10^{18} to 7.6×10^{20} cm^{-3}. Both the optical band gap widening by conduction band filling and the carrier scattering mechanisms in the low and high doping regimes are consistently described employing parameters solely based on the intrinsic physical properties of $BaSnO_3$. The results explain the current mobility limits in epitaxial films and demonstrate the potential of $BaSnO_3$ to outperform established wide band gap semiconductors also in the moderate doping regime.

5.1 Introduction

Transparent perovskite stannate $BaSnO_3$ shows great potential as a high-mobility electron transport material composed of abundant elements. Since the report of an extraordinary high room temperature mobility of 320 cm^2/Vs for La:$BaSnO_3$ single crystals [19], which is the highest value reported for perovskite oxides, the material has rapidly attracted interest as high-mobility channel layers in oxide thin film transistors [143–145] and multi-functional perovskite-based optoelectronic devices [32,33]. To fully exploit the potential of La:$BaSnO_3$ for device applications, current research concentrates on understanding and improving the electron transport in epitaxial La:$BaSnO_3$ thin films [22, 24–26, 95, 96, 141, 142].

La:$BaSnO_3$ thin films grown heteroepitaxially on $SrTiO_3$ substrates using pulsed laser deposition (PLD) show a reduced carrier mobility of 70 cm^2/Vs [96] as compared to single crystals. It was suggested that the high density of dislocations introduced scattering centres for electron transport [95]. However, even by homoepitaxy on $BaSnO_3$ single crystals the carrier mobility can be increased only to 100 cm^2/Vs [24]. Moreover, molecular beam epitaxy allows for preparation of La:$BaSnO_3$ films with the record Hall mobility of 124 cm^2/Vs on $SrTiO_3$ substrates [25], suggesting the larger impact of the deposition method on electron transport properties. A quantitative analysis of the prevailing carrier scattering mechanism in $BaSnO_3$ epitaxial films is still lacking and would provide a guideline for improving the electron transport beyond the current mobility limits of epitaxial films.

The high mobility in La:$BaSnO_3$ single crystals is attributed to the large dispersion of the Sn 5s orbital-derived conduction band and the ideal 180° O−Sn−O bond angle in the network of corner sharing $(SnO_6)^{2-}$ octahedra in the cubic perovskite structure [91]. Quantitatively, the electron mobility is determined by the ratio of electron effective mass m_e^* and scattering relaxation time τ as given in Eq. (1.6). A

fundamental understanding of the electron transport in epitaxial La:$BaSnO_3$ films thus requires a quantitative analysis of these two quantities, which both strongly dependent on carrier concentration.

5.2 Experimental Methods

Polycrystalline $La_xBa_{1-x}SnO_3$ (x = 0, 0.01, 0.03 and 0.07) ceramic targets for pulsed laser deposition (PLD) were prepared by calcination of stoichiometric mixtures of high purity La_2O_3, $BaCO_3$ and SnO_2 powders at 1200 °C for 12 h, reground and sintered at 1450 °C for 48 h. A polycrystalline NiO target was prepared by sintering high purity NiO powder at 1200 °C for 5 h.

200-nm La:$BaSnO_3$ thin films were deposited on a 50-nm NiO buffer layer on MgO(100) single crystal substrates by pulsed laser ablation of the targets using a KrF excimer laser (248 nm) at a pulse frequency of 8 Hz. The NiO buffer layer was deposited at a substrate temperature of 700 °C, O_2 pressure of 0.7 Pa and laser beam fluence of 2.3 J/cm^2. The La:$BaSnO_3$ thin film was deposited at a substrate temperature of 800 °C, O_2 pressure of 20 Pa and laser beam fluence of 1.8 J/cm^2. The La doping concentration in the $BaSnO_3$ films was varied from $0-7$ at.% in the Ba site by co-ablation of two $La_xBa_{1-x}SnO_3$ ceramic targets of different compositions x using a multi-target carousel.

The crystal structures of the films were investigated by high resolution X-ray diffraction (HR-XRD) employing a Philips MRD diffractometer with a monochromatic Cu $K_{\alpha 1}$ (1.5406 Å) X-ray source and parallel beam optics. The surface topography of the MgO substrate, NiO and La:$BaSnO_3$ thin films was investigated with a Bruker atomic force microscope (AFM) in contact mode. The cross-sectional transmission

electron microscopy (TEM) specimen was prepared by grinding, polishing and dimpling until the specimen thickness was below 10 μm, followed by Ar ion milling using a PIPS Ion miller (Gatan USA). Conventional and high resolution TEM was performed using a JEOL 2100 microscope equipped with a field emission gun operating at 200 keV.

Optical transmission and reflectivity spectra of La:$BaSnO_3$ films were measured by vacuum Fourier transform infrared (FTIR) spectroscopy for photon energies of $0.1 - 1$ eV. Ellipsometry spectra of La:$BaSnO_3$ films were recorded using a Jobin Yvon UVISEL spectrophotometer equipped with a phase modulator, at 60° angle of incidence and in the spectral range from $0.6 - 4.8$ eV.

Alternating current Hall measurements of La:$BaSnO_3$ films at room temperature were performed with a LakeShore 8400 system (Toyo Co.) using the four-terminal method with sputtered Au/Ti contacts in van der Pauw geometry. The Hall carrier concentration was accurately determined using the film thickness derived from spectroscopic ellipsometry analysis. Temperature-dependent electrical transport properties were measured with a ResiTest 8300 system (Toyo Co.) in the range from 300 to 45 K in He atmosphere.

5.3 Results

5.3.1 La:$BaSnO_3$ Epitaxy on MgO Substrate

Regardless of the small 2.3 % lattice mismatch between MgO (4.212 Å) and $BaSnO_3$ (4.117 Å), a NiO buffer layer (4.177 Å) is necessary to facilitate the epitaxial growth. The out-of-plane HR-XRD patterns of 7 at.% La:$BaSnO_3$ thin films on MgO(100) substrate demonstrate that the crystal quality strongly depends on the thickness of the NiO buffer layer (Fig. 5.1). The 7 at.% La:$BaSnO_3$ thin film depos-

ited directly on the MgO substrate without use of any buffer layer is nanocrystalline-polycrystalline as indicated by the diffraction peaks from different crystallographic planes, the weak peak intensities and missing diffraction peaks as compared to the XRD pattern of the polycrystalline material (cf. Fig. 4.1). By employing a 30-nm thick NiO buffer layer, (100) epitaxy is observed, however, a significant fraction of the 7 at.% La:$BaSnO_3$ film still shows a random orientation. When the NiO buffer layer thickness is increased to 60 nm, high quality (100) epitaxy of 7 at.% La:$BaSnO_3$ on NiO/MgO is realized.

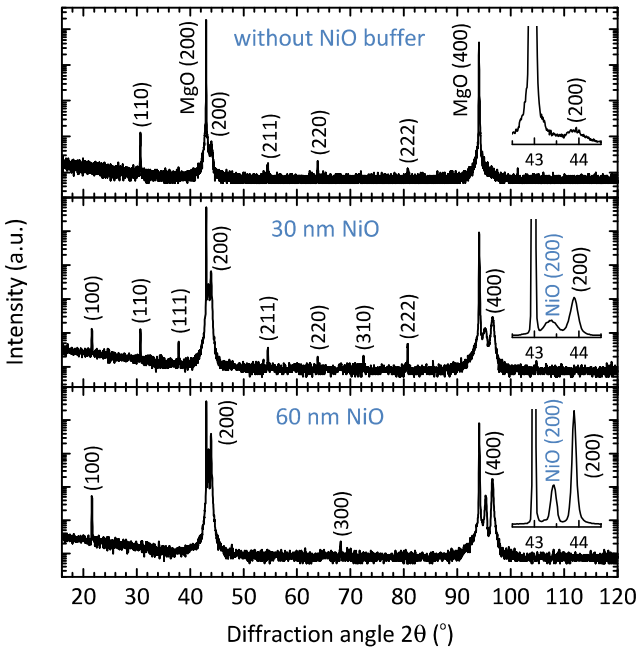


Fig. 5.1: Out-of-plane HR-XRD patterns recorded with parallel beam geometry of 7 at.% La:$BaSnO_3$ thin films on MgO substrate without buffer layer, 30-nm and 60-nm NiO-buffered MgO substrate. Insets show a magnification of the 200 diffraction peaks on a linear scale.

Apart from the structural difference of $BaSnO_3$ and MgO, the quality of the substrate surface is another crucial factor to consider for achieving high quality epitaxy. The surface roughness of an as-received, chemically-mechanically polished MgO sub-

strate annealed at a temperature of 800 °C is greater than that of a 50-nm NiO thin film deposited on MgO substrate with the same annealing treatment (Fig. 5.2). In general, MgO substrates are prone to form a carbonate layer and it is more difficult to clean the surface by annealing. This is in contrast to the high crystal quality perovskite substrates such as $SrTiO_3$, for which a clear step-and-terrace surface structure may be readily obtained (cf. Fig. 4.2(a)). While the MgO substrate shows no such surface features, the NiO film topography shows facets which may promote nucleation of $BaSnO_3$ at the initial growth stage.

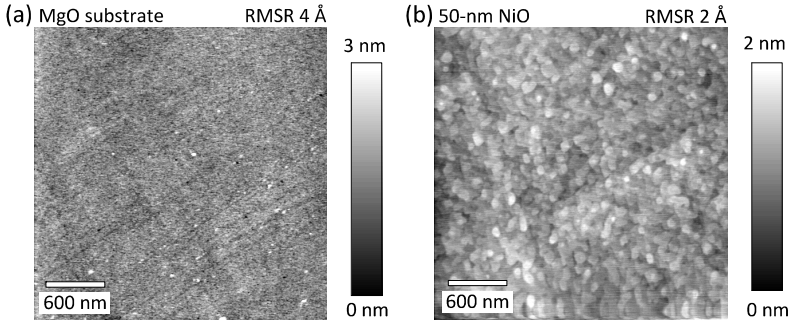


Fig. 5.2: Surface topography of (a) MgO substrate and (b) 50-nm NiO buffer layer on MgO substrate both annealed at 800 °C.

The surface topography of 7 at.% La:$BaSnO_3$ thin films on MgO(100) substrate changes remarkably based on the thickness of the NiO buffer layer. When no buffer layer is employed or the NiO film thickness is only 30 nm, a nanocrystalline thin film morphology with large surface roughness is observed (Fig. 5.3(a,b)). 7 at.% La:$BaSnO_3$ thin films deposited on MgO substrates employing a NiO-buffer layer of 60 nm show an atomically smooth surface indicating a high quality crystal growth (Fig. 5.3(c)).

The high resistivity of the 7 at.% La:$BaSnO_3$ film on MgO substrates without NiO buffer layer reflects the nanocrystalline nature of the film, in agreement with XRD and AFM analysis (Tab. 5.1). In contrast, the electrical transport properties of the

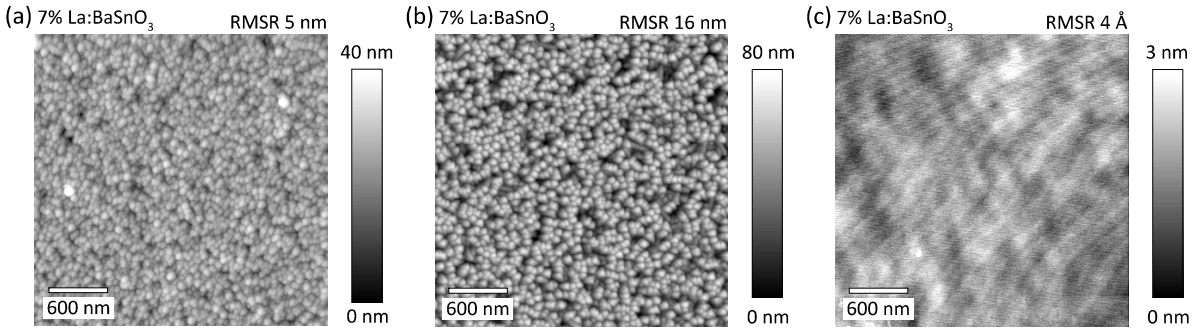


Fig. 5.3: Surface topography of 7 at.%La:$BaSnO_3$ (a) nanocrystalline film on MgO substrate (b) nanocrystalline/semi-epitaxial film on 30-nm NiO-buffered MgO substrate and (c) epitaxial film on 60-nm NiO-buffered MgO substrate.

7 at.% La:$BaSnO_3$ film grown on NiO-buffered MgO substrate are greatly improved. It is remarkable that the nanocrystalline/semi-epitaxial 7 at.% La:$BaSnO_3$ film grown on 30-nm NiO-buffered MgO substrate shows a surprisingly high carrier concentration and Hall mobility as compared to the epitaxial film grown on 60-nm NiO-buffered MgO substrate, indicating that the remaining fraction of the nanocrystalline phase does not deteriorate the transport properties to a large degree.

Table 5.1: Electron transport properties of 7 at.% La:$BaSnO_3$ thin film on MgO substrate, and employing a 30 nm and 60 nm NiO buffer layer on MgO substrate.

Material	NiO thickness (nm)	Resistivity (Ωcm)	Carrier concentration (cm^{-3})	Hall mobility (cm^2/Vs)
7 at.% La:$BaSnO_3$	0	1.7	-	-
7 at.% La:$BaSnO_3$	30	1.9×10^{-3}	2.4×10^{20}	14
7 at.% La:$BaSnO_3$	60	1.6×10^{-4}	7.3×10^{20}	47

5.3.2 Structural Characterization of La:$BaSnO_3$/NiO Epitaxial Films

All La:$BaSnO_3$/NiO heterostructures characterized in the following sections refer to a NiO buffer layer thickness of 50 nm, which is sufficient to obtain single-phase epitaxy along the [100] crystallographic direction for both layers, as demonstrated by the out-of-plane diffraction pattern of the La:$BaSnO_3$/50-nm NiO heterostructure (Fig. 5.4(a)). The 0.57° full width at half maximum (FWHM) of the out-of-plane 200 La:$BaSnO_3$ diffraction peak obtained after deconvolution from the corresponding NiO diffraction peak indicates a moderate degree of mosaicity (Fig. 5.4(b)).

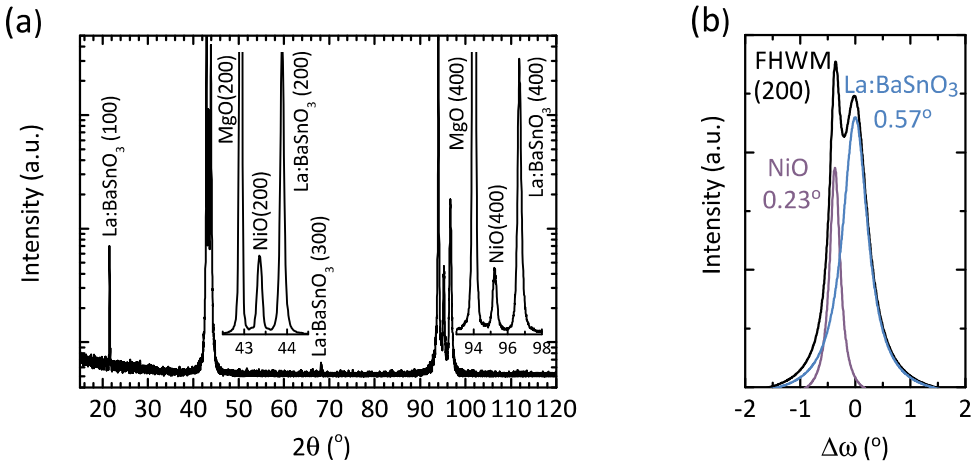


Fig. 5.4: (a) Out-of-plane HR-XRD pattern of La:$BaSnO_3$ thin film on 50-nm NiO-buffered MgO substrate in a logarithmic plot, indicating the single-phase and 100 oriented epitaxial growth. Insets show magnified views of the 200 and 400 diffraction peaks on a linear scale. (b) The 0.57° FWHM rocking curve of the La:$BaSnO_3$ 200 diffraction demonstrates epitaxial growth with a moderate degree of mosaicity.

The 204 reciprocal space map high resolution X-ray diffraction (HR-XRD) analysis confirms the 100 epitaxy of La:$BaSnO_3$ thin film on NiO-buffered MgO substrate (Fig. 5.5). The NiO buffer layer is slightly strained in plane while the

La:$BaSnO_3$ thin film is completely relaxed and shows a moderate degree of mosaicity as indicated by the broadened diffraction peak relative to that of the MgO single crystal in the 204 reciprocal space map.

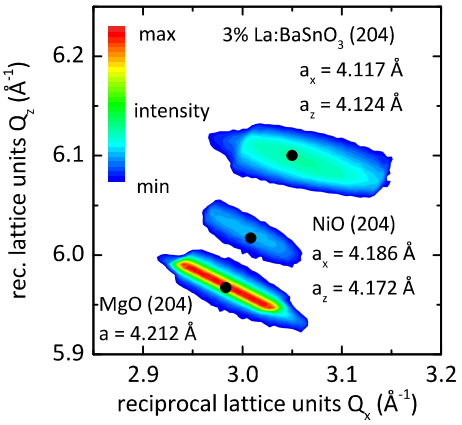


Fig. 5.5: HR-XRD 204 reciprocal space map of 300-nm La:$BaSnO_3$ on 50-nm NiO-buffered MgO substrate given by an intensity contour map on a logarithmic scale with reference positions of unstrained crystals indicated with black dots.

The cross-sectional bright-field transmission electron microscopy (TEM) image of the La:$BaSnO_3$ thin film on a NiO-buffered MgO substrate indicates columnar growth as deduced from the observation of grain boundaries marked by the arrows in Fig. 5.6(a). The cross-sectional high resolution micrograph shows the La:$BaSnO_3$/NiO interface is free of misfit dislocations (Fig. 5.6(b)) as confirmed by the average background subtraction filtered (ABSF) HR-TEM micrograph (Fig. 5.6(c)). Consistent with the mosaicity derived from HR-XRD analysis, the La:$BaSnO_3$ microstructure shows grains of ca. 30 nm size which are slightly tilted with respect to the [100] epitaxial orientation and forms low-angle grain boundaries (Fig. 5.6(d)).

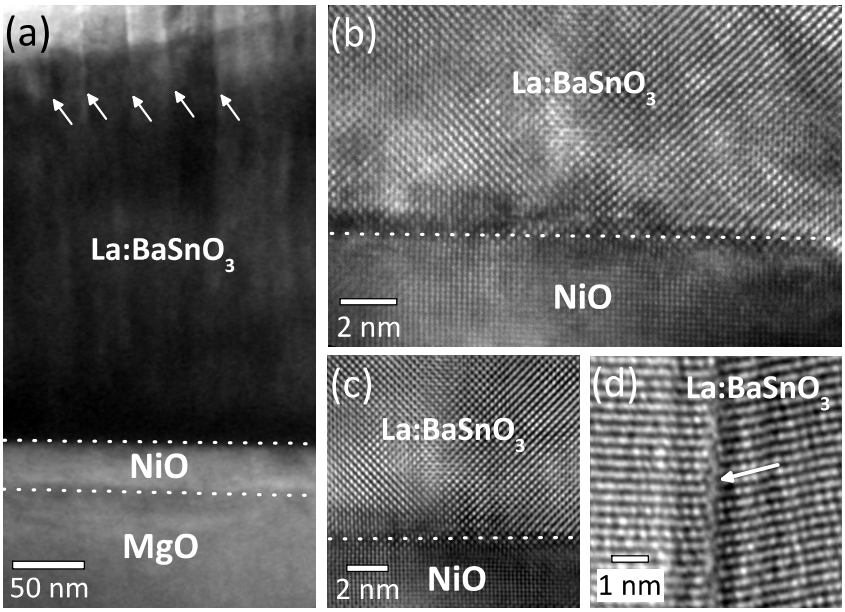


Fig. 5.6: (a) Cross-sectional bright-field TEM micrograph indicates the presence of vertical grain boundaries in La:$BaSnO_3$ and columnar growth. (b) Cross-sectional HR-TEM micrograph shows the single-domain epitaxy at the La:$BaSnO_3$/NiO interface which is free of misfit dislocations as confirmed by the (c) ABSF-filtered HR-TEM micrograph. (d) HR-TEM micrograph of a low-angle grain boundary between two La:$BaSnO_3$ crystallites. TEM micrographs were recorded by S. Rhode, Imperial College London.

5.3.3 Electron Effective Mass

The optical transmittance and reflectivity of the La:$BaSnO_3$ thin films were recorded with FTIR spectroscopy for photon energies of $0.1 - 1$ eV. By comparison with the transmittance spectrum of a 50-nm NiO film on a MgO substrate, the free carrier absorption in La:$BaSnO_3$ below 0.4 eV energy is observed even for a small carrier concentration of 1.6×10^{19} cm^{-3} (Fig. 5.7(a)). When the doping level is increased to 4.4×10^{20} cm^{-3}, the La:$BaSnO_3$ film shows a significantly enhanced IR absorption and reflectivity. The optical constants are obtained from the transmittance and reflectivity spectra as described in section 2.6. The MgO and NiO IR dielectric function is determined by a point-by-point calculation according to equations Eq. (2.12) and (2.13) and is shown in Fig. 5.7(b).

The reflection ellipsometry spectra were recorded in the spectral range from $0.6 - 4.8$ eV (Fig. 5.8(a)). The Tauc-Lorentz dispersion function is employed to describe the dielectric function of the NiO buffer layer [162], which is well suited to describe the optical properties of insulators and semiconductors. The dispersion model parameterizes the imaginary part ε_2 of the dielectric function, which determines the optical absorption of the material. The real part ε_1 is then obtained by Kramers−Kronig integration of the imaginary part ε_2. For photon energies E below the interband transition E_g, the optical absorption by the material is zero. For photon energies above the band edge, according to Tauc et al. the imaginary part of the dielectric function is [163]

$$\varepsilon_2^{\mathrm{T}}(E) = A_{\mathrm{T}} \frac{(E - E_g)^2}{E^2} \tag{5.1}$$

where A_T is a fitting parameter in units of energy. In the Tauc-Lorentz dispersion model, the Tauc term is multiplied by the Lorentz calculation of the imaginary part [164]

$$\varepsilon_2^{\mathrm{L}}(E) = \frac{A_{\mathrm{L}} E_0 C E}{(E^2 - E_0^2)^2 + C^2 E^2} \tag{5.2}$$

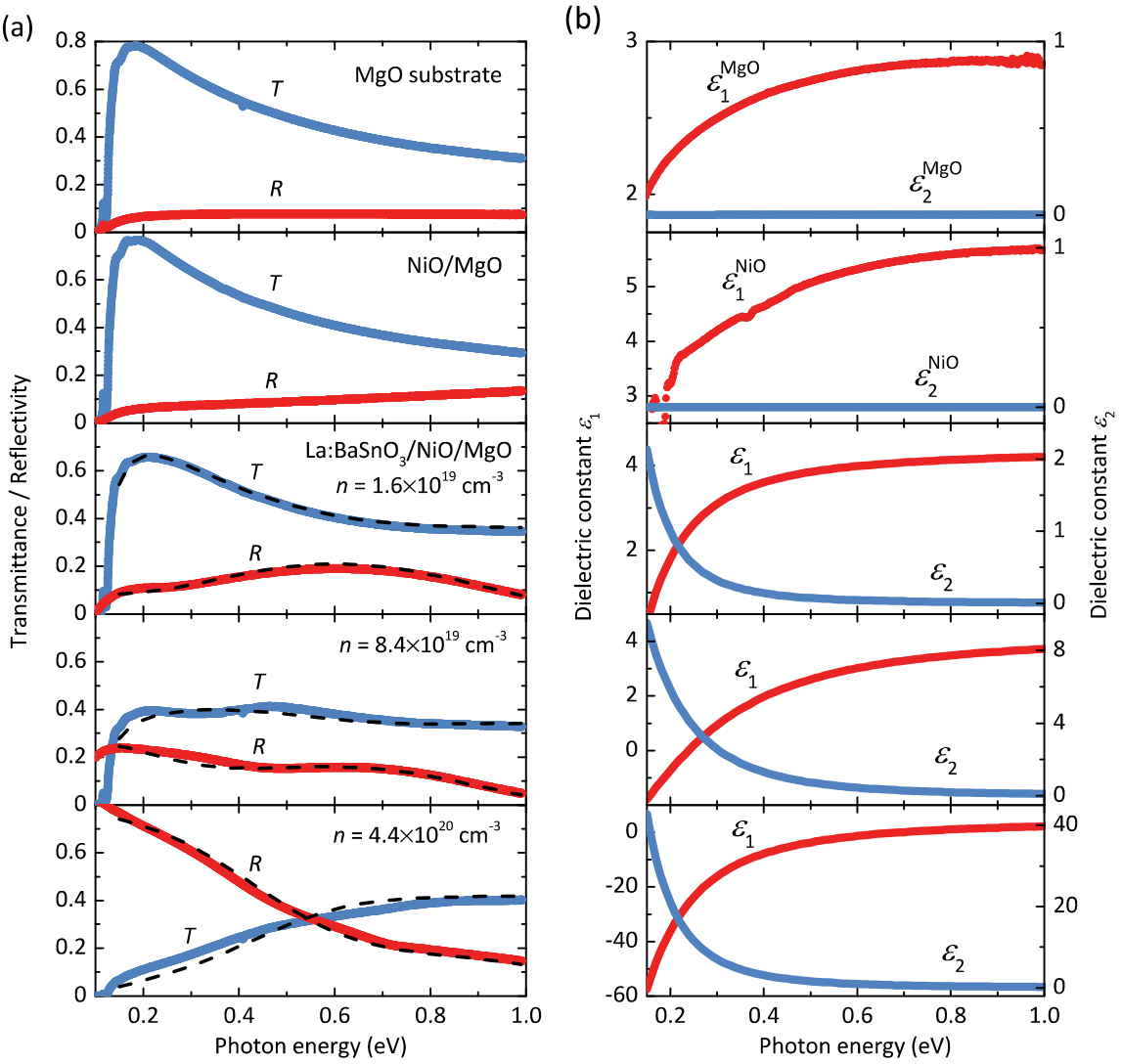


Fig. 5.7: (a) Optical IR transmittance (blue) and reflectivity (red) spectra of bare MgO substrate, NiO film and La:$BaSnO_3$/NiO bilayer structure on MgO substrate. Carrier concentrations in La:$BaSnO_3$ were 1.6×10^{19} cm^{-3}, 8.4×10^{19} cm^{-3} and 4.4×10^{20} cm^{-3} as determined by Hall effect measurements. Dashed lines to the La:$BaSnO_3$ IR spectra indicate theoretical fitting curves employing a combined model of the Drude free carrier absorption and the Tauc-Lorentz dispersion function. (b) Corresponding dielectric functions obtained by the point-by-point analysis of the IR spectra (MgO, NiO) and the dispersion model analysis (La:$BaSnO_3$).

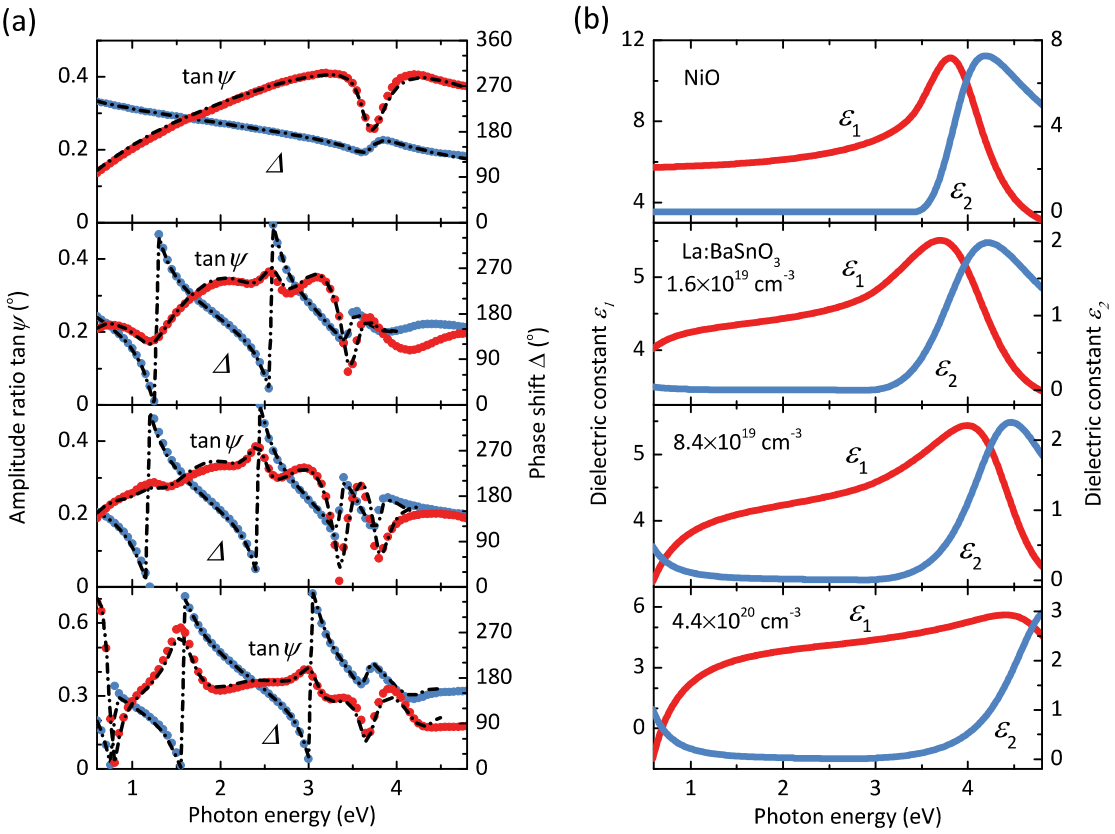


Fig. 5.8: (a) Ellipsometry spectra of amplitude ratio $\tan\Psi$ (red) and phase shift Δ (blue) of NiO film on MgO substrate and La:$BaSnO_3$/NiO bilayer structure on MgO substrate. Carrier concentrations in La:$BaSnO_3$ were 1.6×10^{19} cm^{-3}, 8.4×10^{19} cm^{-3} and 4.4×10^{20} cm^{-3} as determined by Hall effect measurements. Dashed lines to the NiO and La:$BaSnO_3$ ellipsometry spectra indicate theoretical fitting curves employing a combined model of the Drude free carrier absorption and the Tauc-Lorentz dispersion function. (b) Corresponding dielectric functions of NiO and La:$BaSnO_3$ obtained by the dispersion model analysis.

where A_L is a fitting parameter in units of energy, C is the broadening energy and E_0 is the peak transition energy, which accounts for the decrease in the optical absorption for photon energies well above the interband transition. The resulting dielectric function of the Tauc-Lorentz dispersion model is thus given by

$$\varepsilon_2^{\mathrm{TL}}(E) = \begin{cases} \frac{AE_0C(E-E_\mathrm{g})^2}{(E^2-E_0^2)^2+C^2E^2}\frac{1}{E}, & E > E_\mathrm{g} \\ 0, & E \leq E_\mathrm{g} \end{cases} \tag{5.3}$$

and

$$\varepsilon_1^{\mathrm{TL}}(E) = \varepsilon_1^{\mathrm{TL}}(\infty) + \frac{2}{\pi}P\int_{E_\mathrm{g}}^{\infty}\frac{\xi\epsilon_2(\xi)}{\xi^2-E^2}d\xi, \tag{5.4}$$

where A is a fitting parameter in units of energy and P denotes the Cauchy principal part of the Kramers-Kronig integral. The constant $\varepsilon_1^{\mathrm{TL}}(\infty)$ is defined by the Tauc-Lorentz parameters via the equality between $\varepsilon_1^{\mathrm{TL}}(0)$ and the optical dielectric constant ε_∞.

The dielectric function of the La:$BaSnO_3$ films in the spectral range from $0.2-4$ eV is described by a combination of the Drude free electron model and the Tauc-Lorentz dispersion function. Since the Tauc-Lorentz parameters show a strong correlation with the constant $\varepsilon_1^{\mathrm{TL}}(\infty)$, the low-energy IR dispersion function is determined first. Taking the free carrier absorption into account, the IR dielectric function can be written as [165]

$$\varepsilon_1(\omega) = \varepsilon_\infty - \frac{\varepsilon_\infty\omega_\mathrm{p}^2}{\omega^2+\gamma_\mathrm{p}^2}. \tag{5.5}$$

A plot of the real part ε_1 of the dielectric function obtained by mathematical inversion [166] versus $1/\left(E^2+\hbar^2\gamma_\mathrm{p}^2\right)$ yields the high frequency dielectric constant ε_∞ as intercept by linear interpolation of the low-energy region (Fig. 5.9(a)). The initial value of the broadening frequency γ_p is obtained from a fit of the Cauchy model in the spectral range $0.6-3.2$ eV, below the band gap transition. The La:$BaSnO_3$ optical dielectric constant ε_∞ decreases slightly from 4.4 to 4.1 with increasing carrier concentration (Fig. 5.9(b)).

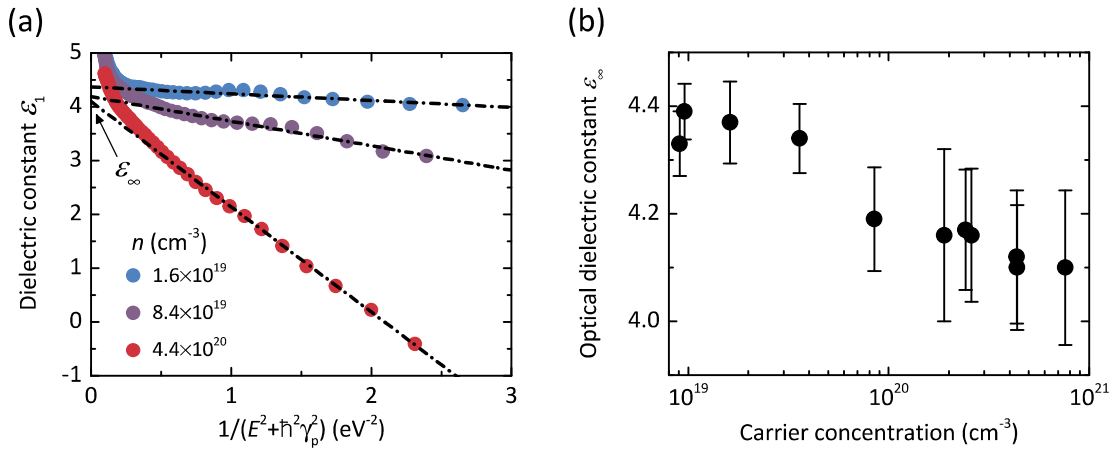


Fig. 5.9: (a) Real part ε_1 of the La:$BaSnO_3$ dielectric function as a function of $1/\left(E^2+\hbar^2\gamma_p^2\right)$. According to Eq. (5.5), the high frequency dielectric constant ε_∞ is obtained from the intercept at $1/\left(E^2+\hbar^2\gamma_p^2\right)=0$. (b) La:$BaSnO_3$ high frequency dielectric constant ε_∞ as a function of carrier concentration.

The screened plasma frequency $\sqrt{\varepsilon_\infty}\omega_p$ is then obtained by fitting the FTIR spectra ($0.2-1$ eV) using theoretical spectra [105] based on the model parameters for the dielectric function according to Eq. (5.5) and with accounting for the optical constants of the MgO substrate and NiO buffer layer. Eventually, the Tauc-Lorentz parameters are obtained by fitting the combined Drude-Tauc Lorentz model from 0.6 eV to $4-4.5$ eV energy, avoiding the complicated structures observed in the dielectric function at all energies above (Table 5.2).

With increasing carrier concentration from 1.6×10^{19} to 4.4×10^{20} cm^{-3}, the dielectric function indicates an increase in the free carrier absorption below 1 eV and a shift in the onset of the optical transition near 3.3 eV to higher energies (Fig. 2.10(b)). The Drude model parameters in Eq. (2.14) allow for calculating the electron effective mass according to Eq. (2.15). The La:$BaSnO_3$ electron effective mass increases remarkably from 0.19 to 0.36 m_0 for carrier concentrations from 1.6×10^{19} to 7.6×10^{20} cm^{-3}, respectively (Fig. 5.10).

Table 5.2: Theoretical parameters used to describe the NiO and La:$BaSnO_3$ dielectric functions using the Tauc-Lorentz dispersion model, where ε_∞ is the optical dielectric constant, E_g is correlated to the band gap energy, A is a fitting parameter in units of energy, E_0 is the peak transition energy for the Lorentz contribution, and C is the broadening energy. The Drude model for free carrier absorption comprises the plasma frequency ω_p, the broadening frequency γ_p and the electron effective mass m_e^*.

material	n	ε_∞	E_g	A	E_0	C	$\hbar\omega_p$	$\hbar\gamma_p$	m_e^*
	(cm^{-3})	-	(eV)	(eV)	(eV)	(eV)	(eV)	(eV)	(m_0)
NiO		5.7	3.4	280	3.9	0.90			
La:$BaSnO_3$	1.6×10^{19}	4.4	2.9	31	4.0	1.3	0.16	0.13	0.19
La:$BaSnO_3$	8.4×10^{19}	4.2	2.9	22	4.4	1.1	0.34	0.24	0.25
La:$BaSnO_3$	4.4×10^{20}	4.1	2.7	17	4.8	1.1	0.70	0.10	0.30

The energy dispersion E of electrons near the conduction band minimum can be described by a first-order non-parabolicity approximation [168]

$$\frac{\hbar^2 k^2}{2m_{e0}^*} = E\,(1 + \beta E)\,, \tag{5.6}$$

where $\hbar$ is the reduced Planck constant, m_{e0}^* is the electron effective mass at the conduction band minimum, $k = (3n\pi^2)^{1/3}$ is the Fermi wave vector for a parabolic conduction band and β is a fitting parameter describing the degree of non-parabolicity of the conduction band. After solving the quadratic equation (5.6) to obtain the electron energy E and applying the relation [55]

$$\frac{1}{m_e^*} = \frac{1}{\hbar^2 k}\frac{dE}{dk}, \tag{5.7}$$

the effective mass is given by

$$m_e^* = m_{e0}^* \sqrt{1 + 2\beta\,\frac{\hbar^2 k^2}{m_{e0}^*}}\,. \tag{5.8}$$

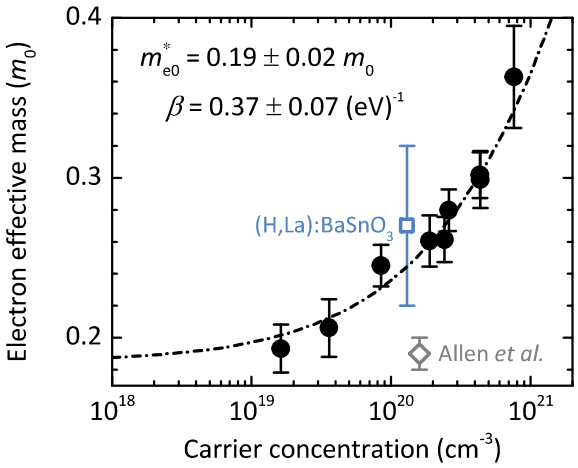


Fig. 5.10: Increase in La:$BaSnO_3$ electron effective mass with carrier concentration as determined by the plasma frequency in the Drude model for free carrier absorption (black filled circles). The IR dielectric function was obtained from transmittance/reflectivity FTIR and ellipsometry spectra. The effective mass of co-doped (H,La):$BaSnO_3$ determined in a previous analysis [26] and that of La:$BaSnO_3$ determined by Allen et al. [167] using an IR reflectivity analysis are given for comparison.

Fitting of equation (5.8) to the electron effective mass data yields $m^*_{e0} = 0.19\ m_0$ at the conduction band minimum, in good agreement with the result from hybrid density functional theory [43]. The electron effective mass obtained by Allen et al. is likely underestimated and may be corrected by a factor of $\varepsilon(\omega_p)/\varepsilon_\infty = 4.2/3.3$ to $0.24\ m_0$, following a delusive notation of the plasma frequency [167] different from Eq. (2.15), and inconsistent with its definition as the frequency for which the dielectric function equals zero. The non-parabolicity parameter $\beta = 0.37$ (eV)$^{-1}$ indicates a more pronounced increase in the La:$BaSnO_3$ effective mass with carrier concentration as compared to other transparent conducting oxides like Ga:ZnO ($\beta = 0.14$ (eV)$^{-1}$) and Sn:In_2O_3 ($\beta = 0.18$ (eV)$^{-1}$) [165], indicating a significant dependence of mobility on doping level.

5.3.4 Burstein-Moss Shift

The ellipsometry spectra in the energy range from 0.6 to 4.8 eV were analysed to extract the La:$BaSnO_3$ optical band gap independently from that of the NiO buffer layer and investigate the Burstein-Moss shift. The absorption coefficient was calculated from the dielectric function using

$$\alpha = \frac{4\pi k_\mathrm{a}}{\lambda_\mathrm{ph}} \,, \tag{5.9}$$

where k_e is the extinction coefficient and λ_ph is the photon wavelength. The band gap was determined from a plot of $(\alpha h\nu)^2$ vs. photon energy $h\nu$, where α denotes the absorption coefficient, which is valid for a direct transition at the absorption edge (Fig. 5.11(a)). Due to the conduction band filling effect, the La:$BaSnO_3$ optical absorption edge shifts from 3.7 to 4.1 eV when the carrier concentration increases from 1.6×10^{19} to 4.4×10^{20} cm^{-3}.

With increasing carrier concentration, electron-electron and electron-impurity interactions partially compensate the Burstein-Moss shift as the conduction band edge is shifted to lower energies. The band gap narrowing due to the electron-electron interactions is given by [169]

$$\Delta E_g^\mathrm{ee} = \frac{e^2 k}{2\pi^2 \varepsilon_\mathrm{s} \varepsilon_0} + \frac{e^2 \lambda}{8\pi \varepsilon_\mathrm{s} \varepsilon_0} \left(1 - \frac{4}{\pi} \tan^{-1}\left(\frac{k}{\lambda}\right)\right), \tag{5.10}$$

where $\varepsilon_\mathrm{s} = 19$ [66, 170] is the $BaSnO_3$ static dielectric constant, $\lambda = 2\sqrt{k/a_\mathrm{B}^* \pi}$ is the Thomas-Fermi screening length, $a_\mathrm{B}^* = 4\pi\varepsilon_\mathrm{s}\varepsilon_0\hbar^2/m_\mathrm{e}^* e^2$ is the effective Bohr radius and $\hbar$ is the reduced Planck constant. The band gap narrowing due to the electron-impurity interactions is given by

$$\Delta E_g^\mathrm{ei} = \frac{n e^2}{\varepsilon_\mathrm{s} \varepsilon_0 a_\mathrm{B}^* \lambda^3} \,. \tag{5.11}$$

In total, both effects contribute to ca. 0.2 eV narrowing of the optical band gap for the highest electron concentration of 7.6×10^{20} cm^{-3}. After subtraction of the conduction

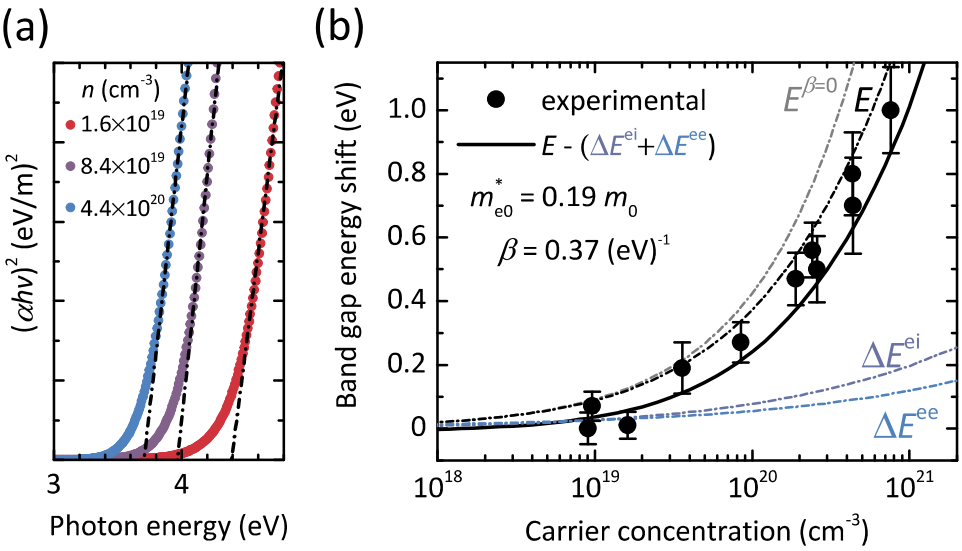


Fig. 5.11: (a) Optical absorption spectra plotted for a direct-type transition. The optical band gap shifts from 3.7 to 4.1 eV when the carrier concentration increases from 1.6×10^{19} to 4.4×10^{20} cm^{-3}. (b) Increase in the La:$BaSnO_3$ optical band gap with carrier concentration due to conduction band filling effect, where $E^{\beta=0}$ is the energy of electrons assuming a non-parabolic band dispersion. The theoretical model employs the effective mass and non-parabolicity parameter derived from the IR optical analysis to calculate the energy dispersion E of conduction band electrons. The band gap narrowing due to electron-ion (ΔE_g^{ei}) and electron-electron interactions (ΔE_g^{ee}) is taken into account.

band shifts, the Burstein-Moss shift in La:$BaSnO_3$ is described consistently with Eq. (5.6), employing the effective mass and the non-parabolicity parameter obtained from IR spectra analysis (the solid curve in Fig. 5.11(b)). As compared to a previous analysis of the Burstein-Moss shift of the indirect electronic band gap of La:$BaSnO_3$ determined by photoelectron spectroscopy [23], the present results indicate a more pronounced non-parabolicity of the conduction band and a weaker effect of many-body electron-electron and electron-impurity interactions.

5.3.5 Electrical Transport Properties

After determination of the effective mass, the mobility in La:$BaSnO_3$ can be quantitatively described using Eq. (2.8) and adopting an analytical description of the relaxation time for carrier scattering. The temperature-dependent electron transport properties for 0.3, 1.5 and and 5 at.% La-doped films show degenerate, metal-like behaviours characterized by a constant carrier concentration and only moderately increasing Hall mobility with decreasing temperature from 300 to 45 K (Fig. 5.14(a)).

Since the La (0/+) charge transition level in $BaSnO_3$ lies within the conduction band [43] (cf. Fig. 1.18), it may be assumed that all the La atoms are readily ionized to donate an electron to the reservoir of free carriers. However, the La:$BaSnO_3$ films of less than 0.3 at.% La impurity concentration ($n_{La} = 4 \times 10^{19}$ cm^{-3}) are highly resistive (Fig. 5.14(b)), which suggests trapping of free carriers by defects in the microstructure. For small doping levels, the Hall carrier concentration is indeed significantly reduced as compared to the La impurity concentration (Fig. 5.12). Above a doping level of 0.3 at.% La, the room temperature Hall mobility increases from 18 to 70 cm^2/Vs at carrier concentrations from 8.3×10^{18} to 4.4×10^{20} cm^{-3}, respectively, but then drops at higher impurity concentrations.

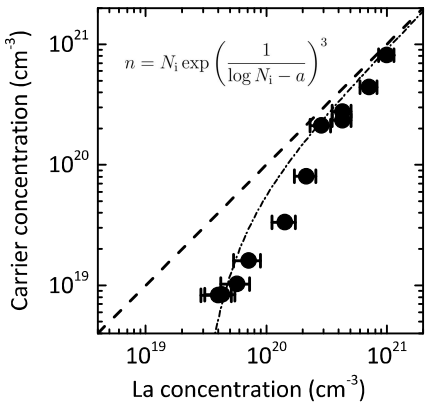


Fig. 5.12: Comparison of carrier concentration obtained by Hall measurements and La impurity concentration. The straight dashed line indicates 100% doping efficiency and the curved dotted line presents an empirical fit to the data points.

5.4 Discussion of Electron Scattering Mechanisms

The crystal mosaicity observed in the HR-XRD analysis and the microstructure in the TEM observation suggest the vertical grain boundaries as possible carrier traps. However, the activation energy of mobility, which reflects the electron transport potential barrier height and temperature-dependent scattering properties, are as low as 2.5 to 3.6 meV and significantly smaller than the thermal energy k_BT, where k_B is the Boltzmann constant and T is the absolute temperature (Fig. 5.13). Thus grain boundaries do not affect the electron transport properties at room temperature [171].

Since the $BaSnO_3$ perovskite structure consists of alternating layers of BaO and SnO_2, stacking faults including Ruddlesden-Popper-type ones are readily introduced into the microstructure when different crystal domains coalesce during thin film growth [172]. Such structural defects are observed even at the exact Ba/Sn growth stoichiometry and independent from the dislocations resulting from the structural mismatch to the substrate. Therefore, dislocation scattering is investigated as the prevailing mobility-limiting transport mechanism in $BaSnO_3$ epitaxial films for car-

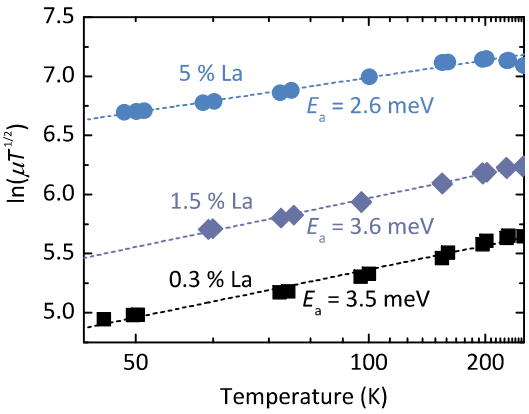


Fig. 5.13: Arrhenius-type plot of $\ln(\mu T^{\frac{1}{2}})$ for evaluation of the activation energy of electron mobility in La:$BaSnO_3$ films (cf. Ref. [171]).

rier concentrations below 1×10^{20} cm^{-3}. The dislocations which may create trap states for free electrons may explain the significantly reduced doping efficiency when the La impurity concentration is comparable to or smaller than the trap density [155]. The mobility governed by dislocation scattering in a degenerate semiconductor is described by [173]

$$\mu_{\mathrm{dis}} = \frac{8ea^2}{\pi h N_{\mathrm{dis}}} \left(\frac{3n}{\pi}\right)^{2/3} (1+\xi_0)^{3/2}\,, \tag{5.12}$$

where

$$\xi_0 = \frac{\varepsilon_{\mathrm{s}}\varepsilon_0 h^2}{m_{\mathrm{e}}^* e^2} \left(3\pi^2 n\right)^{1/3}, \tag{5.13}$$

and a is the $BaSnO_3$ lattice parameter, h is the Planck constant and N_{dis} is the dislocation density. For carrier concentrations above 1×10^{20} cm^{-3}, the room temperature mobility in $BaSnO_3$ is governed by electron-phonon interactions and electron scattering at ionized La impurities [174]. The mobility governed by longitudinal optical (LO) phonon scattering is calculated according to [175, 176]

$$\mu_{\mathrm{LO}_\mu} = \frac{e}{m_{\mathrm{e}}^*} \frac{1}{2c_\mu \omega_{\mathrm{l}_\mu}} \left(1+\frac{c_\mu}{6}\right)^{-3} f(c_\mu) \left(\exp\left(\frac{\hbar\omega_{\mathrm{l}_\mu}}{k_{\mathrm{B}}T}\right) - 1\right) \tag{5.14}$$

where c_μ is the electron-phonon coupling constant proportional to the square root

of electron effective mass $\sqrt{m_e^*}$, ω_{l_μ} is the frequency of the LO phonon mode and $f(c_\mu)$ is a slowly varying function ranging from 1.0 to 1.2 for $0 < c_\mu < 3$ [177]. In La:$BaSnO_3$, the three LO phonon modes with $\hbar\omega_l = 18$, 55 and 96 meV energy are taken into account [66, 170] to calculate an effective mobility μ_{LO} using the sum of reciprocals for each phonon mode, using $\mu_{LO}^{-1} = \sum_\mu \mu_{LO_\mu}^{-1}$ [178]. The mobility governed by ionized impurity scattering in a degenerate semiconductor [179, 180], taking the non-parabolicity of the conduction band into account [181], is given by

$$\mu_{imp} = \frac{3\varepsilon_s^2\varepsilon_0^2 h^3}{m_e^{*2} e^3} \frac{n}{N_i} \frac{1}{F} , \tag{5.15}$$

where F is the screening function

$$F = \left(1 + 4\frac{\xi_1}{\xi_0}\left(1 - \frac{\xi_1}{8}\right)\right)\ln(1+\xi_0) - \frac{\xi_0}{1+\xi_0} - 2\xi_1\left(1 - \frac{5}{16}\xi_1\right) \tag{5.16}$$

and

$$\xi_1 = 1 - \frac{m_{e0}^*}{m_e^*} . \tag{5.17}$$

N_i is the concentration of ionized impurities, which is equal to the La concentration assuming that all the La impurity atoms donate one electron each. According to the Matthiessen's rule, the resulting mobility is

$$\mu_{res}^{-1} = \mu_{dis}^{-1} + \mu_{LO}^{-1} + \mu_{imp}^{-1} , \tag{5.18}$$

which describes the dependence on temperature and carrier concentration over the entire range of investigation (Fig. 5.14).

The analysis according to equations (5.12) to (5.15) shows that the high La:$BaSnO_3$ mobility is mainly attributed to two quantities, the small electron effective mass and the large static dielectric constant. The room-temperature effective mass increases pronouncedly from $m_e^* = 0.19\ m_0$ to $0.36\ m_0$ for the range of the carrier concentrations investigated in this work. This is reflected by the large non-parabolicity parameter $\beta = 0.37\ (\mathrm{eV})^{-1}$ and noticeably reduces the mobility at the highest doping

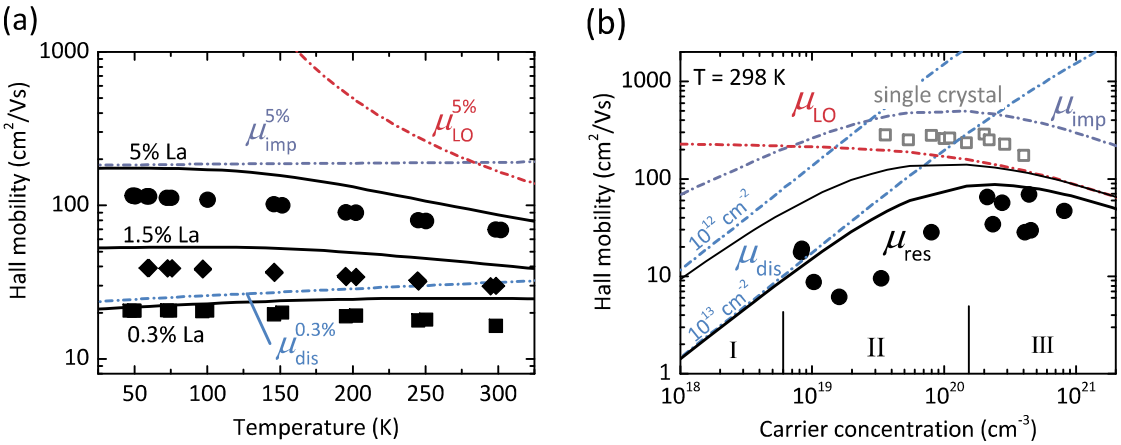


Fig. 5.14: (a) Temperature-dependent Hall mobility of 0.3 %, 1.5 % and 5 % La-doped $BaSnO_3$ films indicates degenerate, metal-like transport behaviours, which is dominated by dislocation scattering for low doping levels and ionized impurity and LO optical phonon scattering for high doping levels. Solid lines present theoretical calculation of the mobility using the three analytical scattering models according to Eqs. (5.12), (5.14), (5.15) and (5.18). (b) La:$BaSnO_3$ films are too resistive to measure Hall voltages for doping levels below 0.3% La (I). The room temperature Hall mobility of the degenerate La:$BaSnO_3$ films is governed by dislocation scattering in the intermediate doping regime (II) and LO optical phonon and ionized impurity scattering in the high doping regime (III). The mobility of La:$BaSnO_3$ crystals is given for comparison (grey open squares, after Kim et al. [96]).

levels concurrent with an increase in the polaron mass. However, the large dielectric constant $\varepsilon_s = 19$ [66, 170] of $BaSnO_3$ promotes screening of the Coulomb potential of charged dislocations and ionized La impurities [96]. The square dependence of mobility governed by impurity scattering on dielectric constant shows that in contrast to other high mobility wide band gap semiconductors like ZnO ($\varepsilon_s^{\perp} = 7.4$ [182]), In_2O_3 ($\varepsilon_s = 8.9$ [183]) and GaN ($\varepsilon_s^{\perp} = 9.5$ [184]), $BaSnO_3$ may exhibit a large mobility even at unusually high carrier concentrations because impurity scattering does not become significant. Furthermore, electron-phonon scattering is less pronounced as compared to other polar oxides such as $SrTiO_3$ ($\sim$10 cm^2/Vs [185]) and Ga_2O_3 ($\sim$115 cm^2/Vs [186]), allowing to achieve an extraordinary high $\sim$300 cm^2/Vs mobility even at room temperature [170, 174].

Further progress in the development of $BaSnO_3$ epitaxial films for application in transparent oxide electronics may be realized not only by considering the lattice mismatch with the substrate, but also by optimising epitaxial growth techniques to reduce dislocation densities and domain boundaries which are inherent to the perovskite structure. Selective-area growth and epitaxial lateral overgrowth techniques as successfully applied in III-nitride semiconductor technology [187] may present effective methods for achieving higher mobilities by reducing the dislocation density of the present $BaSnO_3$ epitaxial films.

5.5 Conclusion

In conclusion, the degenerate perovskite $BaSnO_3$ exhibits an extraordinary high room temperature mobility attributed to an electron effective mass as small as 0.19 m_0. An in-depth investigation of the infrared free carrier absorption and the Burstein-Moss shift yields a significant dependence of electron effective mass on doping level, concurrent with a pronounced non-parabolicity of the conduction band.

The current room temperature mobility limits in epitaxial films are determined by scattering at dislocations at low doping levels, and ionized impurity scattering and electron-phonon interactions at high doping levels. The large dielectric constant of $BaSnO_3$ facilitates the screening of charged defects and ionized impurities more than in other transparent semiconductor and electron-phonon scattering is less pronounced as compared to other polar oxide semiconductors, resulting in an enhanced room-temperature mobility even at unusually high carrier concentrations.

6 Summary and Conclusion

This thesis investigated the origin of the pronounced band gap narrowing in $Ni_xMg_{1-x}O$, a fully miscible solid solution of the important p-type transparent oxide NiO and MgO relevant for application in tunable deep-UV photo detectors. The second part of this thesis investigated an effective crystal growth method for the emerging high-mobility perovskite TCO La:$BaSnO_3$, the doping with previously unexplored electron donor H, the La:$BaSnO_3$ electron effective mass dependence on doping level and electron transport properties in epitaxial thin films.

Chapter 3 of this thesis resolved the controversy over the strikingly non-parabolic band gap bowing in the $Ni_xMg_{1-x}O$ solid solution in the literature. While previous reports claimed that the origin of the unusual band gap bowing may be ascribed to apparent compositional inhomogeneities, the structural investigations on epitaxial $Ni_xMg_{1-x}O$ thin films presented in this thesis do not indicate any deviations of the material from a fully miscible, structurally and compositionally homogeneous solid solution. The pronounced band gap narrowing of $Ni_xMg_{1-x}O$ is instead attributed to the fundamental difference in electronic structure between NiO and MgO. The transition metal oxide NiO forms Ni 3d levels inside the MgO band gap even for small NiO concentrations of 12 at.%, resulting in a reduced 4.8 eV optical band gap as compared to the large 7.8 eV band gap of pure MgO. The standard bowing theory has been rigidly applied to describe the $Ni_xMg_{1-x}O$ band gap dependence in the literature, even though it may in general not be valid for semiconductor systems,

in which one of the alloy end members creates deep electronic levels in the band gap. The results demonstrate that the $Ni_xMg_{1-x}O$ band gap dependence on composition is simply described by a linear interpolation of the band gaps of NiO and Ni impurity doped MgO.

An effective solid phase epitaxy method for preparation of high-mobility La:$BaSnO_3$ thin films of single crystal-like structure using the room temperature-deposited nanocrystalline phase as precursor was presented in Chapter 4. The low La dopant activation of about $9 - 16$ % is attributed to dislocations in epitaxial La:$BaSnO_3$ thin films which act as carrier traps and the La segregation at grain boundaries due to the limited solubility in $BaSnO_3$ and the high temperature crystallization process. Up to present, best doping results have been achieved using La substitutional doping on the Ba-site in $BaSnO_3$. This thesis presents the first experimental report of interstitial H doping in $BaSnO_3$ films, which is the second most effective n-type doping possibility to enhance carrier concentrations reported up to present. H-doping by plasma treatment may be carried out at room-temperature and can be combined with La-doping to significantly enhance the conductivity. This new doping option opens up new functionality for devices since interstitial H may be released again upon annealing.

Chapter 5 of this thesis investigated the origin of the high room temperature mobility in degenerate perovskite $BaSnO_3$. A small conduction band electron effective mass of only 0.19 m_0 is determined independently from analysis of the carrier absorption observed in infrared spectra. A significant increase in electron effective mass on doping level is observed, in agreement with a large Burstein-Moss shift, which is concurrent with a pronounced non-parabolicity of the conduction band. The thesis presents the first quantitative analysis of the current electron mobility limits in La:$BaSnO_3$ epitaxial films, which are determined by scattering at dislocations and ionized impurities. The large dielectric constant of $BaSnO_3$ facilitates the screening

of defects more than in other transparent semiconductors, resulting in an enhanced mobility even at unusually high carrier concentrations. The results demonstrate the potential of $BaSnO_3$ to outperform established wide-band gap semiconductors such In_2O_3, ZnO and even GaN.

The thesis results demonstrate that intriguing properties of emerging transparent conducting oxides are yet to be discovered when present research departs from the conventional materials SnO_2, In_2O_2, ZnO and CdO, which historically dominated this research field since the 1950's. The investigation of novel classes of transparent conducting oxides may result in more innovative material design concepts or and a thorough understanding of previously unexpected physical properties.

In this context, the fundamental understanding of the largely irregular band gap bowing in the $Ni_xMg_{1-x}O$ system presented in this work shows how well-established theories are often rigidly applied, thereby overlooking scientifically interesting and conceptionally different semiconductor physics. Likewise worth investigating, the unprecedented high room-temperature mobility in $BaSnO_3$ has created an immediate research fever to understand the physics of perovskite stannates in great detail. The present results elucidating the electron transport may be of great interest for researchers which recently turned to investigating $BaSnO_3$ for application in high performance thin-film transistors or more interestingly from a scientist's perspective, aim at the development of further emerging wide-band gap perovskites whose intriguing properties are yet to be discovered and understood.

Appendix: P-type Conduction in $Ni_xMg_{1-x}O$

Chapter 3 described the origin of the non-parabolic band gap bowing of undoped $Ni_xMg_{1-x}O$. It was found that by alloying just a small amount of NiO with MgO, the band gap is already drastically reduced due to Ni 3d e_g states which form deep levels inside the MgO band gap. Nevertheless, the $Ni_xMg_{1-x}O$ band gap can be tailored within the range of 3.7 eV−4.8 eV for $1 \leq x \leq 0.12$. In this appendix, the prospect of p-type conduction in wide band gap UV transparent epitaxial Li:$Ni_xMg_{1-x}O$ films is discussed.

Single-phase polycrystalline $5 - 10$ at.% Li:$Ni_xMg_{1-x}O$ (x=1, 0.8 and 0.6) ceramic targets were prepared by sintering high purity $LiCO_3$, NiO and MgO powders at temperatures of 900 °C for 36 h. $Ni_xMg_{1-x}O$ thin films were grown on single-crystal MgO(100) substrates by pulsed laser ablation of the Li:$Ni_xMg_{1-x}O$ ceramic targets using a 248 nm KrF excimer laser. The growth temperature was 600 °C and the deposition pressure was 0.7 Pa O_2. The Li:$Ni_xMg_{1-x}O$ ceramic targets were ablated with a laser beam fluency of 0.8 J/cm^2 per pulse at a frequency of 10 Hz, resulting in a film thickness of about 300 nm. AC Hall measurements were performed with a LakeShore 8400 system (Toyo Co.) using the four-terminal method with sputtered Au/Ti contacts in van der Pauw geometry. The optical transmission of the Li:$Ni_xMg_{1-x}O$ films were measured with a Cary 5000 UV-Vis-NIR spectrophotometer using a bare MgO

substrate as 100% transmission reference.

By alloying 5 at. % and 10 at.% Li:NiO films with a fraction of only 20 at.% MgO, the resistivity increases by more than 2 orders of magnitude due to a significant drop in carrier concentration from about 8 $\times$ 10^{20} cm^{-3} to 1×10^{18} cm^{-3} (Table A.1). The Hall mobility is constant regardless of the MgO alloying content and the maximum value of $\sim$0.06 cm^2/Vs is very similar to that obtained for Li:NiO films prepared by solid phase epitaxy [85]. However, the hole transport properties are inferior to those reported for polycrystalline, semi-transparent NiO films prepared by magnetron sputtering at 200 °C and 0.8 Pa O_2 deposition pressure with a maximum Hall mobility of $\sim$3 cm^2/Vs [83]. The Hall voltage measured for Li:$Ni_{0.6}Mg_{0.4}O$ films was too small to determine the transport properties, which is attributed to a significant drop in carrier concentration and a small mobility.

Table A.1: Hole transport properties of epitaxial Li:$Ni_xMg_{1-x}O$ (x = 1, 0.8 and 0.6) thin films.

Material	Li concentration at.%	Resistivity (Ωcm)	Carrier concentration (cm^{-3})	Hall mobility (cm^2/Vs)
NiO	10	0.32	7.5×10^{20}	2.6×10^{-2}
	5	3.2	6.3×10^{20}	3.1×10^{-3}
$Ni_{0.8}Mg_{0.2}O$	10	25	4.0×10^{18}	6.2×10^{-2}
	5	1.1×10^{3}	1.3×10^{18}	5.4×10^{-3}
$Ni_{0.6}Mg_{0.4}O$	10	46	-	-

The comparison of optical transmission spectra of undoped and Li:$Ni_{0.8}Mg_{0.2}O$ thin films shows a significant drop in transparency for visible light when the Li doping concentration is increased (Fig. A.1). It follows that a reasonable good p-type conductivity is achieved at the cost of optical transparency.

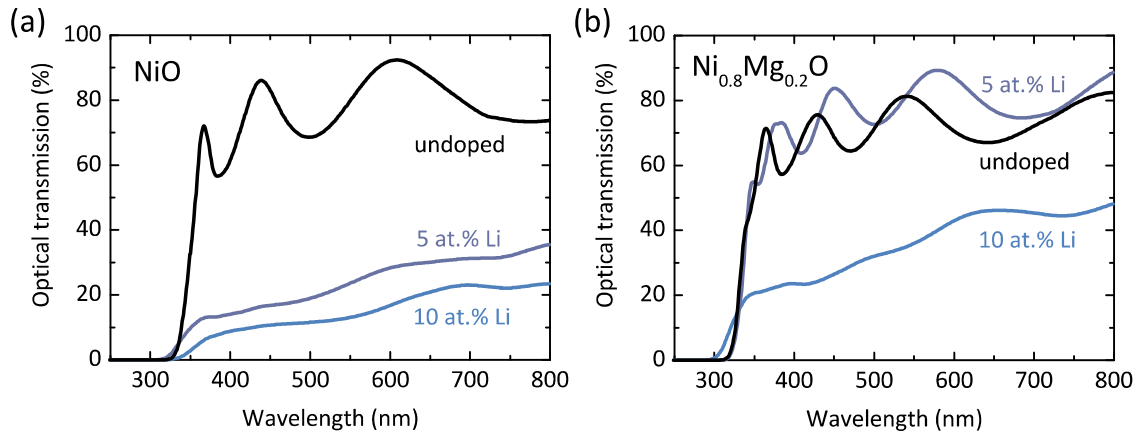


Fig. A.1: Optical transmission spectra of undoped and Li-doped (a) NiO and (b) $Ni_{0.8}Mg_{0.2}O$ thin films indicating the significant loss in transparency in the visible region for high Li doping concentrations.

While Li doping is an effective method to obtain good p-type conduction in NiO thin films, only a small hole concentration can be achieved in Li:$Ni_xMg_{1-x}O$ films with MgO contents of 20 at. % prepared under the same conditions. It is likely that the holes introduced by Li acceptors may readily be compensated by formation of O vacancies (V_O) which have very low formation energy in MgO (see section 1.3). A recent combined experimental and theoretical study of defects in Li:MgO corroborates this argument and suggests formation of defect complexes such as $2Li_{Mg}V_O$ which neutralizes Li acceptors [188]. Such defects may play a role as compensating centres in Li:$Ni_xMg_{1-x}O$, but theoretical studies of the defect chemistry in this system will be required to investigate the origin of hole compensation in more detail.

In conclusion, by allowing NiO with 20 at. % MgO the band gap increased only marginally from 3.7 eV to 3.9 eV. At the same time, the propensity to p-type conduction decreases drastically for Li:$Ni_{0.8}Mg_{0.2}O$ as compared to Li:NiO. Hole compensating defects and defect complexes, such as V_O and $2Li_{Mg}V_O$, respectively, are likely to have small formation energies in $Ni_xMg_{1-x}O$. Furthermore, a compromise must be

made between realizing good p-type conductivity and the loss of transparency by Li doping. Therefore, Li-doped $Ni_xMg_{1-x}O$ alloys do not offer prospects for increasing the band gap of NiO beyond 3.7 eV without degradation of its hole transport properties or optical transparency.

Copyright Acknowledgements

Figures which have been reused from publications of other authors for display in this thesis are indicated in Tab. A.2. The permission for reproduction has been sought where possible and references to original publications are provided below and in the corresponding figure captions. The contents are used for academic purposes only and the copyright remains with the original author and/or publishing company.

The right of reusing contents of my own publications, including all text, tables, figures and supplementary information is granted by all publishing companies to which material of this thesis has been submitted (Nature Publishing Group, AIP Publishing LLC and American Physical Society). Copies of permission documents are available upon request.

Table A.2: List of copyright figures for which a license has been obtained for re-use in this dissertation or for which no licence is required.

Figure	Author	Reference	Licence no. / comments
1.1	Dr Wang	[1]	3894070886415
1.3	T. Minami	[18]	permission granted w/o licence no.
1.4	G.B. Haxel *et al.*	[34]	permission granted w/o licence no.
1.5	A. Ohtomo *et al.*	[9]	3895411109948
1.6	A. Tsukazaki *et al.*	[37]	3895411438753
1.8	A. Zunger	[48]	3897090503916
1.10	M. Goano *et al.*	[54]	3897081022628
1.11	D. Scanlon *et al.*	[56]	3897101374733
1.12	K. Ueda *et al.*	[59]	3897110142113
1.13	V. Prostakova *et al.*	[71]	3897110652055
1.14	R. Gillen *et al.*	[77]	permission granted w/o licence no.
1.15	U. Schönberger *et al.*	[79]	3897120260959
1.16	S. Lany *et al.*	[42]	3897120500850
1.17	H. Mizoguchi *et al.*	[91]	permission granted w/o licence no.
1.18	D. Scanlon	[43]	3897130176783
1.20	H. J. Kim *et al.*	[19]	permission granted w/o licence no.
1.20	W.-J. Lee *et al.*	[24]	3897130980819
1.20	Z. Lebens-Higgins *et al.*	[23]	no licence required
1.20	S. Raghavan *et al.*	[25]	3897131135716
3.9 (a)	J. Kübler *et al.*	[130]	3942300307467
3.9 (b)	G. Timmer *et al.*	[131]	3942301387247

References

[1] K. Takahashi, A. Yoshikawa and A. Sandhu. *Fundamental Properties of Wide Bandgap Semiconductors.* Springer Berlin Heidelberg, (2010).

[2] 'The Nobel Prize in Physics 2014'. Nobelprize.org. Nobel Media AB 2014. Web. 26 May 2016. <http://www.nobelprize.org/nobel_prizes/physics/laureates/2014/>.

[3] Y. Taniyasu, M. Kasu and T. Makimoto. An aluminium nitride light-emitting diode with a wavelength of 210 nanometres. *Nature* **441**, 325 (2006).

[4] H. Hirayama, A. Kinoshita, T. Yamabi, Y. Enomoto, A. Hirata, T. Araki, Y. Nanishi and Y. Aoyagi. Marked enhancement of 320-360 nm ultraviolet emission in quaternary $In_xAl_yGa_{1-x-y}N$ with In-segregation effect. *Applied Physics Letters* **80**, 207 (2002).

[5] S. D. Lester, F. A. Ponce, M. G. Craford and D. A. Steigerwald. High dislocation densities in high efficiency GaN-based light-emitting diodes. *Applied Physics Letters* **66**, 1249 (1995).

[6] T. Obata, H. Hirayama, Y. Aoyagi and K. Ishibashi. Growth and annealing conditions of high Al-content p-type AlGaN for deep-UV LEDs. *Physica status solidi (a)* **201**, 2803 (2004).

[7] H. Amano, N. Sawaki, I. Akasaki and Y. Toyoda. Metalorganic vapor phase epitaxial growth of a high quality GaN film using an AlN buffer layer. *Applied Physics Letters* **48**, 353 (1986).

[8] Y. Segawa, A. Ohtomo, M. Kawasaki, H. Koinuma, Z. K. Tang, P. Yu and G. K. L. Wong. Growth of ZnO Thin Film by Laser MBE: Lasing of Exciton at Room Temperature. *Physica status solidi (b)* **202**, 669 (1997).

[9] A. Ohtomo, K. Tamura, K. Saikusa, K. Takahashi, T. Makino, Y. Segawa, H. Koinuma and M. Kawasaki. Single crystalline ZnO films grown on lattice-matched $ScAlMgO_4(0001)$ substrates. *Applied Physics Letters* **75**, 2635 (1999).

[10] A. Tsukazaki, A. Ohtomo, T. Onuma, M. Ohtani, T. Makino, M. Sumiya, K. Ohtani, S. F. Chichibu, S. Fuke, Y. Segawa, H. Ohno, H. Koinuma and M. Kawasaki. Repeated temperature modulation epitaxy for p-type doping and light-emitting diode based on ZnO. *Nat Mater* **4**, 42 (2005).

[11] Y. Ryu, T.-S. Lee, J. A. Lubguban, H. W. White, B.-J. Kim, Y.-S. Park and C.-J. Youn. Next generation of oxide photonic devices: ZnO-based ultraviolet light emitting diodes. *Applied Physics Letters* **88**, 241108 (2006).

[12] K. Katayama, H. Matsubara, F. Nakanishi, T. Nakamura, H. Doi, A. Saegusa, T. Mitsui, T. Matsuoka, M. Irikura, T. Takebe, S. Nishine and T. Shirakawa. ZnSe-based whiteLEDs. *Journal of Crystal Growth* **214**, 1064 (2000).

[13] M. Adachi, Z. M. Aung, K. Minami, K. Koizumi, M. Watanabe, S. Kawamoto, T. Yamaguchi, H. Kasada, T. Abe, K. Ando, K. Nakano, A. Ishibashi and S. Itoh. Microscopic defect induced slow-mode degradation in II-VI based blue-green laser diodes. *Journal of Crystal Growth* **214**, 1035 (2000).

[14] G. Ziegler, P. Lanig, D. Theis and C. Weyrich. Single crystal growth of SiC substrate material for blue light emitting diodes. *IEEE Transactions on Electron Devices* **30**, 277 (1983).

[15] S. Koizumi, K. Watanabe, M. Hasegawa and H. Kanda. Ultraviolet Emission from a Diamond pn Junction. *Science* **292**, 1899 (2001).

[16] H. Taniuchi, H. Umezawa, T. Arima, M. Tachiki and H. Kawarada. High-frequency performance of diamond field-effect transistor. *IEEE Electron Device Letters* **22**, 390 (2001).

[17] D. S. Ginley, H. Hosono and D. C. Paine. *Handbook of Transparent Conductors.* Springer US, (2011).

[18] T. Minami. Transparent conducting oxide semiconductors for transparent electrodes. *Semiconductor Science and Technology* **20**, S35 (2005).

[19] H. J. Kim, U. Kim, H. M. Kim, T. H. Kim, H. S. Mun, B.-G. Jeon, K. T. Hong, W.-J. Lee, C. Ju, K. H. Kim and K. Char. High Mobility in a Stable Transparent Perovskite Oxide. *Applied Physics Express* **5**, 061102 (2012).

[20] H. F. Wang, Q. Z. Liu, F. Chen, G. Y. Gao, W. Wu and X. H. Chen. Transparent and conductive oxide films with the perovskite structure: La- and Sb-doped $BaSnO_3$. *Journal of Applied Physics* **101**, 106105 (2007).

[21] Q. Liu, J. Dai, Z. Liu, X. Zhang, G. Zhu and G. Ding. Electrical and optical properties of Sb-doped $BaSnO_3$ epitaxial films grown by PLD. *J. Phys. D* **43**, 455401 (2010).

[22] P. V. Wadekar, J. Alaria, M. O'Sullivan, N. L. O. Flack, T. D. Manning, L. J. Phillips, K. Durose, O. Lozano, S. Lucas, J. B. Claridge and M. J. Rosse-

insky. Improved electrical mobility in highly epitaxial La:$BaSnO_3$ films on $SmScO_3$(110) substrates. *Applied Physics Letters* **105**, 052104 (2014).

[23] Z. Lebens-Higgins, D. O. Scanlon, H. Paik, S. Sallis, Y. Nie, M. Uchida, N. F. Quackenbush, M. J. Wahila, G. E. Sterbinsky, D. A. Arena, J. C. Woicik, D. G. Schlom and L. F. J. Piper. Direct Observation of Electrostatically Driven Band Gap Renormalization in a Degenerate Perovskite Transparent Conducting Oxide. *Phys. Rev. Lett.* **116**, 027602 (2016).

[24] W.-J. Lee, H. J. Kim, E. Sohn, T. H. Kim, J.-Y. Park, W. Park, H. Jeong, T. Lee, J. H. Kim, K.-Y. Choi and K. H. Kim. Enhanced electron mobility in epitaxial (Ba,La)SnO_3 films on $BaSnO_3$(001) substrates. *Applied Physics Letters* **108**, 082105 (2016).

[25] S. Raghavan, T. Schumann, H. Kim, J. Y. Zhang, T. A. Cain and S. Stemmer. High-mobility $BaSnO_3$ grown by oxide molecular beam epitaxy. *APL Mater.* **4**, 016106 (2016).

[26] C. A. Niedermeier, S. Rhode, S. Fearn, K. Ide, M. A. Moram, H. Hiramatsu, H. Hosono and T. Kamiya. Solid phase epitaxial growth of high mobility La:$BaSnO_3$ thin films co-doped with interstitial hydrogen. *Applied Physics Letters* **108**, 172101 (2016).

[27] J. Shiogai, K. Nishihara, K. Sato and A. Tsukazaki. Improvement of electron mobility in La:$BaSnO_3$ thin films by insertion of an atomically flat insulating (Sr,Ba)SnO_3 buffer layer. *AIP Advances* **6**, 065305 (2016).

[28] H. Hosono, N. Kikuchi, N. Ueda and H. Kawazoe. Working hypothesis to explore novel wide band gap electrically conducting amorphous oxides and examples. *Journal of Non-Crystalline Solids* **198-200**, 165 (1996).

[29] K. Nomura, H. Ohta, A. Takagi, T. Kamiya, M. Hirano and H. Hosono. Room-temperature fabrication of transparent flexible thin-film transistors using amorphous oxide semiconductors. *Nature* **432**, 488 (2004).

[30] E. M. C. Fortunato, L. M. N. Pereira, P. M. C. Barquinha, A. M. Botelho do Rego, G. Goncalves, A. Vila , J. R. Morante and R. F. P. Martins. High mobility indium free amorphous oxide thin film transistors. *Applied Physics Letters* **92**, 222103 (2008).

[31] E. Fortunato, D. Ginley, H. Hosono and D. C. Paine. Transparent Conducting Oxides for Photovoltaics. *MRS Bulletin* **32**, 242 (2007).

[32] S. Ismail-Beigi, F. J. Walker, S.-W. Cheong, K. M. Rabe and C. H. Ahn. Alkaline earth stannates: The next silicon? *APL Mater.* **3**, 062510 (2015).

[33] K. Krishnaswamy, L. Bjaalie, B. Himmetoglu, A. Janotti, L. Gordon and C. G. Van de Walle. $BaSnO_3$ as a channel material in perovskite oxide heterostructures. *Applied Physics Letters* **108**, 083501 (2016).

[34] G. B. Haxel, J. B. Hedrick, G. J. Orris, P. H. Stauffer and J. W. H. II. Rare Earth Elements - Critical Resources for High Technology. http://pubs.usgs.gov/fs/2002/fs087-02/, (2002). Accessed: 2016-04-27.

[35] M. Kneissl, T. Kolbe, C. Chua, V. Kueller, N. Lobo, J. Stellmach, A. Knauer, H. Rodriguez, S. Einfeldt, Z. Yang, N. M. Johnson and M. Weyers. Advances in group III-nitride-based deep UV light-emitting diode technology. *Semiconductor Science and Technology* **26**, 014036 (2011).

[36] H. Amano, T. Asahi and I. Akasaki. Stimulated Emission Near Ultraviolet at Room Temperature from a GaN Film Grown on Sapphire by MOVPE Using an AlN Buffer Layer. *Japanese Journal of Applied Physics* **29**, L205 (1990).

[37] A. Tsukazaki, A. Ohtomo and M. Kawasaki. High-mobility electronic transport in ZnO thin films. *Applied Physics Letters* **88**, 152106 (2006).

[38] K. Tamura, A. Ohtomo, K. Saikusa, Y. Osaka, T. Makino, Y. Segawa, M. Sumiya, S. Fuke, H. Koinuma and M. Kawasaki. Epitaxial growth of ZnO films on lattice-matched $ScAlMgO_4(0001)$ substrates. *Journal of Crystal Growth* **214**, 59 (2000).

[39] R. D. Shannon. Revised effective ionic radii and systematic studies of interatomic distances in halides and chalcogenides. *Acta Crystallographica Section A* **32**, 751 (1976).

[40] M. Trari, J.-P. Doumerc, P. Dordor, M. Pouchard, G. Behr and G. Krabbes. Preparation and characterization of lanthanum doped BaSnO3. *Journal of Physics and Chemistry of Solids* **55**, 1239 (1994).

[41] W. Walukiewicz, S. Li, J. Wu, K. Yu, J. A. III, E. Haller, H. Lu and W. J. Schaff. Optical properties and electronic structure of InN and In-rich group III-nitride alloys. *Journal of Crystal Growth* **269**, 119 (2004).

[42] S. Lany, J. Osorio-Guillén and A. Zunger. Origins of the doping asymmetry in oxides: Hole doping in NiO versus electron doping in ZnO. *Phys. Rev. B* **75**, 241203 (2007).

[43] D. O. Scanlon. Defect engineering of $BaSnO_3$ for high-performance transparent conducting oxide applications. *Phys. Rev. B* **87**, 161201 (2013).

[44] S. Lany and A. Zunger. Assessment of correction methods for the band-gap problem and for finite-size effects in supercell defect calculations: Case studies for ZnO and GaAs. *Phys. Rev. B* **78**, 235104 (2008).

[45] S. B. Zhang, S.-H. Wei and A. Zunger. A phenomenological model for systematization and prediction of doping limits in II-VI and III-VI compounds. *Journal of Applied Physics* **83**, 3192 (1998).

[46] S. B. Zhang, S.-H. Wei and A. Zunger. Microscopic Origin of the Phenomenological Equilibrium 'Doping Limit Rule" in n-Type III-V Semiconductors. *Phys. Rev. Lett.* **84**, 1232 (2000).

[47] W. Walukiewicz. Intrinsic limitations to the doping of wide-gap semiconductors. *Physica B: Condensed Matter* **302**, 123 (2001).

[48] A. Zunger. Practical doping principles. *Applied Physics Letters* **83**, 57 (2003).

[49] C. G. Van de Walle and J. Neugebauer. Universal alignment of hydrogen levels in semiconductors, insulators and solutions. *Nature* **423**, 626 (2003).

[50] J. Robertson, K. Xiong and S. Clark. Band gaps and defect levels in functional oxides. *Thin Solid Films* **496**, 1 (2006).

[51] P. D. C. King, T. D. Veal, D. J. Payne, A. Bourlange, R. G. Egdell and C. F. McConville. Surface Electron Accumulation and the Charge Neutrality Level in In_2O_3. *Phys. Rev. Lett.* **101**, 116808 (2008).

[52] L. Bjaalie, B. Himmetoglu, L. Weston, A. Janotti and C. G. V. de Walle. Oxide interfaces for novel electronic applications. *New Journal of Physics* **16**, 025005 (2014).

[53] A. Janotti and C. G. V. de Walle. Fundamentals of zinc oxide as a semiconductor. *Reports on Progress in Physics* **72**, 126501 (2009).

[54] M. Goano, E. Bellotti, E. Ghillino, G. Ghione and K. F. Brennan. Band structure nonlocal pseudopotential calculation of the III-nitride wurtzite phase ma-

terials system. Part I. Binary compounds GaN, AlN, and InN. *Journal of Applied Physics* **88**, 6467 (2000).

[55] R. E. Hummel. *Electronic Properties of Materials.* Springer-Verlag New York, 4th edition, (2011).

[56] D. O. Scanlon and G. W. Watson. On the possibility of p-type SnO2. *J. Mater. Chem.* **22**, 25236 (2012).

[57] H. Kawazoe, M. Yasukawa, H. Hyodo, M. Kurita, H. Yanagi and H. Hosono. P-type electrical conduction in transparent thin films of $CuAlO_2$. *Nature* **389**, 939 (1997).

[58] A. Kudo, H. Yanagi, H. Hosono and H. Kawazoe. $SrCu_2O_2$: A p-type conductive oxide with wide band gap. *Applied Physics Letters* **73**, 220 (1998).

[59] K. Ueda, H. Hiramatsu, H. Ohta, M. Hirano, T. Kamiya and H. Hosono. Single-atomic-layered quantum wells built in wide-gap semiconductors LnCuOCh. *Phys. Rev. B* **69**, 155305 (2004).

[60] C. Kittel. *Introduction to Solid State Physics.* New York, Wiley, 7th edition edition, (1996).

[61] Y. Chen, D. M. Bagnall, H.-j. Koh, K.-t. Park, K. Hiraga, Z. Zhu and T. Yao. Plasma assisted molecular beam epitaxy of ZnO on c-plane sapphire: Growth and characterization. *Journal of Applied Physics* **84**, 3912 (1998).

[62] P. J. Gielisse, J. N. Plendl, L. C. Mansur, R. Marshall, S. S. Mitra, R. Mykolajewycz and A. Smakula. Infrared Properties of NiO and CoO and Their Mixed Crystals. *Journal of Applied Physics* **36**, 2446 (1965).

[63] M. A. Subramanian, R. D. Shannon, B. H. T. Chai, M. M. Abraham and M. C. Wintersgill. Dielectric constants of BeO, MgO, and CaO using the two-terminal method. *Physics and Chemistry of Minerals* **16**, 741 (1989).

[64] K. Hisano and K. Toda. Temperature dependence of optical modes of vibration in MgO thin film. *Journal of Physics C: Solid State Physics* **15**, 1111 (1982).

[65] D. M. Roessler and W. C. Walker. Electronic Spectrum and Ultraviolet Optical Properties of Crystalline MgO. *Phys. Rev.* **159**, 733 (1967).

[66] T. N. Stanislavchuk, A. A. Sirenko, A. P. Litvinchuk, X. Luo and S.-W. Cheong. Electronic band structure and optical phonons of $BaSnO_3$ and $Ba_{0.97}La_{0.03}SnO_3$ single crystals: Theory and experiment. *Journal of Applied Physics* **112**, 044108 (2012).

[67] G. L. Harris. *Properties of Silicon Carbide.* IEE, INSPEC, London, (1995).

[68] T. Makino, Y. Segawa, M. Kawasaki and H. Koinuma. Optical properties of excitons in ZnO-based quantum well heterostructures. *Semiconductor Science and Technology* **20**, S78 (2005).

[69] E. F. Schubert. *Light-Emitting Diodes.* Cambridge University Press, 2nd edition, (2006).

[70] A. Kuzmin and N. Mironova. Composition dependence of the lattice parameter in $Ni_cMg_{1-c}O$ solid solutions. *Journal of Physics: Condensed Matter* **10**, 7937 (1998).

[71] V. Prostakova, J. Chen, E. Jak and S. A. Decterov. Experimental study and thermodynamic optimization of the CaO-NiO, MgO-NiO and NiO-SiO_2 systems. *Calphad* **37**, 1 (2012).

[72] H. V. Wartenberg and E. Prophet. Schmelzdiagramme höchstfeuerfester Oxyde. V. Systeme mit MgO. *Zeitschrift für anorganische und allgemeine Chemie* **208**, 369 (1932).

[73] N. F. Mott. The Basis of the Electron Theory of Metals, with Special Reference to the Transition Metals. *Proceedings of the Physical Society. Section A* **62**, 416 (1949).

[74] S. Huefner. Analysis of the core level satellites in XPS spectra of Ni dihalides. *Solid State Communications* **49**, 1177 (1984).

[75] G. A. Sawatzky and J. W. Allen. Magnitude and Origin of the Band Gap in NiO. *Phys. Rev. Lett.* **53**, 2339 (1984).

[76] J. Zaanen, G. A. Sawatzky and J. W. Allen. Band gaps and electronic structure of transition-metal compounds. *Phys. Rev. Lett.* **55**, 418 (1985).

[77] R. Gillen and J. Robertson. Accurate screened exchange band structures for the transition metal monoxides MnO, FeO, CoO and NiO. *Journal of Physics: Condensed Matter* **25**, 165502 (2013).

[78] C. Rödl, F. Fuchs, J. Furthmüller and F. Bechstedt. Quasiparticle band structures of the antiferromagnetic transition-metal oxides MnO, FeO, CoO, and NiO. *Phys. Rev. B* **79**, 235114 (2009).

[79] U. Schönberger and F. Aryasetiawan. Bulk and surface electronic structures of MgO. *Phys. Rev. B* **52**, 8788 (1995).

[80] F. J. Morin. Electrical Properties of NiO. *Phys. Rev.* **93**, 1199 (1954).

[81] H. Ohta, M. Hirano, K. Nakahara, H. Maruta, T. Tanabe, M. Kamiya, T. Kamiya and H. Hosono. Fabrication and photoresponse of a pn-heterojunction di-

ode composed of transparent oxide semiconductors, p-NiO and n-ZnO. *Applied Physics Letters* **83**, 1029 (2003).

[82] H. Long, G. Fang, H. Huang, X. Mo, W. Xia, B. Dong, X. Meng and X. Zhao. Ultraviolet electroluminescence from ZnO/NiO-based heterojunction light-emitting diodes. *Applied Physics Letters* **95**, 013509 (2009).

[83] H. Sato, T. Minami, S. Takata and T. Yamada. Transparent Conducting p-type NiO thin-films prepared by magnetron sputtering. *Thin Solid Films* **236**, 27 (1993).

[84] Y. Chen and M. Abraham. Trapped-hole centers in alkaline-earth oxides. *Journal of Physics and Chemistry of Solids* **51**, 747 (1990).

[85] T. Kamiya, H. Ohta, M. Kamiya, K. Nomura, K. Ueda, M. Hirano and H. Hosono. Li-Doped NiO Epitaxial Thin Film with Atomically Flat Surface. *Journal of Materials Research* **19**, 913 (2004).

[86] Z. Ji, Z. He, K. Liu, S. Zhao and Z. He. Synthesis of $Mg_xNi_{1-x}O$ thin films with a band-gap in the solar-blind region. *Journal of Crystal Growth* **273**, 446 (2005).

[87] Y. Zhao, J. Zhang, D. Jiang, C. S. Z. Zhang, B. Yao, D. Zhao and D. Shen. MgNiO-based metal-semiconductor-metal ultraviolet photodetector. *Journal of physics D: Applied physics* **42**, 092007 (2009).

[88] J. W. Mares, R. C. Boutwell, M. Wei, A. Scheurer and W. V. Schoenfeld. Deep-ultraviolet photodetectors from epitaxially grown $Ni_xMg_{1-x}O$. *Applied Physics Letters* **97**, 161113 (2010).

[89] Y. Guo, L. Zhu, J. Jiang, Y. Li, L. Hu, H. Xu and Z. Ye. Enhanced performance

of NiMgO-based ultraviolet photodetector by rapid thermal annealing . *Thin Solid Films* **558**, 311 (2014).

[90] H. Nishitani, K. Ohta, S. Kitano, R. Hamano, M. Inada, T. Shimizu, S. Shingubara, H. Kozuka and T. Saitoh. Band gap tuning of $Ni_{1-x}Mg_xO$ films by radio-frequency sputter deposition for deep-ultraviolet photodetectors. *Applied Physics Express* **8**, 105801 (2015).

[91] H. Mizoguchi, H. W. Eng and P. M. Woodward. Probing the Electronic Structures of Ternary Perovskite and Pyrochlore Oxides Containing Sn^{4+} or Sb^{5+}. *Inorganic Chemistry* **43**, 1667 (2004).

[92] X. Luo, Y. S. Oh, A. Sirenko, P. Gao, T. A. Tyson, K. Char and S.-W. Cheong. High carrier mobility in transparent $Ba_{1-x}La_xSnO_3$ crystals with a wide band gap. *Applied Physics Letters* **100**, 052104 (2012).

[93] K. Ganguly, P. Ambwani, P. Xu, J. S. Jeong, K. A. Mkhoyan, C. Leighton and B. Jalan. Structure and transport in high pressure oxygen sputter-deposited $BaSnO_{3-x}$. *APL Mater.* **3**, 062509 (2015).

[94] H. J. Kim, J. Kim, T. H. Kim, W.-J. Lee, B.-G. Jeon, J.-Y. Park, W. S. Choi, D. W. Jeong, S. H. Lee, J. Yu, T. W. Noh and K. H. Kim. Indications of strong neutral impurity scattering in $Ba(Sn,Sb)O_3$ single crystals. *Phys. Rev. B* **88**, 125204 (2013).

[95] H. Mun, U. Kim, H. Min Kim, C. Park, T. Hoon Kim, H. Joon Kim, K. Hoon Kim and K. Char. Large effects of dislocations on high mobility of epitaxial perovskite $Ba_{0.96}La_{0.04}SnO_3$ films. *Applied Physics Letters* **102**, 252105 (2013).

[96] H. J. Kim, U. Kim, T. H. Kim, J. Kim, H. M. Kim, B.-G. Jeon, W.-J. Lee,

H. S. Mun, K. T. Hong, J. Yu, K. Char and K. H. Kim. Physical properties of transparent perovskite oxides (Ba,La)SnO_3 with high electrical mobility at room temperature. *Phys. Rev. B* **86**, 165205 (2012).

[97] R. Eason and D. P. Norton. *Pulsed Laser Deposition of Thin Films.* John Wiley & Sons, Inc., (2007).

[98] P. P. Ewald. *Fifty Years of X-ray Diffraction.* Published for the International Union of Crystallography by A. Oosthoek, Utrecht, (1962).

[99] U. Pietsch, V. Holý and T. Baumbach. *High Resolution X-Ray Scattering: From Thin Films and Multilayers.* New York, Springer, (2004).

[100] E. J. Mittemeijer. *Fundamentals of Materials Science: The Microstructure−Property Relationship Using Metals as Model Systems.* Springer-Verlag Berlin Heidelberg, (2011).

[101] P. J. Eaton and P. West. *Atomic Force Microscopy.* Oxford: Oxford UP, (2010).

[102] D. B. Williams and B. C. Carter. *Transmission Electron Microscopy.* Springer, 2nd edition edition, (2009).

[103] J. Lindemuth and S.-I. Mizuta. Hall measurements on low-mobility materials and high resistivity materials. *Proc. SPIE* **8110**, 81100I (2011).

[104] D. F. Swinehart. The Beer-Lambert Law. *Journal of Chemical Education* **39**, 333 (1962).

[105] O. S. Heavens. Optical properties of thin films. *Reports on Progress in Physics* **23**, 1 (1960).

[106] J. Humlicek. Chapter 1 - Polarized Light and Ellipsometry . In *Handbook of Ellipsometry,* H. G. Tompkins and E. A. Irene, editors, 3. William Andrew Publishing (2005).

[107] H. F. Wong, K. H. Wong and C. H. Lau. Electrical and optical properties of LixNi1-xO/In:MgxZn1-xO heteroepitaxial junction grown on TiN buffered Si. *Physica status solidi (a)* **206**, 2202 (2009).

[108] C.-C. Huang, F.-H. Wang, C.-C. Wu, H.-H. Huang and C.-F. Yang. Developing high-transmittance heterojunction diodes based on NiO/TZO bilayer thin films. *Nanoscale Research Letters* **8**, 206 (2013).

[109] H. Long, L. Ai, S. Li, H. Huang, X. Mo, H. Wang, Z. Chen, Y. Liu and G. Fang. Photosensitive and temperature-dependent I-V characteristics of p-NiO film/n-ZnO nanorod array heterojunction diode. *Materials Science and Engineering: B* **184**, 44 (2014).

[110] J.-Y. Wang, C.-Y. Lee, Y.-T. Chen, C.-T. Chen, Y.-L. Chen, C.-F. Lin and Y.-F. Chen. Double side electroluminescence from p-NiO/n-ZnO nanowire heterojunctions. *Applied Physics Letters* **95**, 131117 (2009).

[111] B. O. Jung, Y. H. Kwon, D. J. Seo, D. S. Lee and H. K. Cho. Ultraviolet light emitting diode based on p-NiO/n-ZnO nanowire heterojunction. *Journal of Crystal Growth* **370**, 314 (2013).

[112] A. G. Thompson and J. C. Woolley. Energy-Gap Variation in Mixed III-V Alloys. *Canadian Journal of Physics* **45**, 255 (1967).

[113] J. A. Van Vechten and T. K. Bergstresser. Electronic Structures of Semiconductor Alloys. *Phys. Rev. B* **1**, 3351–3358 (1970).

[114] J. W. Mares, R. C. Boutwell, A. Scheurer, M. Falanga and W. V. Schoenfeld. Cubic $Zn_xMg_{1-x}O$ and $Ni_xMg_{1-x}O$ thin films grown by molecular beam epitaxy for deep-UV optoelectronic applications. *Proc. SPIE* **7603**, 76031B (2010).

[115] Z.-G. Yang, L.-P. Zhu, Y.-M. Guo, Z.-Z. Ye and B.-H. Zhao. Preparation and band-gap modulation in $Mg_xNi_{1-x}O$ thin films as a function of Mg contents. *Thin Solid Films* **519**, 5174 (2011).

[116] R. Boutwell, M. Wei, A. Scheurer, J. Mares and W. Schoenfeld. Optical and structural properties of NiMgO thin films formed by sol-gel spin coating. *Thin Solid Films* **520**, 4302 (2012).

[117] J. Deng, M. Mortazavi, N. V. Medhekar and J. Zhe Liu. Band engineering of Ni1-xMgxO alloys for photocathodes of high efficiency dye-sensitized solar cells. *Journal of Applied Physics* **112**, 123703 (2012).

[118] Y. H. Kwon, S. H. Chun and H. K. Cho. Controllable band-gap engineering of the ternary $Mg_xNi_{1-x}O$ thin films deposited by radio frequency magnetron sputtering for deep ultra-violet optical devices. *Thin Solid Films* **529**, 417 (2013).

[119] P. F. Fewster and N. L. Andrew. Applications of multiple-crystal diffractometry. *Journal of Physics D: Applied Physics* **28**, A97 (1995).

[120] N. F. Mott and E. A. Davis. *Electronic Processes in Non-Crystalline Materials.* Oxford, Clarendon Press, (1971).

[121] S. Park, H.-S. Ahn, C.-K. Lee, H. Kim, H. Jin, H.-S. Lee, S. Seo, J. Yu and S. Han. Interaction and ordering of vacancy defects in NiO. *Phys. Rev. B* **77**, 134103 (2008).

[122] G. H. Rosenblatt, M. W. Rowe, G. P. Williams, R. T. Williams and Y. Chen. Luminescence of F and F^+ centers in magnesium oxide. *Phys. Rev. B* **39**, 10309 (1989).

[123] Y. M. Guo, L. P. Zhu, J. Jiang, L. Hu, C. L. Ye and Z. Z. Ye. Valence band offset of n-ZnO/p-$Mg_xNi_{1-x}O$ heterojunction measured by X-ray photoelectron spectroscopy. *Applied Physical Letters* **101**, 052109 (2012).

[124] C. A. Niedermeier, M. Rasander, S. Rhode, V. Kachkanov, B. Zou, N. Alford and M. A. Moram. Band gap bowing in $Ni_xMg_{1-x}O$. *Scientific Reports* **6**, 31230 (2016).

[125] S. Holgersson and A. Karlsson. Röntgenographische Untersuchungen einiger Mischkristallsysteme mit Monoxyden als Komponenten. *Zeitschrift für anorganische und allgemeine Chemie* **182**, 255 (1929).

[126] P. K. Davies and A. Navrotsky. Thermodynamics of solid solution formation in NiO - MgO and NiO - ZnO. *Journal of Solid State Chemistry* **38**, 264 (1981).

[127] D.-H. Woo, H.-G. Lee and I.-H. Jung. Thermodynamic modeling of the NiO-SiO2, MgO-NiO, CaO-NiO-SiO2, MgO-NiO-SiO2, CaO-MgO-NiO and CaO-MgO-NiO-SiO2 systems. *Journal of the European Ceramic Society* **31**, 43 (2011).

[128] L. Bellaiche, S.-H. Wei and A. Zunger. Localization and percolation in semiconductor alloys: GaAsN vs GaAsP. *Phys. Rev. B* **54**, 17568 (1996).

[129] P. R. C. Kent and A. Zunger. Evolution of III-V Nitride Alloy Electronic Structure: The Localized to Delocalized Transition. *Phys. Rev. Lett.* **86**, 2613–2616 (2001).

[130] J. Kübler and A. Williams. Itinerant theory of localized magnetism. *Journal of Magnetism and Magnetic Materials* **54**, 603 (1986).

[131] G. Timmer and G. Borstel. Electronic structure of nickel, iron, and cobalt impurities in magnesium oxide. *Phys. Rev. B* **43**, 5098 (1991).

[132] F. Kroeger, H. Vink and J. V. D. Boomgaard. Absorption and fluorescence of solid solutions MgO-NiO. *Physica* **18**, 77 (1952).

[133] R. Pappalardo, D. L. Wood and R. C. Linares. Optical Absorption Spectra of Ni-Doped Oxide Systems. I. *The Journal of Chemical Physics* **35**, 1460 (1961).

[134] W. Duley. Multiphoton excitation of visible and {VUV} luminescence in MgO crystals. *Optics Communications* **51**, 160 (1984).

[135] A. Fazzio, M. J. Caldas and A. Zunger. Many-electron multiplet effects in the spectra of 3d impurities in heteropolar semiconductors. *Phys. Rev. B* **30**, 3430 (1984).

[136] M. Weyers, M. Sato and H. Ando. Red Shift of Photoluminescence and Absorption in Dilute GaAsN Alloy Layers. *Japanese Journal of Applied Physics* **31**, L853 (1992).

[137] M. J. Seong, H. Alawadhi, I. Miotkowski, A. K. Ramdas and S. Miotkowska. Oxygen isoelectronic impurity in ZnS_xTe_{1-x}. *Phys. Rev. B* **60**, R16275 (1999).

[138] W. Shan, W. Walukiewicz, J. W. Ager, E. E. Haller, J. F. Geisz, D. J. Friedman, J. M. Olson and S. R. Kurtz. Band Anticrossing in GaInNAs Alloys. *Phys. Rev. Lett.* **82**, 1221 (1999).

[139] W. Walukiewicz, W. Shan, K. M. Yu, J. W. Ager, E. E. Haller, I. Miotkowski, M. J. Seong, H. Alawadhi and A. K. Ramdas. Interaction of Localized Electronic

States with the Conduction Band: Band Anticrossing in II-VI Semiconductor Ternaries. *Phys. Rev. Lett.* **85**, 1552 (2000).

[140] D. Stauffer and A. Aharony. *Introduction to Percolation Theory.* London: Taylor & Francis, 2nd edition, (1992).

[141] S. Sallis, D. O. Scanlon, S. C. Chae, N. F. Quackenbush, D. A. Fischer, J. C. Woicik, J.-H. Guo, S. W. Cheong and L. F. J. Piper. La-doped $BaSnO_3$ − Degenerate perovskite transparent conducting oxide: Evidence from synchrotron X-ray spectroscopy. *Applied Physics Letters* **103**, 042105 (2013).

[142] U. Kim, C. Park, T. Ha, R. Kim, H. S. Mun, H. M. Kim, H. J. Kim, T. H. Kim, N. Kim, J. Yu, K. H. Kim, J. H. Kim and K. Char. Dopant-site-dependent scattering by dislocations in epitaxial films of perovskite semiconductor $BaSnO_3$. *APL Materials* **2**, 056107 (2014).

[143] C. Park, U. Kim, C. J. Ju, J. S. Park, Y. M. Kim and K. Char. High mobility field effect transistor based on $BaSnO_3$ with Al_2O_3 gate oxide. *Applied Physics Letters* **105**, 203503 (2014).

[144] U. Kim, C. Park, T. Ha, Y. M. Kim, N. Kim, C. Ju, J. Park, J. Yu, J. H. Kim and K. Char. All-perovskite transparent high mobility field effect using epitaxial $BaSnO_3$ and $LaInO_3$. *APL Materials* **3**, 036101 (2015).

[145] Y. M. Kim, C. Park, U. Kim, C. Ju and K. Char. High-mobility $BaSnO_3$ thin-film transistor with HfO_2 gate insulator. *Applied Physics Express* **9**, 011201 (2016).

[146] A. Prakash, J. Dewey, H. Yun, J. S. Jeong, K. A. Mkhoyan and B. Jalan. Hybrid molecular beam epitaxy for the growth of stoichiometric $BaSnO_3$. *Journal of Vacuum Science & Technology A* **33**, 060608 (2015).

[147] K. Nomura, H. Ohta, K. Ueda, M. Orita, M. Hirano and H. Hosono. Novel film growth technique of single crystalline $In_2O_3(ZnO)_m$ (m=integer) homologous compound . *Thin Solid Films* **411**, 147 (2002).

[148] H. Hiramatsu, K. Ueda, H. Ohta, M. Orita, M. Hirano and H. Hosono. Heteroepitaxial growth of a wide-gap p-type semiconductor, LaCuOS. *Applied Physics Letters* **81**, 598 (2002).

[149] H. Hiramatsu, H. Ohta, T. Suzuki, C. Honjo, Y. Ikuhara, K. Ueda, T. Kamiya, M. Hirano and H. Hosono. Mechanism for Heteroepitaxial Growth of Transparent P-Type Semiconductor: LaCuOS by Reactive Solid-Phase Epitaxy. *Crystal Growth and Design* **4**, 301 (2004).

[150] M. Yasukawa, T. Kono, K. Ueda, H. Yanagi and H. Hosono. High-temperature thermoelectric properties of La-doped $BaSnO_3$ ceramics. *Materials Science and Engineering: B* **173**, 29 (2010).

[151] R. J. Cava, P. Gammel, B. Batlogg, J. J. Krajewski, W. F. Peck, L. W. Rupp, R. Felder and R. B. van Dover. Nonsuperconducting $BaSn_{1-x}Sb_xO_3$: The 5s-orbital analog of $BaPb_{1-x}Bi_xO_3$. *Phys. Rev. B* **42**, 4815 (1990).

[152] C. G. Van de Walle. Hydrogen as a Cause of Doping in Zinc Oxide. *Phys. Rev. Lett.* **85**, 1012 (2000).

[153] C. Kilic and A. Zunger. n-type doping of oxides by hydrogen. *Applied Physics Letters* **81**, 73 (2002).

[154] M. Kawasaki, K. Takahashi, T. Maeda, R. Tsuchiya, M. Shinohara, O. Ishiyama, T. Yonezawa, M. Yoshimoto and H. Koinuma. Atomic Control of the $SrTiO_3$ Crystal Surface. *Science* **266**, 1540 (1994).

[155] N. G. Weimann, L. F. Eastman, D. Doppalapudi, H. M. Ng and T. D. Moustakas. Scattering of electrons at threading dislocations in GaN. *Journal of Applied Physics* **83**, 3656 (1998).

[156] M. Oshikiri, Y. Imanaka, F. Aryasetiawan and G. Kido. Comparison of the electron effective mass of the n-type ZnO in the wurtzite structure measured by cyclotron resonance and calculated from first principle theory. *Physica B: Condensed Matter* **298**, 472 (2001).

[157] K. J. Button, C. G. Fonstad and W. Dreybrodt. Determination of the Electron Masses in Stannic Oxide by Submillimeter Cyclotron Resonance. *Phys. Rev. B* **4**, 4539 (1971).

[158] Y. Mi, H. Odaka and S. Iwata. Electronic Structures and Optical Properties of ZnO, SnO_2 and In_2O_3. *Japanese Journal of Applied Physics* **38**, 3453 (1999).

[159] Z. M. Jarzebski. Preparation and physical properties of transparent conducting oxide films. *physica status solidi (a)* **71**, 13 (1982).

[160] D. C. Look, J. W. Hemsky and J. R. Sizelove. Residual native shallow donor in zno. *Phys. Rev. Lett.* **82**, 2552 (1999).

[161] N. Miller, E. E. Haller, G. Koblmüller, C. Gallinat, J. S. Speck, W. J. Schaff, M. E. Hawkridge, K. M. Yu and J. W. Ager. Effect of charged dislocation scattering on electrical and electrothermal transport in n-type InN. *Phys. Rev. B* **84**, 075315 (2011).

[162] G. E. Jellison and F. A. Modine. Parameterization of the optical functions of amorphous materials in the interband region. *Applied Physics Letters* **69**, 371 (1996).

[163] J. Tauc, R. Grigorovici and A. Vancu. Optical Properties and Electronic Structure of Amorphous Germanium. *physica status solidi (b)* **15**, 627 (1966).

[164] F. Wooton. *Optical Properties of Solids.* Academic, New York, (1972).

[165] H. Fujiwara and M. Kondo. Effects of carrier concentration on the dielectric function of ZnO:Ga and In_2O_3 : Sn studied by spectroscopic ellipsometry: Analysis of free-carrier and band-edge absorption. *Phys. Rev. B* **71**, 075109 (2005).

[166] H. Fujiwara. *Spectroscopic Ellipsometry: Principles and Applications*, 200. John Wiley & Sons, Ltd (2007).

[167] S. James Allen, S. Raghavan, T. Schumann, K.-M. Law and S. Stemmer. Conduction band edge effective mass of La-doped $BaSnO_3$. *Applied Physics Letters* **108**, 252107 (2016).

[168] T. Pisarkiewicz, K. Zakrzewska and E. Leja. Scattering of charge carriers in transparent and conducting thin oxide films with a non-parabolic conduction band. *Thin Solid Films* **174**, 217 (1989).

[169] K. F. Berggren and B. E. Sernelius. Band-gap narrowing in heavily doped many-valley semiconductors. *Phys. Rev. B* **24**, 1971 (1981).

[170] C. A. Niedermeier, T. Kamiya and M. A. Moram. Polaron coupling constants in $BaSnO_3$. *arXiv 1602:01343* (2016).

[171] J. Y. W. Seto. The electrical properties of polycrystalline silicon films. *Journal of Applied Physics* **46**, 5247 (1975).

[172] W. Y. Wang, Y. L. Tang, Y. L. Zhu, J. Suriyaprakash, Y. B. Xu, Y. Liu, B. Gao, S.-W. Cheong and X. L. Ma. Atomic mapping of Ruddlesden-Popper faults in transparent conducting $BaSnO_3$-based thin films. *Scientific Reports* **5**, 16097 (2015).

[173] D. Look, C. Stutz, R. Molnar, K. Saarinen and Z. Liliental-Weber. Dislocation-independent mobility in lattice-mismatched epitaxy: application to GaN. *Solid State Communications* **117**, 571 (2001).

[174] K. Krishnaswamy, B. Himmetoglu, Y. Kang, A. Janotti and C. G. V. de Walle. First-principles analysis of electron transport in $BaSnO_3$. *arXiv:1610.06253* (2016).

[175] H. Fröhlich and N. F. Mott. The Mean Free Path of Electrons in Polar Crystals. *Proceedings of the Royal Society of London A: Mathematical, Physical and Engineering Sciences* **171**, 496 (1939).

[176] F. E. Low and D. Pines. The Mobility of Slow Electrons in Polar Crystals. *Phys. Rev.* **91**, 193 (1953).

[177] F. E. Low and D. Pines. Mobility of Slow Electrons in Polar Crystals. *Phys. Rev.* **98**, 414 (1955).

[178] D. M. Eagles. Polar modes of lattice vibration and polaron coupling constants in rutile (TiO_2). *Journal of Physics and Chemistry of Solids* **25**, 1243 (1964).

[179] H. Brooks. Theory of the Electrical Properties of Germanium and Silicon. *Adv. Electron. Electron Phys.* **7**, 85 (1955).

[180] R. Dingle. Scattering of electrons and holes by charged donors and acceptors in semiconductors. *The London, Edinburgh, and Dublin Philosophical Magazine and Journal of Science* **46**, 831 (1955).

[181] W. Zawadzki and T. Moss. *Handbook of Semiconductors.* North-Holland, Amsterdam, (1982). p. 713 (Chapter 12).

[182] H. Yoshikawa and S. Adachi. Optical Constants of ZnO. *Japanese Journal of Applied Physics* **36**, 6237 (1997).

[183] I. Hamberg and C. G. Granqvist. Evaporated Sn-doped In_2O_3 films: Basic optical properties and applications to energy-efficient windows. *Journal of Applied Physics* **60**, R123 (1986).

[184] A. S. Barker and M. Ilegems. Infrared Lattice Vibrations and Free-Electron Dispersion in GaN. *Phys. Rev. B* **7**, 743 (1973).

[185] A. Verma, A. P. Kajdos, T. A. Cain, S. Stemmer and D. Jena. Intrinsic Mobility Limiting Mechanisms in Lanthanum-Doped Strontium Titanate. *Phys. Rev. Lett.* **112**, 216601 (2014).

[186] K. Ghosh and U. Singisetti. Ab initio calculation of electron-phonon coupling in monoclinic β-Ga_2O_3 crystal. *Applied Physics Letters* **109**, 072102 (2016).

[187] K. Hiramatsu. Epitaxial lateral overgrowth techniques used in group III nitride epitaxy. *Journal of Physics: Condensed Matter* **13**, 6961 (2001).

[188] N. A. Richter, F. Stavale, S. V. Levchenko, N. Nilius, H.-J. Freund and M. Scheffler. Defect complexes in Li-doped MgO. *Phys. Rev. B* **91**, 195305 (2015).